ABSTRACT

Design and Implementation of a Custom Imaging Mass Spectrometer

Matthew Ryan Brantley, Ph.D.

Mentor: Touradj Solouki, Ph.D.

Mass spectrometry (MS) has been demonstrated to be a very robust and capable analytical tool for chemical analysis. As such, MS has found application across practically every field of science today. One notable area where MS is utilized is in the analysis of biological samples, such as tissues, where MS has been utilized for lipidomic, proteomic, and metabolomic studies. This document outlines the author's contribution to an ongoing project for developing a novel class of imaging mass spectrometer towards subcellular mass spectrometry imaging.

Construction of the proposed instrument required a great deal of engineering to achieve mass spectral imaging at subcellular spatial resolutions. In many cases, commercially available instrument components did not meet the necessary specifications of the project and thus custom-engineered solutions were necessary. Chapter Two describes many of these custom-engineered subsystems, their functions, and how they contribute toward subcellular mass spectrometry.

In Chapter Three, a technique called Segmented Monte Carlo (SMC) is introduced for unsupervised optimization and characterization of ion optics in mass spectrometers,

including the imaging mass spectrometer outlined in this document. Ion trajectories can be determined either analytically or numerically. Although analytical solutions can account for ion trajectories under ideal conditions, they are mathematically complex and limited to describing relatively simple and static systems. Numerical solutions are mathematical approximations that, when given sufficient computational resources, are capable of approaching analytical solutions in accuracy. Using SMC, it is demonstration that numerical solutions are more appropriate for complex, arbitrary, or dynamic systems and can be determined stochastically in an automated, rapid manner.

In Chapter Four, the instrument control platform Data Station One (DSO) is introduced. DSO is utilized to control the numerous automation tasks required of this instrument, in addition to data analysis. The highly modular architecture of DSO enabled it's use in the rapid prototyping of the multiple subsystems that make up the imaging mass spectrometer. Chapter Five completes this dissertation by discussing future research and outlines a plan for completion of the imaging mass spectrometry instrument.

Design and Implementation of a Custom Imaging Mass Spectrometer

by

Matthew Ryan Brantley, B.S.

A Dissertation

Approved by the Department of Chemistry and Biochemistry

_____

Patrick J. Farmer, Ph.D., Chairperson

Submitted to the Graduate Faculty of
Baylor University in Partial Fulfillment of the
Requirements for the Degree
of

Doctor of Philosophy

Approved by the Dissertation Committee

_____

Touradj Solouki, Ph.D., Chairperson

_____

C. Kevin Chambliss, Ph.D.

_____

Elyssia S. Gallagher, Ph.D.

_____

Kevin L. Shuford, Ph.D.

_____

Scott Koziol, Ph.D.

Accepted by the Graduate School

August 2019

_____

J. Larry Lyon, Ph.D., Dean

Page bearing signatures is kept on file in the Graduate School.

TABLE OF CONTENTS

LIST OF FIGURES

LIST OF SCHEMES

LIST OF TABLES

LIST OF ABBREVIATIONS

Abbreviation	*Description*
AC	Alternating Current
APCI	Atmospheric Pressure Chemical Ionization
API	Atmospheric Pressure Ionization
APPI	Atmospheric Pressure Photoionization
CDEM	Continuous Dynode Electron Multiplier
CI	Chemical Ionization
CMS	Content Management System
CSV	Comma Separated Value
DAQ	Data Acquisition
DC	Direct Current
DDA	Data Dependent Analysis
DESI	Desorption Electrospray Ionization
DNA	Deoxyribonucleic acid
DSO	DataStation One
EI	Electron Ionization
EM	Electron Multiplier
EM	Electron Multiplier
ESI	Electrospray Ionization
FAB	Fast Atom Bombardment
FDI	Field Desorption/Ionization
FI	Field Ionization
FIB	Focused Ion Beam
FIB-SEM	Focused Ion Beam-Scanning Electron Microscopy
FPGA	Field Programmable Gate Arrays
FT-ICR	Fourier Transform-Ion Cyclotron Resonance
FT-MS	Fourier Transform-Mass Spectrometry
GA	Genetic Algorithm
GCIB	Gas Cluster Ion Beam
GUI	Graphical User Interface
IM	Ion Mobility
IRMPD	Infrared Multiphoton Dissociation
LC	Liquid Chromatography
LMIS	Liquid-Metal Ion Source
m/z	Mass-to-Charge Ratio
MALDI	Matrix-Assisted Laser Desorption/Ionization
MCP	Microchannel Plate
MS	Mass Spectrometry
MSI	Mass Spectrometry Imaging

Abbreviation	*Description*
NMR	Nuclear Magnetic Resonance
PC	Personal Computer
PEEK	Polyether Ether Ketone
pps	Pixels Per Second
PSG	Pulse Sequence Generator
REMPI	Resonance Enhanced Multi-Photon Ionization
RF	Radio Frequency
RNA	Ribonucleic acid
ROI	Region of Interest
S/N	Signal-to-Noise Ratio
SDK	Software Development Kit
SEM	Scanning Electron Microscopy
SIMS	Secondary Ion Mass Spectrometry
SMC	Segmented Monte Carlo
TEM	Tunneling Electron Microscopy
TOF	Time-of-Flight
UHC	Ultra-High Vacuum
USB	Universal Serial Bus

ACKNOWLEDGMENTS

My personal gratitude is extended to my PhD advisor, Dr. Touradj Solouki, for his leadership, guidance, and patience during my graduate studies at Baylor University. The degree of instrumentation, methods, and analytical prowess made available to me during my graduate studies has significantly contributed on my abilities as an analytical scientist. As a 1st-year graduate student, all of these resources were made available to me not because I had the necessary experience, but because of an interest in my development as a scientist by Dr. Solouki and the greater Baylor Community. Furthermore, it was through this support that I was able to share my research in high-impact, peer-reviewed journals, present my research at international conferences, and interact with leading scientists in multiple fields.

I would additionally like to extend my gratitude to the other members of my committee, Dr. C. Kevin Chambliss, Dr. Elyssia Gallagher, Dr. Kevin Shuford, and Dr. Scott Koziol. Throughout my studies, the feedback from the members of my committee were invaluable to my studies and development as a scientist. I would also like to extend a personal thanks to Dr. Chambliss and Dr. Gallagher for their personal guidance.

A great deal of my success throughout graduate school is owed to my peers, past and present. I want to thank my fellow group members, Dr. Behrooz Zekavat, Dr. Mahsan Miladi, Dr. Abayomi Olaitan, Dr. Brett Harper, Dr. Michael Pettit, Jackie Lockridge, Ian Anthony, Luke Richardson, Raul Villacob, Amy Schnelle, Kyle Wilhelm, Drew Stolpman. I also want to thank the undergraduate members of the Solouki group, especially Elizabeth Neumann, Brooke Brown, Carter Lantz, Adam Floyd, Shihou Zhou, and Christina Gaw.

The input, advice, and efforts of our collaborators were invaluable to my time in graduate school. I want to personally thank our collaborators, Dr. Pat Farmer and Dr. Bill Hockaday of Baylor University, Dr. Kermit Murray and Dr. Fabrizio Donnarumma of Louisiana State University, Dr. Deniz Erdogan and Dr. Emrah Ozensoy of Bilkent University.

Finally, I want to express my thanks to my friends and family. To my wife, Ashley, thank you for your unwavering support throughout my graduate career. To my mother, Deborah, thank you for believing in me and giving me the strength to overcome the inevitable hurdles of graduate school. To my father, Don, thank you for stoking the curiosity within me that has led me down the path of insight.

DEDICATION

To my wife, Ashley, for giving me support.

To my mother, Deborah, for giving me strength.

To my father, Don, for giving me inspiration.

CHAPTER ONE

Introduction

1.1 Introduction to Mass Spectrometry

Mass spectrometry (MS) is an analytical technique in which mass-to-charge ratios (*m/z*) of ionized molecules and atoms are measured and used for chemical analyses.[1] Operated exclusively in the gas-phase, measurements of an ion's *m/z* is made possible by exposing the ion to magnetic and electric fields and observing its behavior.[2] The high reproducibility, sensitivity, and dynamic range of MS has facilitated its use in quantitative measurements in fields such as environmental monitoring,[3-8] food & safety,[8-12] and biomedical analysis.[13-19] Furthermore, MS is a highly useful technique for exploratory studies as it has been readily applied to biopolymer sequencing (including polypeptides,[20-21] sugars,[22-23] and polynucleotides[24-25]), surface[26-28] and tissue analyses,[29-30] and even macromolecular structure analyses.[31-32] From small, persistent gases to very large protein macromolecules, MS techniques have found their place at the forefront of numerous fields of science.

1.2 Mass Spectrometry Instrumentation

Mass spectrometry instruments can vary dramatically in their implementations; however, at the highest level, all MS instruments consist of a minimum of four key components,[1] the ion source, a mass analyzer, a detector, and a vacuum chamber/electronics. In some cases, multiple sources, analyzers, or detectors can exist in a single instrument, as is the case with the triple-quadrupole MS.[33] Furthermore, the image

current detectors used in Fourier transform mass spectrometers are often physically the same component as their associated mass analyzer.[34-35]

1.2.1 Ionization Sources

The ionization source(s) of a mass spectrometer serves to ensure molecules in the mass spectrometer have the net charge(s) necessary for analysis. Typically, positive ions are generated from a molecule through radical cation formation[36] (to form $[M^{\bullet+}]$ ions), protonation[37-38] (to form $[M+H]^+$ ions), or through non-covalent adduction of (usually) Group 1 and Group 2 metals[39] (although ionization *via* small molecule charge carriers such as NH_3 are also common). Negative ion generation is typically possible through deprotonation[40-41] (to form $[M-H]^-$ ions) or non-covalent adduction of usually Group 16 and Group 17 elements[39] (although, small molecule charge such as H_2O carriers are common as well). Before ionization, neutral analytes can vary dramatically in their composition as well as in their physical phase. As such, ionization techniques in mass spectrometry are typically categorized by the phase of material they are suitable with as well as the relative "hardness" of the technique[42]. The term "hard" is used to denote that the ionization technique results in the generation of primarily fragment ions. The term "soft" denotes an ionization event wherein primarily non-fragmented (*i.e.*, intact) ions are generated.

1.2.1.1 Gas-phase ionization. Gas-phase ionization was the first ionization technique utilized in mass spectrometry because it did not require any phase transition of the sample to become compatible with the mass spectrometer. J. J. Thomson, famous for his discovery of the electron,[43] utilized ions generated in a cathode-ray tube and MS

analysis in his discovery of isotopes.[44-45] Today, a variety of gas-phase ionization techniques are used depending on the type of sample being ionized.

Electron ionization (EI)[36] is the most common gas-phase ionization technique. In an EI source, gaseous material is intersected by a beam of electrons to generate ions. In this process, an electron passing close to a molecule distorts the electron cloud surrounding the molecule. If the electron has sufficient kinetic energy, this can result in the ejection of a valence electron and formation of a radical cation ($M^{\bullet+}$).[36] EI is generally considered a hard ionization technique, primarily due to the extensive fragmentation that occurs in standard 70eV EI sources. However, lower energy EI experiments can result in less fragmentation at the cost of lower efficiency.[36] Electron generation for EI typically comes from a thermionic emitter.[46] However field-effect emitters[47] are also used for EI.[48] Furthermore, experiments into radio-frequency ionization (RFI)[49-50] revealed RFI to also be an electron ionization technique[51] resulting from a potentially novel class of electron emitter.

Chemical ionization (CI) is another common gas-phase ionization technique in which a charged molecule, called the reagent gas (likely generated separately using EI), comes in contact with a molecule and either donates or receives a proton to form $[M+H]^+$ or $[M-H]^-$ ions, respectively.[52] CI is considered to be a soft ionization technique.[53-54]

Photoionization is another class of gas-phase ionization in which molecules absorb a photon, resulting in promotion of an electron past the ionization threshold.[55-56] Single-photon ionization[57] requires lasers typically in the UV or X-ray regime and can result in molecule ionization. Multi-photon ionization,[58] on the other hand, results from absorption of several photons. For multi-photon ionization techniques like resonance enhanced multi-

photon ionization (REMPI), information about a molecules electronic states can also be probed.[59]

A fourth type of gas-phase ionization is field ionization (FI).[60-61] In FI, a molecule is exposed to very strong electric fields (10^7-10^8 V/cm)[61] under which an electron can be extracted through quantum tunneling to form primarily $M^{\bullet+}$ ions. Because minimal energy is introduced into the molecule during this event (aside from the energy necessary to tunnel the electron), FI is a notably soft ionization technique with almost exclusively molecular ions observed.[60]

1.2.1.2 Solution-phase ionization. Solution-phase ionization has ubiquitous use in biological mass spectrometry.[62-63] For example, proteomics analysis usually involves the analysis of proteins suspended in an aqueous solvent.[64] Liquid chromatography (LC)[65] is a useful tool for separating biological molecules that, for simplicity of engineering, necessitates the use of solution-phase ionization.[66]

Electrospray ionization (ESI)[37, 67] is a highly sensitive ionization technique that works by forcing a liquid solution through a small needle that is biased to a few kilovolts relative to the MS inlet. When exposed to the strong electric field gradient (usually expressed in units of v/cm) ions are generated through at least one of three proposed ionization mechanisms, the ion evaporation model (IEM),[68] the charge residue model (CRM),[69] or the chain-ejection model (CEM).[70] ESI is a soft ionization technique which produces primarily $[M+H]^+$ ions as well as a variety of adducted species.[37] ESI works best for ions with reasonable polarizability.[71]

Atmospheric pressure chemical ionization (APCI) is a solution-phase approach to chemical ionization in which a corona discharge pen is installed near a nebulized plume of

solution.[52, 72] Ionized gas from the corona pen can then undergo proton transfer reaction in a similar manner to gas-phase CI.[52] Because of the geometric similarities to ESI, combination APCI/ESI sources are fairly common.[72]

Photoionization of solution is also possible through atmospheric pressure photoionization (APPI).[56] Typically, using an argon lamp, a nebulized solution is bombarded by blackbody radiation resulting in the formation of ions.[55] APPI is commonly used for ionization of molecules with small or negligible polarizabilities that are unsuitable for ESI.

1.2.1.3 Solid-phase ionization. Solid-phase ionization techniques vary in applications, with modern day usage primarily focused towards use in imaging applications[73-75] and surface analysis.[28, 76] Further discussion into the application and instrumental requirements of solid-phase ionization can be found in Section 1.4.

Matrix-assisted laser desorption/ionization (MALDI)[77] is nowadays the most common form of solid-phase ionization, especially for tissue analysis. By coating or mixing a solid-phase material with a matrix[78] specifically tuned to absorb energy of a certain wavelength of light (typically 337.1 nm) followed by exposure to laser radiation, MALDI can be used to very softly generate molecular ions from a variety of biological samples.[38] Further, MALDI can be utilized for extracting spatial information by rastering the laser across a sample to form a mass spectral image.[79]

Fast atom bombardment (FAB) is another technique for generating ions from solid-phase material.[80] FAB ionization works by focusing a high energy beam of atoms towards a material.[81] Collision of the high energy atoms with the material substrate is a high energy process resulting in generation of ionized substrate molecules. A mixture of the material

substrate with a non-volatile matrix, such as glycerol, can act to disperse the energy of collision and thus allow FAB to be used as a soft ionization technique.[82]

Secondary ion mass spectrometry (SIMS) resembles FAB but, instead of a high energy atom beam, SIMS utilizes a high energy ion beam.[26] Various ion beams have been utilized for SIMS. Beams produced from ions such as Ga^+ have narrow beam widths but are hard ionization techniques.[83] In contrast, beams produced from C^{60} are more diffuse but are able to produce molecular ions of smaller biomolecules.[84]

1.2.2 Mass Analyzers

Independent of how ions are generated, the mass analyzer(s) serve to separate these ions by the ions' *m/z* values using various electric and/or magnetic fields. Tandem MS experiments utilize multiple stages of mass analysis[85] and (as Tandem MS is often highly desirable for structural analysis because of the ability to study molecule fragmentation) many modern instruments utilize multiple mass analyzers.

1.2.2.1 Spatially dispersive mass analyzers. Spatially dispersive mass analyzers utilize electric and/or magnetic fields to vary ion trajectories as a function of *m/z*. When ions are spatially dispersed, only a given range of *m/z* values can reach the detector (or subsequent mass analyzers) at any given point. The smaller range of *m/z* values can limit spatially dispersive mass analyzers' sensitivity when operating over large *m/z* ranges. However, spatially dispersive mass analyzers operate in a "continuous" fashion, meaning a constant stream of ions can be analyzed without interruption.

Sector mass analyzers were one of the earliest forms of spatially dispersive mass analyzers.[86] In a sector mass analyzer, an ion enters into a geometry that is bent off-axis at a certain angle and radius. Ions are exposed to an electric or magnetic field (or both[87-88])

that changes the ions' direction based on the ions' *m/z* and kinetic energy. If the change in direction of an ion matches the angle and radius of the sector geometry, the ion will successfully exit the mass analyzer. Alternatively, if the change in an ion's direction is too fast or slow for a given geometry then the ion will collide with the walls of the mass analyzer and neutralize.

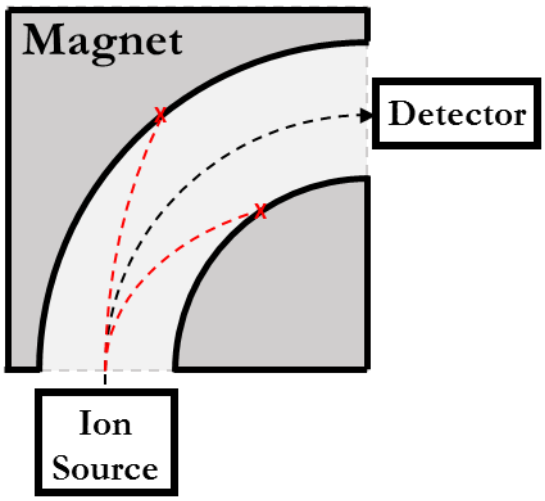

Scheme 1.1. Representation of a magnetic sector mass analyzer. Ion trajectories that pass through the analyzer are shown in black while ion trajectories that are not transmitted are shown in red.

For magnetic sectors, transmission occurs when the centripetal force (F_C) of the ion is equal to the deflection force imposed by the magnetic field (F_B).

Equation 1.1: $$F_C = F_B$$

Plugging in equations for centripetal force (F_C), and magnetic force (F_B) we get the following:

Equation 1.2: $$\frac{mv^2}{r} = ezvB$$

Where *m* is the ion mass, *v* is its velocity (in meters/second), *r* is the radius of the centripetal path (in meters), *e* is the charge of a proton (in coulombs), *z* is the point

charge of the ion (unitless), and *B* is the magnetic field strength (in tesla). Substituting in the kinetic energy equation:

Equation 1.3: $$KE = \frac{mv^2}{2} = ezV$$

We can find the solution of *B* and *V* (accelerating voltage) for a given *m/z*.

Equation 1.4: $$\frac{m}{z} = \frac{B^2 r^2 e}{2V}$$

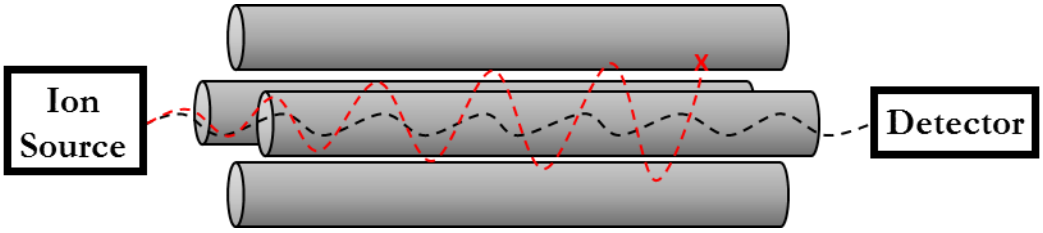

Scheme 1.2. Schematic representation of a quadrupole mass analyzer. Ions transmitted through the analyzer are shown in black while ions not transmitted are shown in red.

The Quadrupole mass analyzer is another spatially dispersive mass analyzer in which a bipolar RF potential is applied to opposing rods and a "resolving" DC potential can be used to select for individual mass ranges.[89] Furthermore, quadrupoles can be operated in "RF-Only" mode by removing the "resolving" DC potential, allowing a large *m/z* range of ions to pass. As such, quadrupoles are regularly used as both mass analyzers and as ion transport optics. Ion trajectories within the quadrupole can be described by the Mathieu equations and are discussed in more detail in Chapter 3.

1.2.2.2 Temporally dispersive mass analyzers. Temporally dispersive mass analyzers separate ions in a given path temporally by their *m/z*. These mass analyzers, referred to as time-of-flight (TOF) mass analyzers, are pulsed operation and require an ion accumulation step prior to each operation cycle.[90] In TOF mass analysis, ions of various *m/z* values are given potential energy through a repelling voltage according to:

Equation 1.5: $E_p = ezU$

Where E_p is the potential energy (in joule), e is the charge of a proton (in coulombs), z is the point charge of the ion (unitless), and U is the electric potential (in volts). The potential energy (E_P) is converted to kinetic energy (E_K) which is calculated according to:

Equation 1.6: $E_k = \frac{1}{2}mv^2$

Where E_k is the kinetic energy (in joules), m is the mass of the ion (in kilograms), and v is the ion's velocity (in m/s). Setting E_K an E_P to be equal gives us:

Equation 1.7: $ezU = \frac{1}{2}mv^2$

While measuring velocity natively can be difficult, given a known electric field gradient (U) and a known flight distance (d), it can be calculated from the ions time-of-flight (t) using the following equation:

Equation 1.8: $v = \frac{d}{t}$

Whereas various spatially dispersive mass analyzers can only observe a single *m/z* range at any given point and ions outside of that range are lost, TOF mass analyzers can measure multiple ions of different *m/z* at the same time and are thus more sensitive for use when measuring many different *m/z* values.

1.2.2.3 Ion trap mass analyzers. Ion trap mass analyzers are a unique class of mass analyzers that can accumulate and store ions and, in some cases, provide unique experimental capabilities. Ion trap mass analyzers come in many varieties, although two primary types are those that use electrostatic fields to trap ions (Paul[91] and

Kingdon/Oribtrap[92] traps) and those that use both electric and magnetic fields to trap ions (Penning traps[93]).

One limitations of ion trap mass analyzers is that the ion traps can only contain a finite number of ions at a given time, leading to limited quantitation capabilities when compared to TOF and quadrupole mass analyzers (although ion traps are used for quantitative analyses[18]). For certain types of ion traps, a "microscan" can be taken to determine the relative ion flux as a function of time. Using the ion flux measurement, ions are then accumulated in the trap for a precise amount of time with the goal of achieving a specific charge density.[94] Additionally, most ion trap MS instruments have moderate-to-slow duty cycles (on the order of 10 to 2,000+ ms). Alternatively, advantages of ion trap mass analyzers are that the trapped ions can be subjected to novel, tandem-MS strategies (such as infrared multiphoton dissociation (IRMPD)[95]) and that Fourier transform-mass spectrometry (FT-MS) data (such as that produced from Orbitraps and FT-ICRs) is usually significantly higher *m/z* resolution (100,000 – 1,000,000 m/Δm at half-height) than data produced by either spatially or temporally-dispersive MS.

In FT-ICR MS, ions are trapped in a Penning trap (trapped radially by the magnetic field and trapped axially by electric fields). FT-ICR takes advantage of not only the trapping capabilities of the magnetic field but also the unique motion of ions within a magnetic field. When in a magnetic field, ions move in a circular motion called a cyclotron at a frequency proportional to the *m/z* of the ion and the magnetic field strength.

Equation 1.9: $$f = \frac{qB}{2\pi m}$$

where f is the cyclotron frequency (in hertz), q is the ion charge (in coulombs), B is the magnetic field strength (in tesla), and m is the ion mass (in kg).

By careful application of energy (during a step known as "excitation"), ions may both be excited to higher radii as well as induced into more coherent "packets" where all ions of a given *m/z* have not only the same frequency (which is a constant in the Penning trap) but also the same (or nearly the same) phase. After the "excitation" step, and as the ion packets oscillate radially within the Penning trap, the ion packets may be detected by the current they induce when passing by a set of detection plates. This method of detection is described in more detail below in Section 1.2.3.1.

1.2.3 Mass Spectrometry Detectors

The last component of the mass spectrometer is the detector(s), which in conjunction with the mass analyzer(s), provides the relevant information to calculate the *m/z* of the various ions. Although various implementations of detector devices exist, all detectors serve the purpose of providing an electrical signal (although some of the earliest versions did use scintillators[96]) in response to the presence of ions.[2] Quantitative detection is possible with mass spectrometry detectors; however, due to the large number of instrumental variables, a calibration curve using known quantity standards is necessary.[16, 18]

1.2.3.1 Charge detectors. Charge detectors come in various forms for the measurement of incident charges when a charged particle collides with the detector. The simplest form of a charge detector is a Faraday cup in which a small electrical current is produced each time a charge particle collides with its metal surface.[97] Electron multipliers (EM)s provide a large signal-gain through multiple stages of secondary emission before collision with a Faraday cup and are available in discrete[98] and continuous dynode

configuration.[99] A grid of continuous dynode EMs can be organized on a plate into what is known as a microchannel plate (MCP) detector.[100]

1.2.3.2 Image current detectors. In contrast to charge detectors, image current detectors[101] do not require collision of an ion to a conductive surface but instead measure the current induced by the movement of a charged particle towards or away from a metallic plate and are considered a "non-destructive" form of detection. Image current detectors in mass spectrometry are typically found in FT-MS[34] instruments (i.e., Orbitrap/Kingdon trap and Penning trap ion trap mass analyzers) which utilize the combined image currents of all ions within the ion trap to measure the oscillating packets of ions before frequency analysis using a Fourier transform.[102]

The Fourier transform is a method of extracting pure frequency information from overlapping sinusoidal signals in a "complex waveform" comprised of many different frequencies. Such a waveform is precisely the signal produced on the detection plates of an image current detector such as an Oribtrap or FT-ICR cell. Ions (or ion packets if sufficient coherency has been induced) are concurrently observed as multiple, overlapping sinusoidal waveforms. After observing the motions of these ions and collection of their time-domain signals for some time (often 10 to 2,000 ms), a Fourier transform may be performed to convert the complex waveform information into a set of ion frequencies.[102] The resolution of the frequency-domain spectra is dependent on how many oscillations were observed, how stable the oscillation frequency is, and the lifetime of the signal. Two methods of increasing the number of observable oscillations are increasing the oscillation frequency and observing the oscillations for a longer period of time.

Increasing the frequency of oscillations in FT-MS generally requires different physical hardware (such as a higher strength magnet for FT-ICR or higher trapping potentials in an Orbitrap). The length of observation is primarily limited to the de-phasing of the ion packets (i.e. coherence is lost). De-phasing occurs due to a number of factors including, but not limited to, collisions of the ion packet with neutral atoms/molecules that were not evacuated from the vacuum chamber (pressure-limited), dispersion caused by random motion (i.e., increasing entropy), dispersion caused by coulombic charge repulsion (as ions within the same packet are similarly charged and will repel one another).

The signal produced from a single observation of a given ion is significantly lower for image current detectors in comparison to charge detectors; however, it is not uncommon for image current detectors to observe a given ion up to a million times in a single detection event.[34] Furthermore, image current detectors typically utilize differential signal detection to dramatically reduce external noise interference.[103-104]

1.3 Mass Spectrometer Engineering

Given the previous introductions to the components of mass spectrometers and their numerous combinations, it might come without surprise that mass spectrometers are not generally not simple to engineer. Mass spectrometers can require the use of high and ultra-high vacuum (10^{-6}–10^{-12} torr), voltages in the kilovolts range, sub-microsecond timings, use of cryogenic cooling and/or heating past the boiling point of water, millions of data points per acquisition, and advanced data analysis requirements.[2] As such, proper MS engineering is a multi-disciplinary problem that requires special understanding of its unique requirements.

1.3.1 Vacuum Pumps and Measurement

Mass spectrometry requires the use of vacuum systems for operation of many of its components; however, the vacuum requirements can vary significantly between instruments. Quadrupole[89] and TOF[90] mass analyzers are typically operated in the range of $1x10^{-6}$ torr, while FT-MS[34] mass analyzers require vacuum as high as $1x10^{-10}$ torr. For discussion purposes, we refer to the $1x10^{-3}$ to $1x10^{-9}$ torr regime as "high vacuum" and the $1x10^{-9}$ to $1x10^{-12}$ torr regime as "ultra-high vacuum".[105] Each regime comes with unique benefits and drawbacks. MS instruments capable of operating at pressures as high as 1 torr have been tested in laboratory settings but are outside of this discussion.[106]

The high vacuum regime is commonly used in quadrupole and TOF mass analyzers and requires the use of a dual-stage pumping system. Commonly, mechanical pumps are used to generate pressures of around $5x10^{-2}$ torr in series with a turbomolecular or diffusion pump. These turbomolecular or diffusion pumps are what achieve the high vacuum inside the chamber. At high vacuum, Viton® (a high-performance fluoropolymer) gaskets are sufficient seals to maintain vacuum,[107] although soft-metal gaskets are sometimes utilized at the upper end of this vacuum range.[108] Electric insulators constructed from PEEK (polyether ether ketone) are common for use in high vacuum applications and have very low outgassing.[109]

The ultra-high vacuum regime is harder to engineer,[110] but is a requirement of most FTMS mass analyzers as the mean free path is in excess of a few km. Utilizing a similar pumping strategy to high vacuum, special care is given to the ultimate pressure of the pumps utilized. Furthermore, Viton® gaskets are no longer suitable for maintaining this level of vacuum (only soft-metal gaskets can be used) and PEEK insulators should be

replaced with ceramic insulators. When pumping down, it is not uncommon to heat the vacuum chamber in excess of 150° C for days to remove contaminants before reaching ultra-high vacuum.[110]

In instruments where an atmospheric interface is required (such as when coupled with many liquid- and solid-phase ionization sources) a differential pumping strategy is required wherein sequential vacuum chambers are connected through low-conductance orifices (limiting gas flow but still allowing guided ions to travel through) with each stage having higher vacuum than the previous. The use of continuous accumulation quadrupoles as well as the advent of ion mobility (IM) separations within the mass spectrometer (both of which require maintaining a higher pressure of gas) have required some instruments to have as many as 5 different vacuum chambers within a single instrument to main proper vacuum pressures.[111]

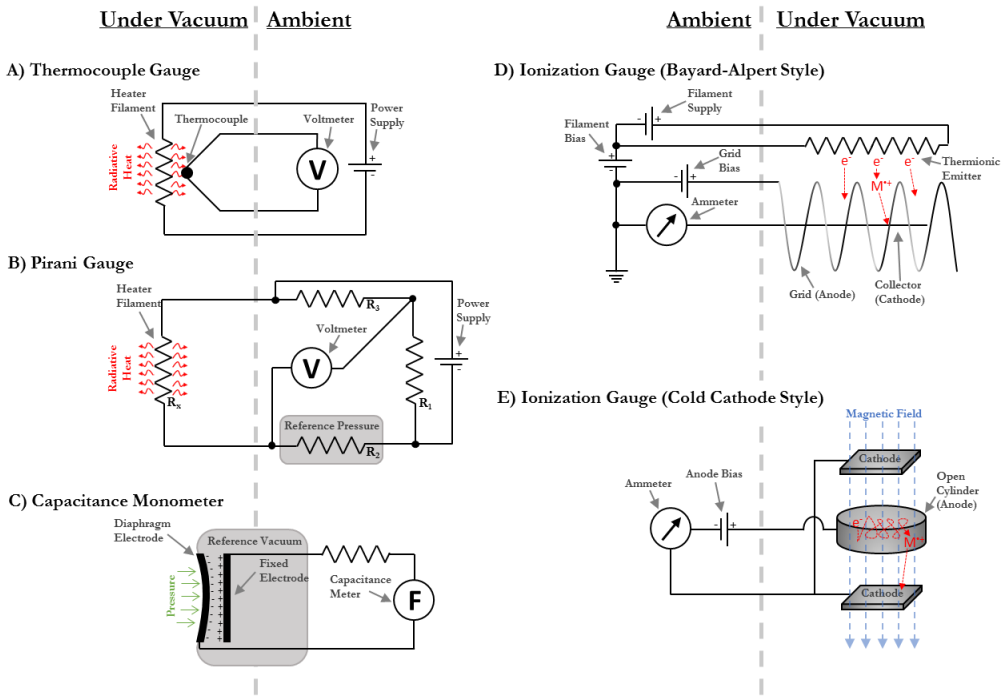

Scheme 1.3. Schematic representation of common vacuum measurement devices. Only components necessary for the measurement operation are shown.

Pressure measurement is required when ensuring proper vacuum is achieved at each stage of the mass spectrometer. While many other types of vacuum measurement devices exist, the five most commonly used for vacuum measurement in modern systems are shown in Scheme 1.3. The first two vacuum measurement devices (Scheme 1.3A-B) operate by measuring thermal transfer properties of an unknown system. Thermal transfer is highly dependent on gas type and gas pressure[112], thus it is common to see these types of devices calibrated for specific gases. Assuming the gas composition is relatively well understood, and mass transfer is minimized, thermal transfer is then primarily dependent on gas pressure and thus is a suitable property for pressure measurement. Thermal transfer gauges are suitable for pressures between 1,000 and $1x10^{-4}$ torr and come in two primary configurations, the thermocouple gauge (Scheme 1.3A), where the heat from a strand of heated filament is measured using a thermocouple, and the Pirani gauges (Scheme 1.3B), where a filament is configured as a leg in a Wheatstone bridge[113] for measuring its temperature-dependent resistance. In a Pirani gauge, the steady-state temperature of the filament is a function of the total heat dissipated and the thermal transfer of the surrounding gas. By applying a constant current to the filament (for constant heat dissipation), the steady-state temperature is then dependent primarily on the thermal transfer properties of the surrounding gas.

Capacitance gauges (Scheme 1.3C) can measure between 1,125 and $3.8x10^{-5}$ torr and operate by measuring the capacitance between two plates, one off which acts as a barrier between a reference pressure and the test pressure. As external pressure increases, the plates are mechanically closer resulting in an increased capacitance. An increase in capacitance is the direct result of gas pressure and thus capacitance gauges are notably

insensitive to gas composition.[114] Capacitance monometers are typically more accurate than thermal transfer gauges; however, capacitance measurements are not as simple as resistance measurements and require long thermal equilibration times usually exceeding 1 hour.

Ion gauges operate by measuring the ion current generated under a constant electron emission (*via* electron ionization[36]). As gas pressure decreases, the probability of collision between an emitted electron and a gas molecule decrease thus resulting in fewer charged molecules reaching the collector. The most common type of ion gauge found in scientific instrumentation is the Bayard-Alpert style (Scheme 1.3D) in which a filament is heated sufficiently for thermionic emission of electrons[46] and the collector is surrounded by a grid to extract electrons. An alternative to the heated filament in the Bayard-Alpert configuration is the Cold-Cathode style (Scheme 1.3E; also referred to as a Penning gauge). In the Cold-Cathode arrangement, a strong magnet and trapping electrodes are used to capture electrons generated from a self-sustaining discharge. Similar to the Bayard-Alpert configuration, when an electron is incident to a neutral molecule it can undergo electron ionization[36] and the resulting charged particle move towards the collector; however, in the Cold-Cathode arrangement the emitted electrons are captured in the trap (thus increasing the electron density in the trap). Cold-Cathode ion gauges require an initial population of trapped electrons and thus rely on an initial electron emission event (field emission or otherwise) before they can function.

1.3.2 Electronics, Timing, and Amplification

Mass spectrometry makes extensive use of electronics to generate the numerous signals required for the various electric/magnetic fields being applied and signals being

detected. For example, a relatively common ESI-TOF-MS instrument requires a few kilovolts of potential on the ESI source, tens of kilovolts on the pusher, and bias potentials on the detectors well into the kilovolts range (in addition to dozens of other signals being applied). The high operating speed of the TOF necessitates jitter be on the sub-ns scale in addition to digitizers able to measure at 4 GHz or higher. Combined with the growing demand for real-time, data-dependent experiment modifications, the electronic engineering requirements of MS can be exceedingly difficult.

Central to all instrumentation requiring sub-millisecond precision is a pulse sequence generator (PSG)[115] which, for all intents and purposes, ensures all electronic components are able to perform their respective functions at the correct time by providing deterministic trigger pulses. Various implementations of PSGs are available and range from small universal serial bus (USB) devices to dedicated cards in a computer and even custom field programmable gate arrays (FPGA). When synchronization requirements of a project require jitter on timescales shorter than nanoseconds, synchronization clocks (a central system clock shared by all components in lieu of individual internal clocks) may be required. As a rule, the timing requirements of a project should be defined before any electronics design should begin.

The various ion optics (i.e., the required electric/magnetic fields) require some form of amplification and filtering since most signal generators do not meet the required voltage or current draw of the ion optics. Discussion of signal generation, amplification, and filtering for use in mass spectrometry requires entire textbooks[116-119] and thus is beyond the scale of this discussion. However, there are a few notable electronics companies that provide electronics directly for use in mass spectrometry, such as Ardara Technologies,[120]

GAA Custom Engineering,[121] Stahl-Electronics,[122] Extrel CMS,[123] Fasmatech,[124] which can serve as excellent starting points when addressing an MS electronics system.

1.3.3 Instrument Control Software

Instrument control software serves an important role in enabling researchers to interact with the instrument they are using. Tasks seemingly as simple as modifying an experimental procedure can be very time consuming unless previous efforts were made to facilitate this in the control software. The lack of suitable tools for implementing instrument control software necessitated an entire manuscript (Chapter 4 – "Data Station One: An Open Source, Modular Control Platform for Custom Imaging Mass Spectrometers") to remedy this problem.

1.3.4 Data Analysis Software

Modern mass spectrometers are capable of collecting an astounding amount of data, especially in the case of TOFs coupled with multiple chemical separations like the AccuTOF-GCx,[125] Pegasus GC-HRT 4D,[125] and Synapt[111] instruments. Visualizing the data generated by such devices requires special software. Imaging mass spectrometers have similar difficulties, where each pixel in an image corresponds to an entire mass spectrum.[79] Furthermore, efforts towards coupling ion mobility (IM) with imaging mass spectrometry add another degree of difficulty in data complexity.[126-127]

Before attempting to develop an instrument, it is important to understand how to collect, store, and retrieve information collected from the proposed instrument. In some cases, predefined data file formats such as Technical Data Management Streaming (TDMS),[128] Comma Separated Values (CSV),[129] Extensible Markup Manguage (XML),[130] or JavaScript Object Notation (JSON)[131] may be suitable. However, many data sets require

the use of more complex data storage implementations such as Structured Query Language (SQL),[132] DataFrame,[133] or even an entirely custom format. Although data storage and retrieval may seem to be a trivial portion of the design, even a single 10-bit, 100 MHz digitizer (which is ubiquitous in modern day technology) can fill 8 GB of memory in just over a minute. An 8-bit, 4 GHz digitizer found in many commercial TOFs can fill the same 8 GB in just 2 seconds.

Software platforms exist for handling complex data, such as MATLAB[134] and R,[135] which can handle very large data sets and come equipped with powerful statistical tools. However, many complex MS data sets have experiment-specific information encoded in what is referred to as the "meta-data" that is ignored by generic software or lost in the data conversion step. As such, specialized analysis software may be required and can necessitate extensive development time.

1.4 Mass Spectrometers Imaging

Mass spectrometry imaging (MSI) is a special class of mass spectrometry where mass spectral images are recorded in which every pixel corresponds to a mass spectrum. Applications of MSI primarily extend to the fields of material science, where surface characteristics can be analyzed for their chemical composition,[136] and analysis of biological tissues, where tissues are analyzed for their fundamental and medically-relevant properties.[75] Recent efforts have been made towards coupling standard mass spectrometers with spatially-aware sampling techniques[137-138] to perform MSI, but these approaches are beyond the scope of this discussion. In this section, only techniques utilizing a primary photon or ion beam are discussed.

1.4.1 Secondary Ionization Mass Spectrometry (SIMS)

As discussed previously in Section 1.2.1.3, Secondary ionization mass spectrometry (SIMS) is an MSI technique wherein a high-energy beam of ions is bombarded against material to produce ions.[26] SIMS is generally considered to be a destructive analysis technique that is primarily utilized in material analysis.

Three principal classes of ion guns, commonly referred to as a focused ion beams (FIBs), are utilized in SIMS and differ primarily in their mechanism of generating ions. Once ions are generated, beam focusing and rastering is handled mostly the same across ion gun types. The first class, known as liquid-metal ion source (LMIS), operates by heating a metal to its liquid state and extracting ions *via* a high-voltage electric field.[139] Metals such as gallium, gold, germanium, and iridium are utilized in LMISs and primarily produce monoatomic ion beams capable of focusing down to a few nanometers.

The second class of ion guns are the plasma FIBs, where a gas (xenon, C_{60}, argon, helium, and many more) is passed through a plasma to generate ions which are then extracted for focusing/acceleration. The unique benefit of plasma FIBs is that they can produce ion beams of practically any element. However, plasma FIBs lack brightness when compared to other ion sources.[140]

The third class of ion guns are known as gas cluster ion beams (GCIBs). GCIB ion guns operate *via* jet expansion of an inert gas (such as argon) resulting in very low energy gas clusters. These gas clusters are then ionized by crossing through a beam of electrons to undergo electron ionization (see section 1.2.1.1) and are extracted by an electric field for focusing/acceleration. GCIBs are a popular technique used for imaging of biological tissue due to the large surface area resulting in less surface damage and thus preserving

biomolecules during ionization.[141] However, GCIBs lack the spatial resolutions achievable by LMIS and plasma FIBS.[142]

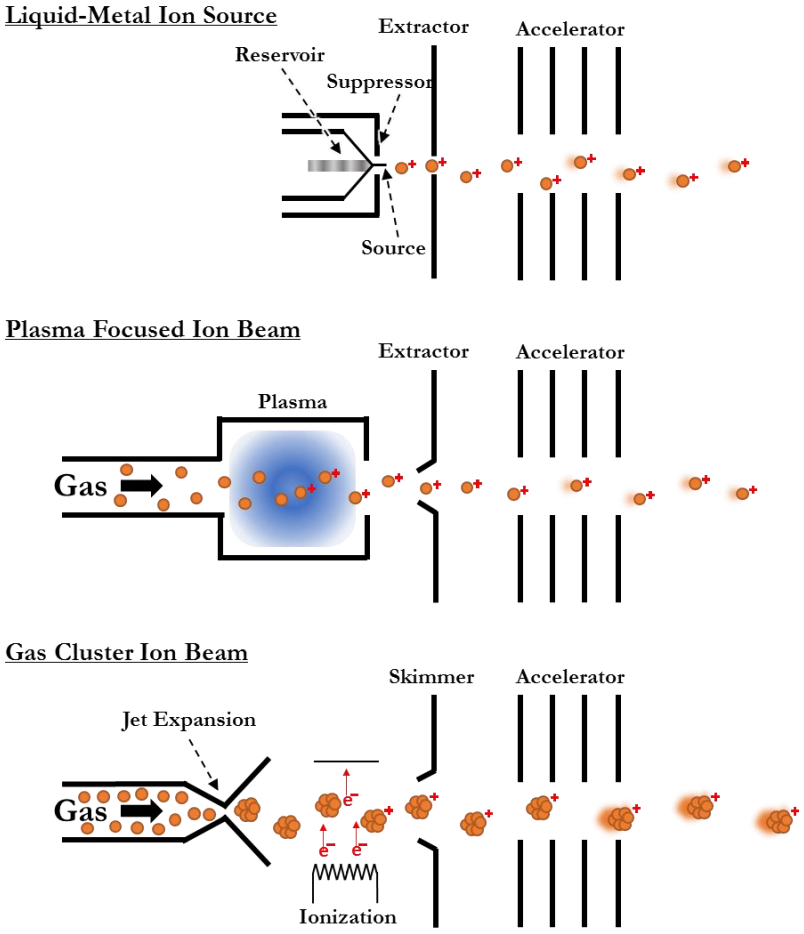

Scheme 1.4. Schematic representation of the three primary classes of focused ion beams: liquid metal ion source, plasma focused ion beam, and gas cluster ion beam.

1.4.2 Matrix Assisted Laser Desorption/Ionization (MALDI)

As discussed previously in Section 1.2.1.3, MALDI is a solid phase ionization technique in which a sample is coated in a matrix designed to absorb laser radiation at certain wavelengths. The matrix (often a molecule that contains an aromatic core and one or more conjugated bonds, such as cinnamic acid or naphthalene-like compounds) absorbs the laser radiation (often at 337 nm) and converts the radiation into thermal energy.[38] The

sudden rise in thermal energy causes an ablation event (i.e., the sample and some of the matrix are transported from the solid phase into the gas phase) as well as an ionization event whereby charged portions of the MALDI matrix react (generally *via* one or possibly more proton transfers) with the substrate analyte.[143-144]

The combination of these events with the highly soft nature of MALDI can yield large *m/z* values (> 20,000 *m/z*) with intact molecular information.[145] The large *m/z* values combined with the relatively high vacuum compatibility of MALDI (sometimes performed in ~10 mTorr or less) and the highly-synchronized initiation of the ionization and vaporization event result in MALDI being naturally paired with TOF MS. Some of the most common solid-phase MS instruments are, in fact, MALDI-TOF MS instruments. However, MALDI has also been pared with other forms of MS, including FT-ICR MS.[146-147]

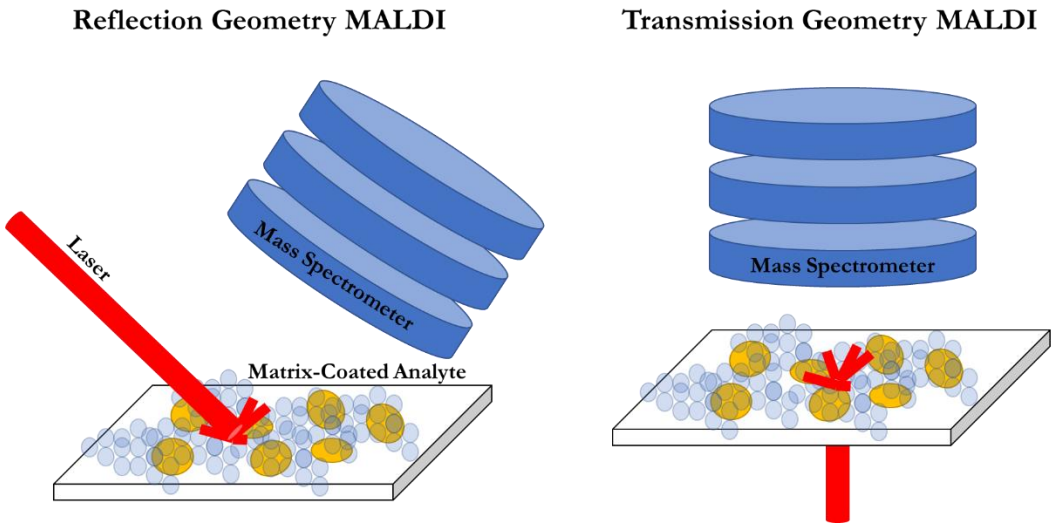

Scheme 1.5. Schematic representations of reflection (left) and transmission (right) geometry MALDI ion sources.

Scheme 1.5 depicts two differing configurations that correspond to MALDI-MS instruments. The first (Scheme 1.5, left) is a reflection geometry MALDI where the laser

simply impacts the matrix-coated analyte, causes an ablation event, and the resultant ions are extracted into the MS instrument. The second (Scheme 1.5, right) is a transmission geometry MALDI where the laser is positioned behind the sample and a transparent "slide" allows the laser light to ablate the underside of the analyte-matrix mixture. MALDI is often performed in reflection geometry MALDI, as samples can be of thicknesses that would be infeasible for transmission geometry MALDI. Additionally, in reflection geometry MALDI the matrix can be applied only on-top of the sample. However, the main advantage of transmission geometry MALDI is highly-efficient sample transfer in atmospheric conditions.[148] This highly efficient sample transfer can be taken advantage of by other techniques, such as laser ablation-capture (discussed below).

1.4.3 Laser Ablation-Capture

An alternative method of solid-phase analysis utilizing lasers is laser ablation-capture MS.[149] In laser ablation-capture MS, a thin section of a sample (often a tissue) is placed on a thin, glass slide. A laser (often an IR laser instead of the UV laser that is common to MALDI imaging) is used to ablate the sample material (often in a configuration similar to the transmission geometry MALDI displayed on the right of Scheme 1.5). However, instead of direct transfer of the ablated material to the MS instrument, the ablated material is "captured" (often in a simple microcentrifuge tube).[149-150] This captured material is then dissolved in a liquid solvent (as the samples are often tissues, this solvent is often water to avoid unwanted changes to the ablated material). The liquid solvent may be stored, transported, and prepared as any other (dilute) liquid sample. Thus, (although the timescales are lengthened from minutes–hours to days–months for analysis) a tissue can undergo MSI with added LC and/or IM separation axes. Due to the extreme lengthening of

timescales, as well as the enhanced signal intensity achieved when combining larger amounts of ablated material, it is common for laser ablation-capture MS to involve a step where regions of interest (ROI) are first selected and then each region is individually ablated.[151]

1.5 Author Contributions

One-hundred percent of the results presented in Chapters Three (including Appendix A) and Four (including Appendix B) were generated by Matthew R. Brantley. For Chapter Three, ninety percent of the text was authored by Matthew R. Brantley, the remaining ten percent was contributions from Raul Villacob and Touradj Solouki of Baylor University. Seventy percent of the text in Chapter Four was authored by Matthew R. Brantley, the remaining thirty percent was contributions from Ian G. M. Anthony and Touradj Solouki of Baylor University.

CHAPTER TWO

Design Considerations and Implementation of a Custom Imaging Mass Spectrometer

2.1 Experimental Design

In this section, an in-depth discussion into the theory of operation, preliminary results, and the benefits and drawbacks of this instrument are discussed. The described imaging mass spectrometer must balance spatial resolution with "hardness" of ionization. A typical eukaryotic cell is approximately 10 to 100 µm in diameter.[152] Because the goal of this instrument was biomolecule analysis at sub-cellular resolutions, spatial resolutions of lower than 1 µm are required. Additionally, the interest in biomolecules necessitates the use of soft ionization techniques.

Table 2.1. Comparison of resolution and ionization hardness for common MSI techniques.

MSI Technique	Resolution (spatial)	Soft/Hard Ionization
MALDI	50-200 µm[153]	Soft
Liquid Sampling	200-500 µm[154]	Soft
Laser Ablation	150-350 µm[155]	Soft
Monoatomic SIMS	5-50 nm[156]	Hard
Cluster SIMS	1-5 µm[157]	Soft/Hard

As shown in Table 2.1., no existing MSI technique is capable of sub-micron spatial resolution with soft ionization. As such, the instrument described herein explores new ionization mechanisms for use with monoatomic SIMS.

2.1.1 Theory of Operation

The described imaging mass spectrometer has three operating modes, each providing a different type of information about a sample. In all three cases, a high energy Ga^+ FIB is directed towards a solid-phase sample. In the first operating mode (focused ion beam-scanning electron microscopy (FIB-SEM)), Ga^+ ions bombard the surface in a high energy process resulting in the release of electrons. These electrons are then attracted to the positive-potential bias applied to the continuous dynode electron multiplier (CDEM) detector grid and subsequently amplified by the electron multiplier (see Section 1.2.3.1). This operating mode allows for Scanning Electron Microscopy (SEM) when the Ga^+ beam is rastered and a demonstration of this can be seen in Section 2.3.1.

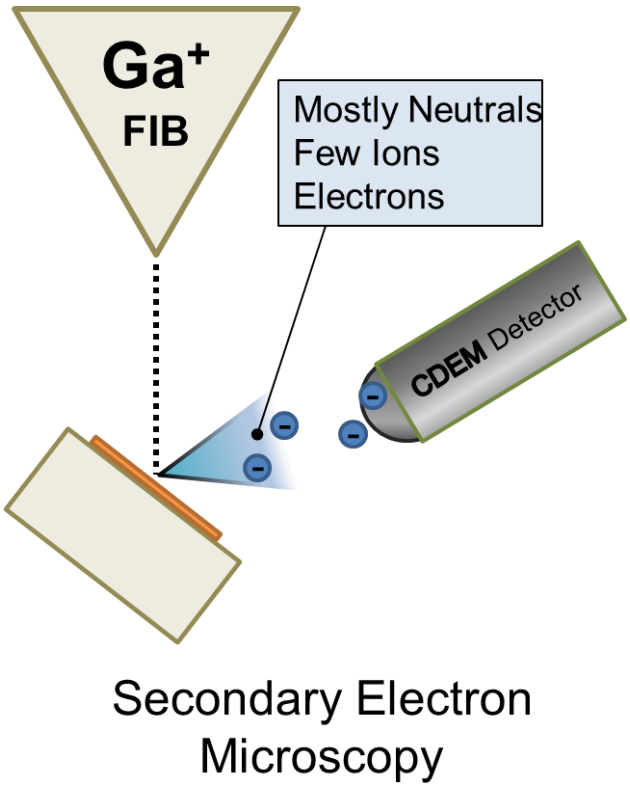

Figure 2.1. Pictorial representation of the instruments Scanning Electron Microscopy operating mode.

In the second operating mode (SIMS), ions generated from the high-energy Ga^+ ablation process are extracted by the ion optics (see Section 2.2.2) of the mass spectrometer for transmission to the FT-ICR mass analyzer (see Section 1.2.2) for mass measurements. The SIMS operating mode of the described instrument can be seen pictorially in Figure 2.2. As it is likely to be an extremely "hard" ionization process, the SIMS operating mode of this instrument would primarily be utilized to study distributions of heavy metals.

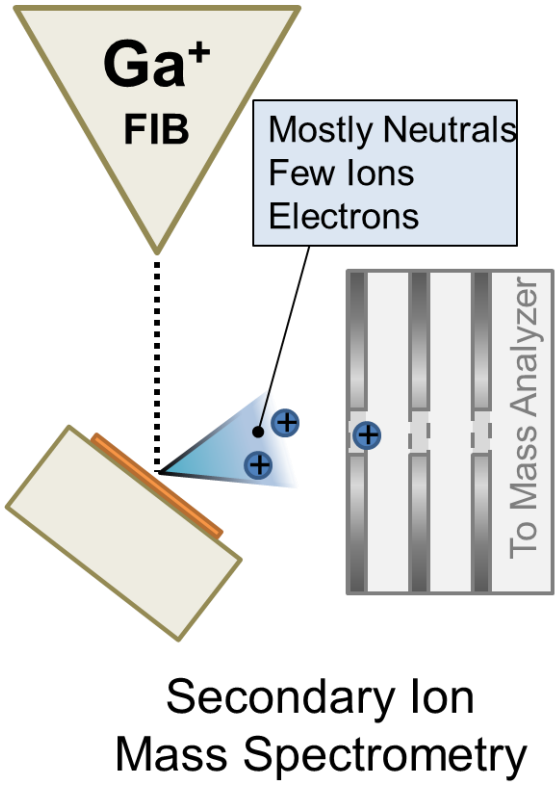

Figure 2.2. Pictorial representation of the instruments Secondary Ion Mass Spectrometry operating mode.

The third operating mode, RFI Post-Ionization Mass Spectrometry, is what necessitated the construction of this instrument due to RFI Post-Ionization Mass Spectrometry's unique instrumental constraints. However, this proposed mechanism can potentially overcome the "hardness" limitations of SIMS and allow biomolecule analysis

at sub-cellular spatial resolutions. In this operating mode, the ions and electrons generated from the Ga^+ ablation event are not utilized. Instead ionization of the ablated neutral molecules is performed prior to MS analysis. Ga^+ FIBs are excellent at milling due to their high sputter yield but are highly destructive to the sample.[83, 158] However, the high sputter yield of Ga^+ FIB could contain a significant population of neutral molecules which remain undamaged (i.e., retain their molecular information) in the Ga^+ ablation process (as the effective ablation area is larger than the focused Ga^+ beam diameter).

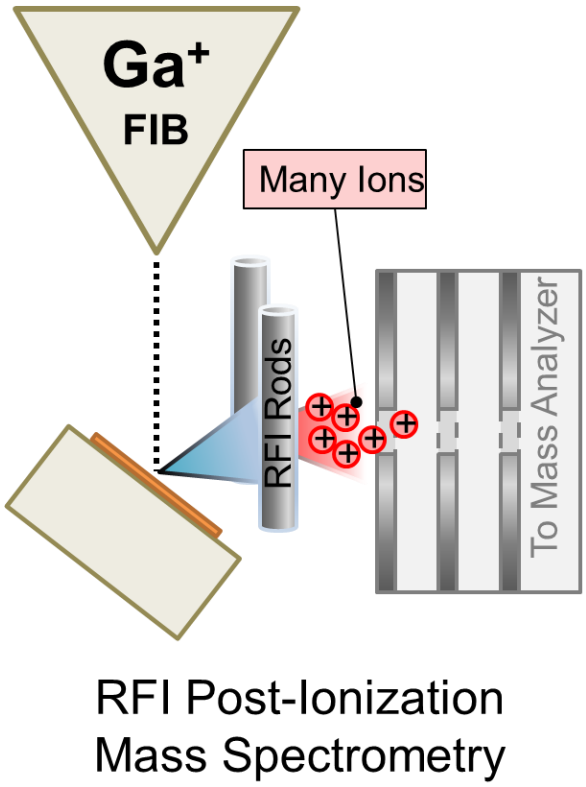

Figure 2.3. Pictorial representation of the instruments RFI Post-Ionization Mass Spectrometry operating mode.

2.1.2 Benefits of Proposed Experiment

The described instrument can operate in three unique modes, each of which provides unique information about the sample.

The operating speeds of FIB-SEM and FT-ICR SIMS are orders of magnitude different (FIB-SEM is far faster) and, as such, have different instrumental requirements for their operations. To account for the high speed of FIB-SEM, a high-speed raster system was assembled which utilized the deflection optics of the Magnum Ga^+ column. This raster system allowed for image collection on the order of 100s of milliseconds. However, FT-ICR experiments can sometimes take a few seconds to complete and thus beam stability by using the deflection optics was a concern. This was addressed by the inclusion of a high-precision electromechanical positioning system for use when operating in SIMS mode (see Section 1.2.1.3).

The proposed post-ablation ionization mechanism is RFI which, unlike other electron ionization techniques, is capable of pulsed operation. Furthermore, this technique is not known to generate a significant amount of light or heat, unlike thermionic emitters which would emit potentially damaging photons onto the sample. The sample can be protected from electrons through the use of stage bias voltages.

2.1.3 Drawbacks of Proposed Experiment

As with all instrumentation, the described instrument comes with certain drawbacks. The most immediate drawback is that the vacuum requirement for operation of the ion source (<10E-6 Torr) is significantly higher than what is typically used for the analysis of biological samples. To accommodate for this, tissues must be specially prepared

for exposure to vacuum; however, a research has been done in this area and can be addressed for most samples.[159]

The post ionization mechanism included in this design is RFI, which has been demonstrated to be an electron-based ionization technique.[51] Electron-based ionization techniques are notably "hard" ionization techniques, thus the resulting mass spectral information can be highly convoluted. However, this concern is mostly addressed by the high mass-resolution of the FT-ICR analyzer. Understanding of the principles of RFI electron generation remains minimal, thus source design is likely unoptimized (the RFI electrode assembly on the ion optics was designed in a modular manner to account for this).

Use of an FT-ICR as the mass analyzer greatly limits the duty cycle, a highly-important parameter when performing mass spectrometry imaging. Initially justifiable due to the availability of an existing, functioning FT-ICR, complications arose very early when the electronics of the initially proposed FT-ICR had a critical failure and were unable to be repaired. To remain within budget constraints, reconstruction of the FT-ICR using new electronic components was the selected option.

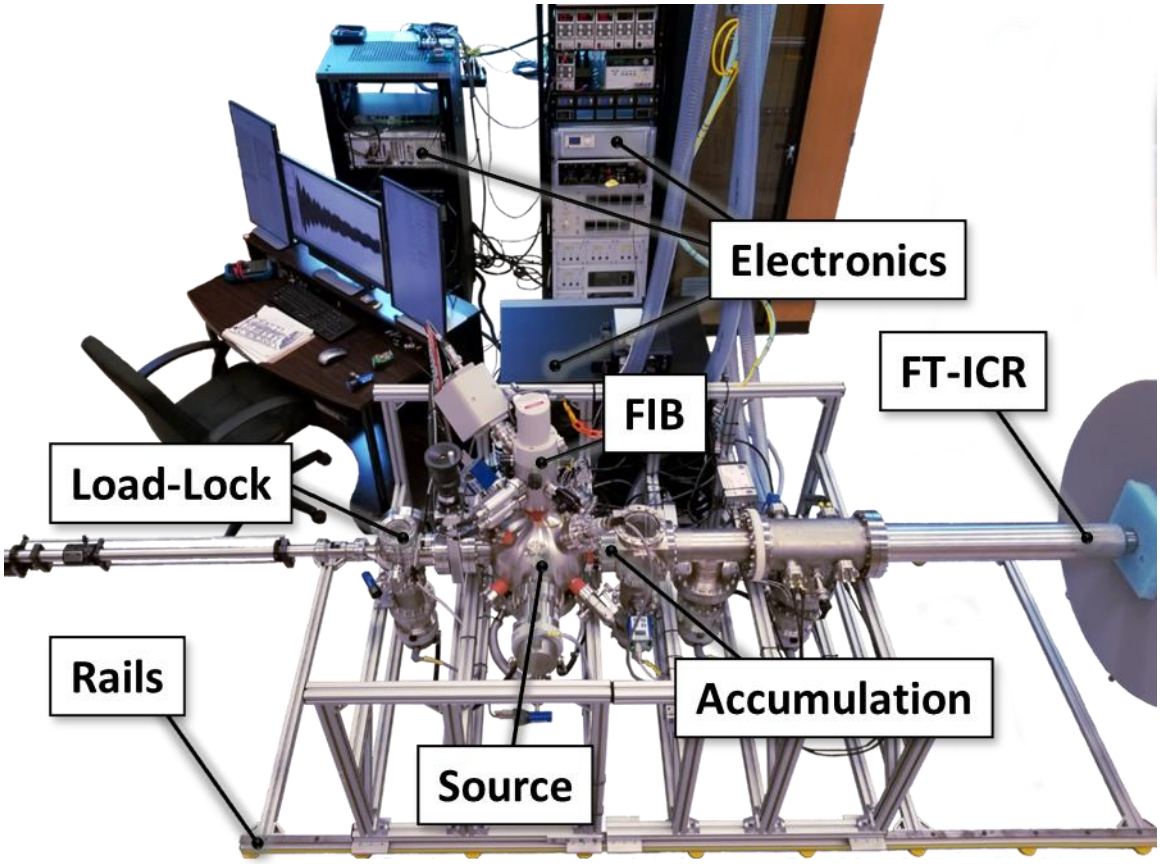

Figure 2.4. Image of the assembled FIB-SEM/FT-ICR imaging mass spectrometer with key components labeled.

2.2.1 Vacuum System

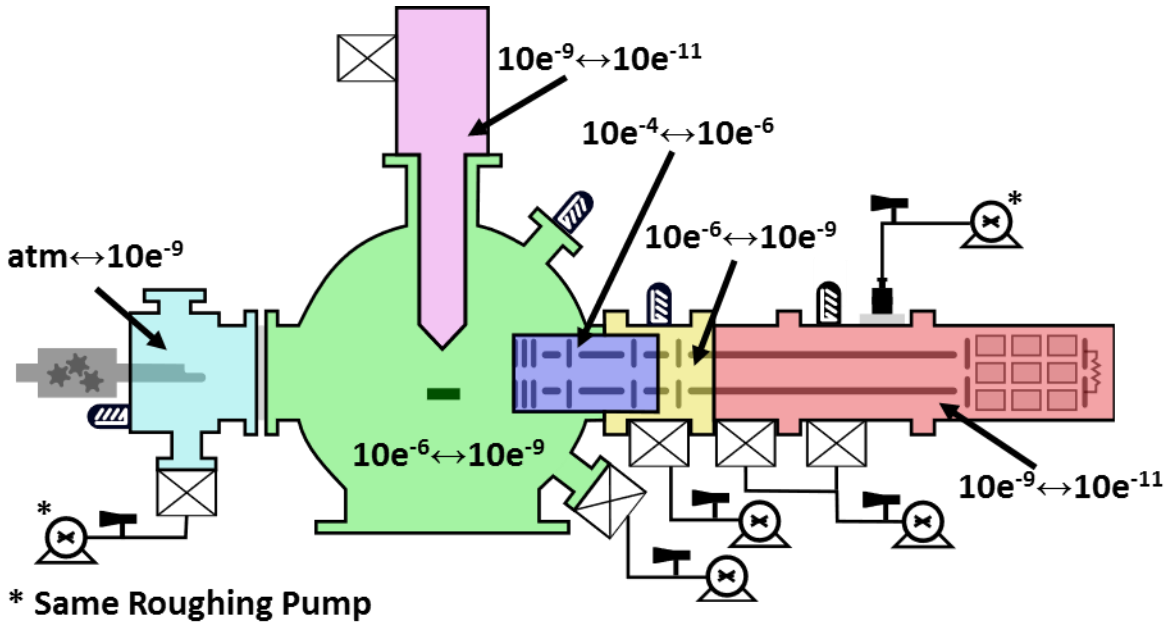

Figure 2.5. Schematic representation of the instrument vacuum chambers with vacuum regions colored and labeled for their respective pressure regime. Cyan: Load-Lock Chamber, Green: Source Chamber, Pink: FIB Column, Purple: Accumulation Region. Yellow: Transfer Chamber, and Red: ICR Chamber.

2.2.1.1 Instrument vacuum regions. A total of six pressure regions exist within the instrument. The Load-Lock Chamber region Figure 2.5; cyan) is separated from the rest of the chamber by a gate valve and has a separate door for loading/unloading samples. A turbomolecular pump (Pfeiffer Vacuum TMU 260) and roughing pump (Welch 8905 Rotary Vane) supply vacuum to the Load-Lock Chamber when necessary for pump down before opening the gate valve. Additionally, the Load-Lock Chamber can be vented to atmosphere (only whenever the gave valve is closed). Load-Lock Chamber pressures are measured from atmosphere to ultra-high vacuum (UHV) using an ion gauge (KJL 392) and Pirani gauge (KJL 275i).

The Source Chamber region (Figure 2.5; green) is where sample ablation occurs and is evacuated by a dedicated turbomolecular pump (Pfeiffer Vacuum TMU 260) and roughing pump (Welch 8905 Rotary Vane). Pressure measurement is performed using an ion gauge (KJL 354i) and convectron gauge (KJL 275i). Many electrical feedthroughs are necessary for the sample stage, CDEM detector, etc. that are housed inside the Source Chamber. For all components mounted to the bottom flange (10-inch Conflat®), feedthroughs were custom installed on the same flange. Additional electrical connections are supplied through various other flanges attached to the hemispherical source chamber.

Attached to the top of the Source Chamber is the FIB Column (Figure 2.5; pink) wherein the internal components of the Ga^+ LMIS are housed, such as the source, apertures, lenses, etc. UHV is achieved in the FIB Column by use of ion getter pump (Duniway Stockroom 35 L/s). Unlike the other chamber regions, the FIB Column region does not have a dedicated roughing pump and the ion getter pump cannot be turned on until vacuum of at least $1x10^{-5}$ torr has been achieved. A column isolation valve (CIV) allows isolation of the FIB Column to the Source Chamber and is opened during column use and initial pump down. The Source Chamber vacuum system can get the FIB Column vacuum to the required $1x10^{-5}$ torr when the CIV is opened, allowing for the ion getter pump to be started. Pressure measurement is accomplished using the ion getter pump as well, where the current generated by ions depositing in the getter material is proportional to the pressure (in the same manner as a cold-cathode ionization gauge; see Section 1.3.1)

The Accumulation Region (Figure 2.5; purple) contains the accumulation quadrupole which relies on a relatively higher pressure ($1x10^{-4}$ to $1x10^{-6}$) for collisional cooling of ions inside a potential well, thus accumulating them. A leak valve (MDC

Sapphire) was modified to terminate internally with a 1/16" copper tubing that fed directly into the Accumulation Region through a small Swagelok® fitting, providing the necessary gas flow. The Accumulation Region is fully enclosed with a 316L stainless steel shroud and is opened at both ends with 4mm orifices which serve as conductance limits. Because of design restrictions, no pressure measurement was feasible in this region.

The Transfer Chamber (Figure 2.5; yellow) separates the Accumulation Region from the ICR Chamber and serves as a differential pumping region, with a 4 mm orifice between itself and the Accumulation Region and a 3 mm orifice between itself and the ICR chamber serving as conductance limits. The Transfer Chamber vacuum is provided by a dedicated turbomolecular pump (Pfeiffer Vacuum TMU 260) and roughing pump (Welch 8905 Rotary Vane). Pressure measurement is performed using an ion gauge (KJL 354i) and pirani gauge (KJL 275i).

The ICR Chamber (Figure 2.5; red) is the longest of the vacuum chamber regions and has the highest vacuum requirements which are discussed in more length in Section 2.2.1.2. To maximize the vacuum achieved, two turbomolecular pumps (2x Pfeiffer Vacuum TMU 260) were dedicated to the ICR chamber region, with both being backed by a roughing pump (Welch 8905 Rotary Vane). Pressure measurement is performed using an ion gauge (KJL G100F Nude Gauge) and Pirani gauge (KJL 275i).

2.2.1.2 Vacuum requirements for ICR. Higher vacuum increases the distance between collisions (known as mean free path) and, because of the nature of the ICR mass analyzer (see Section 1.2.2.3), ion flight paths during a single detection event can readily exceed a few kilometers. Mean free path can be calculated as follows:

Equation 2.1: $$\bar{\imath} = \frac{k \cdot T}{\sqrt{2} \cdot \pi \cdot p \cdot d_m^2}$$

Where $\bar{\iota}$ is the mean free path, k is the Boltzmann constant, T is the temperature (in Kelvin), p is pressure (in pascals), and d is the effective diameter of the molecules (in meters). At UHV, the residual gas composition is primarily H_2 due to outgassing/permeation from stainless steel[160] and the limited H_2 compression ratio of the TMU260 turbomolecular pumps ($1.3x10^4$ for H_2 compared to $>1x10^9$ for N_2). Thus, the mean free path for H_2 can be used to represent the mean free path of residual gas in this vacuum system.

Table 2.2. Mean free path of H_2 particles calculated at various pressures.

Pressure (Torr)	Mean Free Path (km)
1.00E-05	0.0088
1.00E-06	0.0879
1.00E-07	0.8794
1.00E-08	8.7944
1.00E-09	87.944
1.00E-10	879.44
1.00E-11	8794.4

The mean free path metric only accounts for collisions between H_2 molecules and does not represent the free path between an ion (which typically has collisional areas significantly larger than H_2) and H_2. However, dividing mean free path by the ratio of analyte-to-H_2 collisional cross sections can provide a rough approximation for ICR measurements. For example, the cross section of Benzene is 0.88 nm^2 (compared to H_2 at 0.27 nm^2), reducing the mean free path calculation for a given pressure by approximately three.

2.2.2 Ion Optics

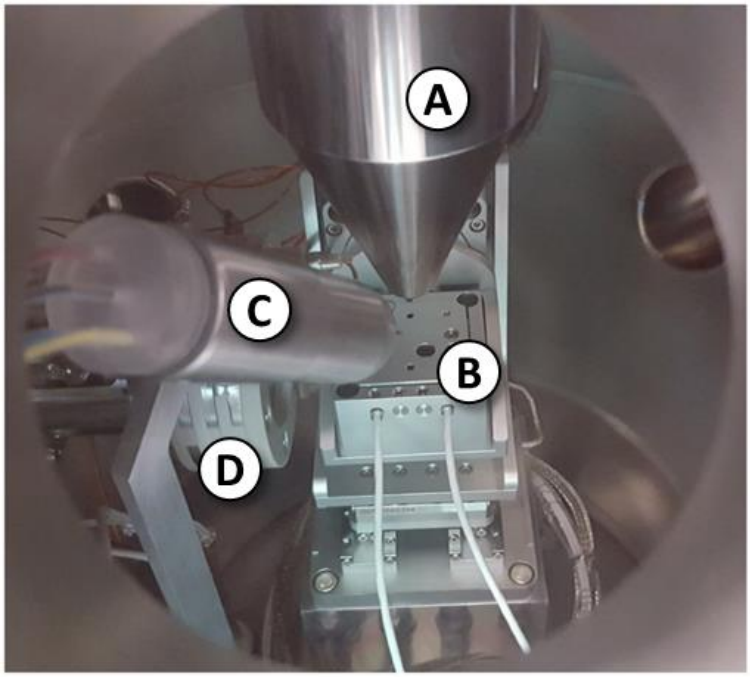

Figure 2.6. Photo of the ionization source chamber with key components labeled. A - FIB column, B – sample positioning stage, C – CDEM detector, D – ion extraction optics.

2.2.2.1 Ion source. Ions and electrons generated using the Ga^+ LMIS and RFI (see Section 2.1.1) can be directed towards either the CDEM or mass spectrometer depending on the experiment of interest. For secondary electron (or ion) imaging, the collector grid of the CDEM detector is biased to a sufficient voltage (± 500 V) to attract electrons or ions. For electron imaging, the orientation and position of the sample has minimal impact on sensitivity as long as there is a clear path from the site of generation to the CDEM. However for mass spectral imaging, the sample stage is rotated 45 degrees relative to the FIB and ion extraction optics (see Figure 2.2 and Figure 2.3) to maximize ion throughput.

2.2.2.2 Ion extraction and accumulation. Ion extraction and accumulation are critical steps in the transport of ions generated in the source to the mass analyzer. A set of three rings acts as an ion funnel with a large acceptance region to accommodate for ion

spread. For post-ablation ionization, the RFI rods are positioned between the sample and the entrance lenses. Once extracted and focused by the extraction lenses, ions are guided through a series of RF-only quadrupole ion guides before reaching the FT-ICR mass analyzer.

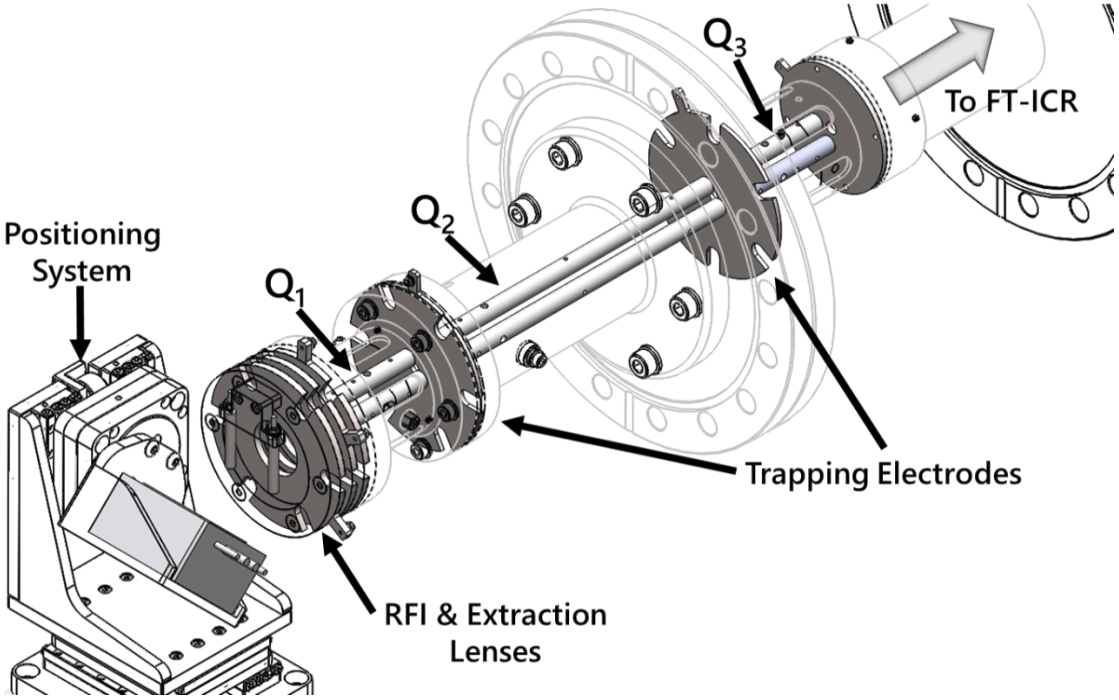

Figure 2.7. Perspective view of the ion extraction and assembly optics with various components labeled.

FT-ICR mass analyzers are pulsed-operation analyzers, thus ions must be supplied to the mass analyzer only at the beginning of each analysis cycle. However, the ionization methods available on this instrument are capable of continuous operation. External accumulation[161] is the established method of accommodating for this duty cycle mismatch in FT-ICRs and also serves to increase sensitivity. Continuous external accumulation is performed in this system in the accumulation cell (Figure 2.8) which is filled with an inert gas at pressures between $1x10^{-4}$ and $1x10^{-6}$ Torr and contained inside a stainless-steel shroud. For ions entering and exiting the accumulation cell, trapping lenses serve as

conductance limits (Figure 2.7; 4 mm orifices) that allow focused ions through but limit the release of gas to the adjacent vacuum regions. RF-only ion guides before and after the accumulation cell were equipped with slotted shrouds to increase gas permeation and assist with differential pumping.

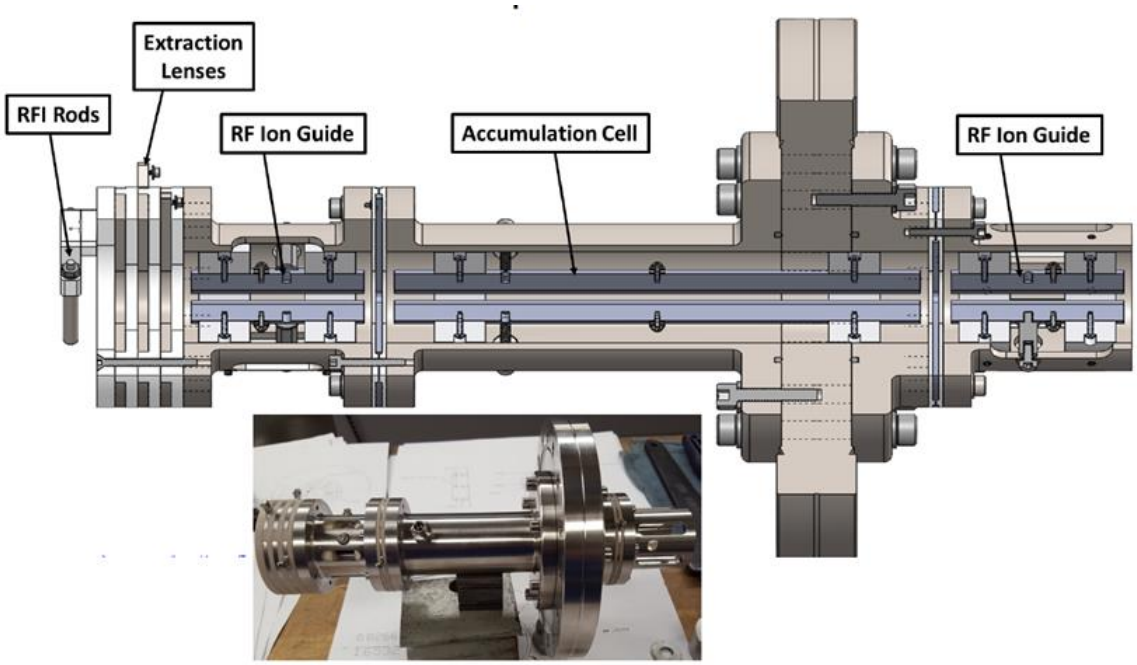

Figure 2.8. Perspective render of the ion extraction and accumulation assembly with select components labeled. Inset shows image of the ion extract and accumulation assembly fully constructed.

Positioning of the extraction lenses proximal to the sample stage required that the extraction and accumulation assembly be constructed on a Conflat® flange, which can be seen in Figure 2.8. In addition, the transfer quadrupole of the FT-ICR mass analyzer reached only part-way into the Transfer Chamber which also necessitated construction on a flange. To accommodate both requirements with minimal addition to the ion flight path, it was decided to use a single, double-sided Conflat® solution that can be seen installed on Figure 2.9. Electrical connections were provided using feedthroughs located on the Source

Chamber; however, new flange designs from Ardara have been introduced which incorporate feedthroughs onto the outer ring of the flange.

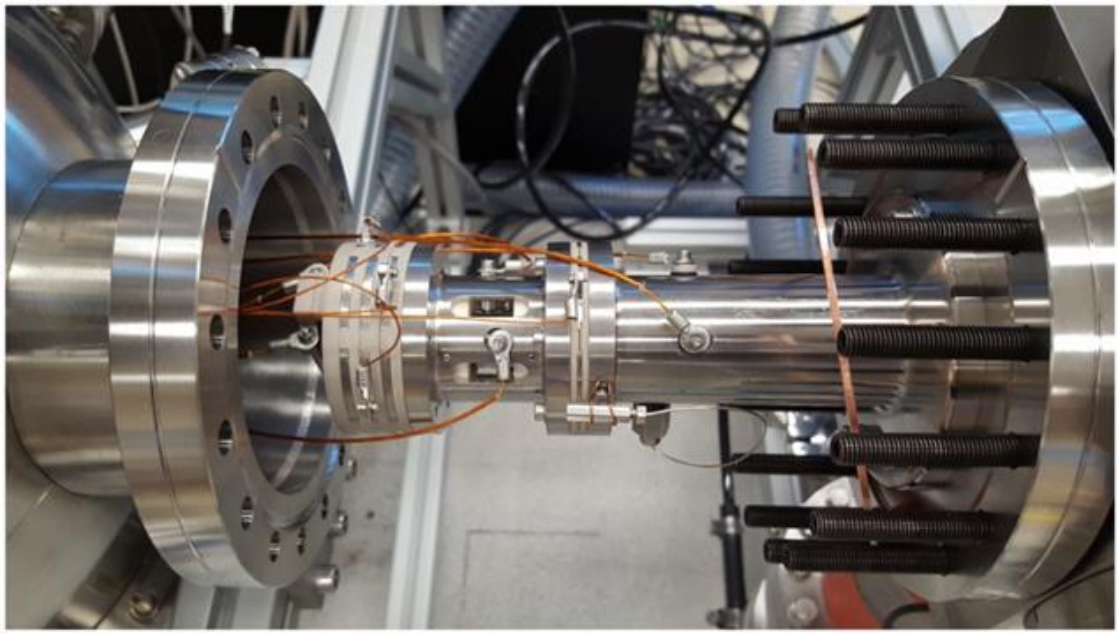

Figure 2.9. Image of the ion extraction and accumulation assembly installed with electric connections in place.

In addition to providing a minimal ion flight path between the sample and the transfer quadrupole of the FT-ICR mass analyzer, the extraction and accumulation assembly serves as the only mechanical connection between the Source Chamber and the Transfer Chamber as both were constructed on individual carts. As such, separation at the ion extraction and accumulation assembly allows access to internal components within the ~13-foot vacuum chamber.

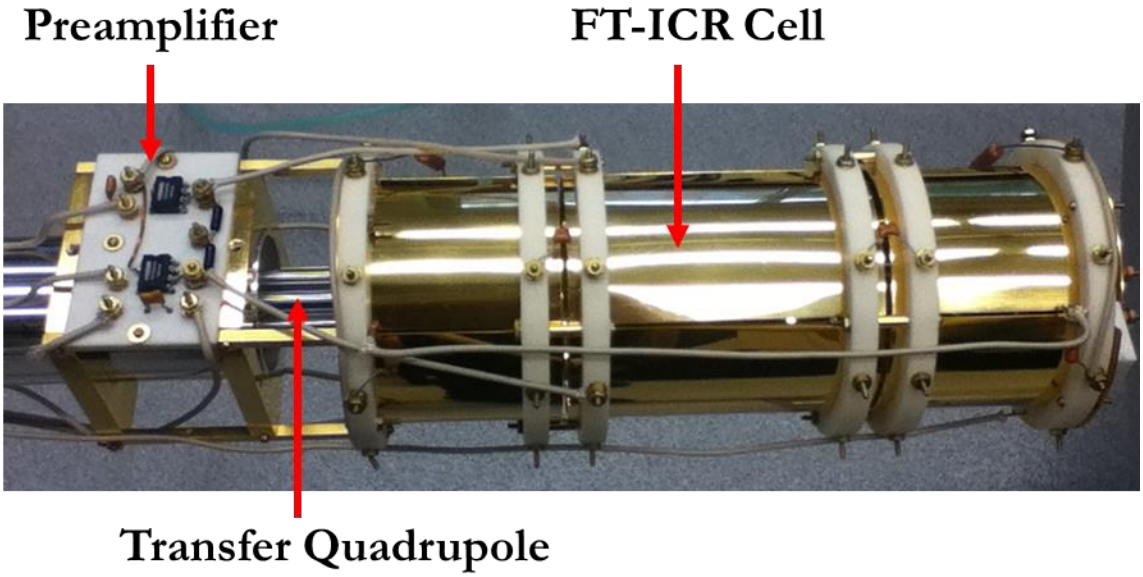

Figure 2.10. Image of the ICR cell, pre-amplifier, and transfer quadrupole outside of the vacuum chamber.

2.2.2.3 Mass analyzer. The mass analyzer utilized in this instrument was an FT-ICR recovered from an IonSpec FT-ICR instrument which was initially utilized as a GC/FT-ICR MS. The recovered portion of the instrument included a vacuum chamber with a ~3-foot-long transfer quadrupole, a preamplifier, and an FT-ICR cell. The FT-ICR cell is a segmented cell design in which three sets of four-electrode-rings are sandwiched between two trapping electrodes. The outermost rings (called the inner trapping rings) are configured for a DC bias potential while also capacitively coupling the top and bottom plates to the excitation plates for increased excitation homogeneity.

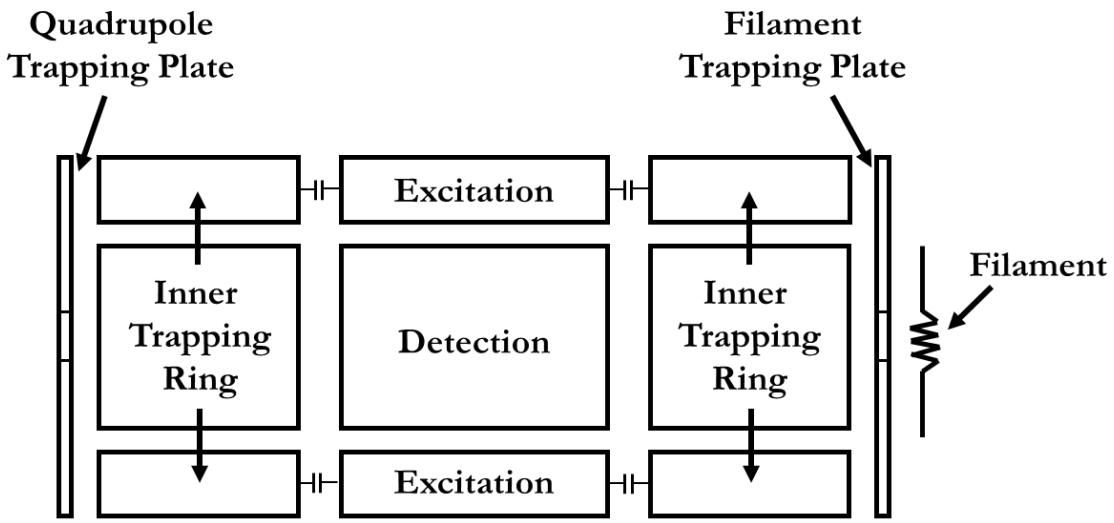

Scheme 2.1. Schematic representation of the ICR cell with individual electrodes labeled.

2.2.2.4 Focused ion beam. The focused ion beam's ion optics allow for the extraction, alignment, and focusing of the monoatomic Ga^+ ions onto the sample within the source chamber with high accuracy and narrow spot size (as low as 7 nm beam width). Directing ions with such precision requires high electric fields, precise geometries, and proper tuning. Details into how Ga^+ ions are initially generated from the Ga^+ source can be read in Section 1.4.1 as the Ga^+ LMIS (FEI Magnum BDS50) used in this instrument follows the same principles.

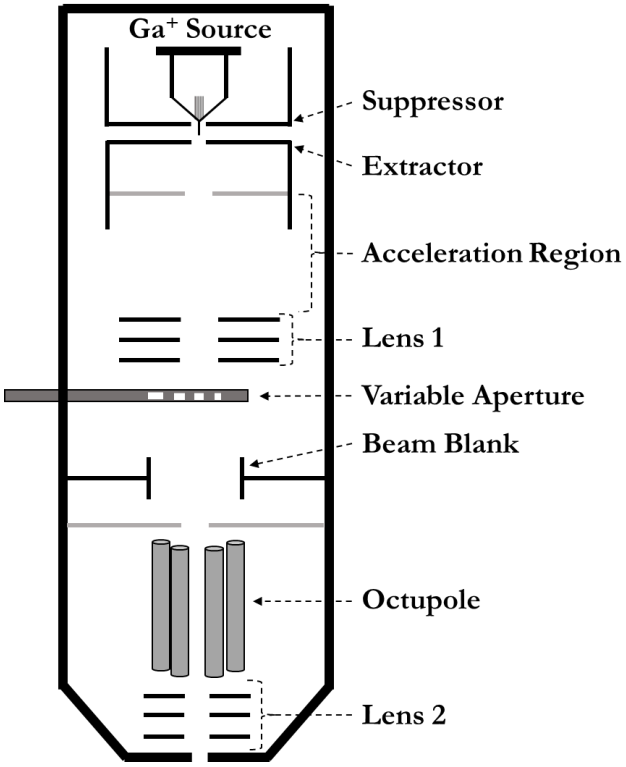

Scheme 2.2. Schematic representation of the FEI Magnum Ga^+ focused ion beam utilized in this instrument. The acceleration region describes a region of significant potential difference but does not refer to a specific electrode(s). Lens 1 and Lens 2 refer to discrete sets of 3 lenses which are electrically connected.

For this particular LMIS, the extractor voltage is held at a constant 12 kV to ensure sufficient V/cm for field emission of Ga^+ ions. However, without any additional electric fields present, the emission current (measured on the extractor electrode as induced current; see Section 1.2.3.1 on Faraday cups) would be too high and the source would quickly deplete. The suppressor can reduce emission current by applying a retarding electric field while not actually effecting the V/cm between the Ga^+ emitter tip and the extractor. For this column, all operations are based on a source emission current of 2.2 μA which is held constant by real-time adjustment of the suppressor potential.

Ions leaving the extractor are then exposed to a high acceleration field, between 1-30 kV depending on the desired beam current and size. After acceleration, ions are focused

in lens 1 onto a set of mechanical apertures. The mechanical aperture consists of a metal strip with holes of various diameters cut through it. Depending on the size of the hole, more or fewer Ga^+ ions will make it through the aperture. The aperture size is adjusted manually using micrometers on the exterior of the ion column. Specific combinations of acceleration voltage, aperture size, and lens 1 voltage determine the final beam diameter and are tabulated below for 30 kV at 19.4 mm working distance.

Table 2.3. Beam Column Settings for 30 kV Acceleration and 19.4 mm Working Distance

Beam Current (nA)	FW50 Beam Size (nM)	Lens 1 (V)
0.001	7	10000
0.01	12	14500
0.03	16	16000
0.05	19	17500
0.1	23	21500
0.3	33	24500
0.5	39	25000
1.0	50	25500
3.0	81	27500
5.0	110	28300
7.0	141	28500
20.0	427	28500

After the aperture are the beam blank electrodes that, when enabled, deflect the Ga^+ ion beam into an aperture which is connected to an external BNC terminal for measurement. Beam blanking is utilized to preserve sample life when Ga^+ contamination is of concern and for diagnostic purposes to ensure correct beam current is achieved (such as when manually adjusting the mechanical aperture). The beam blank can operate as fast as 100 kHz, thus enabling rapid beam blanking for milling applications.

The octupole behaves differently in the ion column than it would in a mass spectrometer. Instead of creating a containment field in which ions are radially confined

by a high frequency AC signal, the octupole here uses DC potentials to adjust the beam shape and direction and has several operating modes which are superimposed to produce the desired beam operation. Beam shift in the X or Y direction is accomplished by adjusting the dipole modes and can be rotated by changing which physical electrodes the dipolar field is applied to. Depth of field for beam raster is achieved by adjusting the magnitude of beam shift.

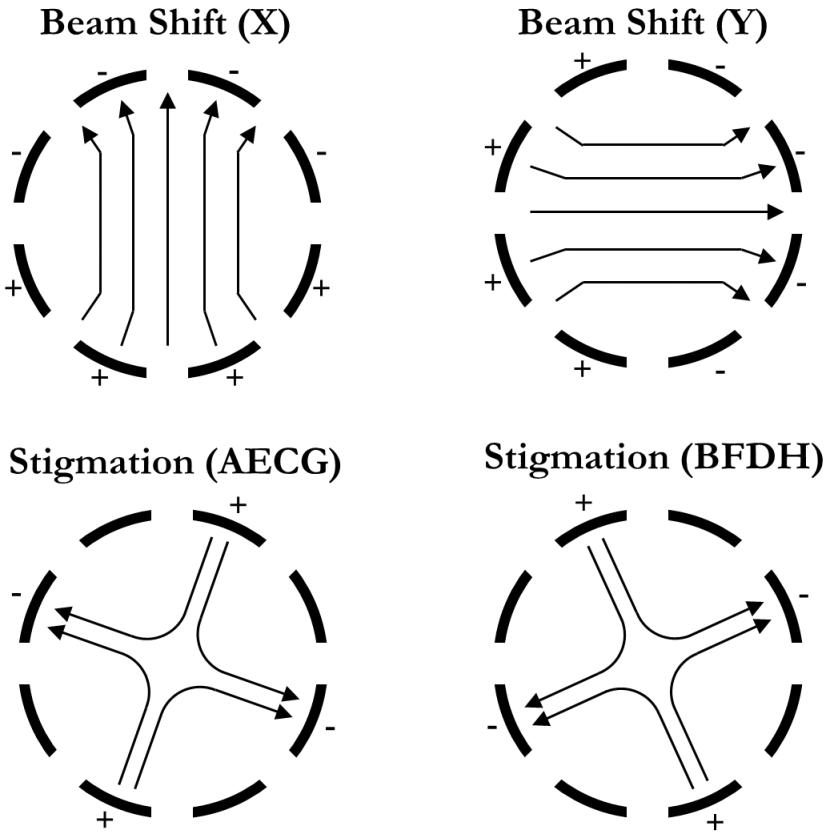

Figure 2.11. Octupole deflection modes.

The stigmation modes are for correction of astigmatism (*i.e.*, beam crossover point is divergent for the X and Y axis or other shape irregularities). Two quadrupolar fields, AECG and BFDH, are positioned 45° apart and are adjusted independently to achieve ideal beam shape. After beam shaping and deflection, lens 2 is used for focusing the Ga^+ ions

onto the sample by adjusting the crossover point. Maximum resolution is achieved for a given beam current only when stigmation and focusing are properly adjusted.

2.2.2.5 Ion trajectory simulations. Ion trajectory simulations were utilized to guide instrument design and to find optimized fields for ion transmission. However, difficulties in rapidly characterizing and optimizing ion optics are apparent when working with complex systems. To address these concerns, the Segmented Monte Carlo approach was developed and is discussed in detail in Chapter 3.

2.2.3 Electronics

2.2.3.1 Signal generators and power supplies. Electronics for generating the DC and AC signals used in this instrument come from many different signal generators and power supplies. For the Ga^+ FIB, most signals are generated from the vendor-supplied electronics with one notable exception. Beam deflection reference voltages were supplied from a PXIe-6739 (National Instruments) capable of high speed (up to 1 MS/s) voltage outputs to 64 channels. Each channel is capable of ±10 V outputs but only at 10 mA current, thus the capacitance of the capable and low-input resistance of the deflection optics limited scan-line speeds to about 2000 lines/second.

For the ion extraction/accumulation optics and the mass analyzer, DC biases were supplied from a custom MIPS (GAA Custom Engineering, LLC) solution capable of supplying 8 DC voltages at ±50 V and 8 more DC voltages at ±250 V with 5 mA output current per channel. While limited in their output current, the MIPS solution provided high-density, high-voltage power supplies unavailable from any other vendor and enabled direct connection of the power supplies to the electrodes without concern. Filament current was

supplied from an Agilent 6554A laboratory power supply and filament-bias was supplied from the MIPS. Slew times were ~80 ms due to the limited current output of the MIPS and the high-capacitance output terminals of the 6554A power supply.

Excitation waveforms for the FT-ICR were generated using a PXIe-5451 (National Instruments) 2-channel arbitrary waveform generator. Waveforms were generated on a personal computer (PC) and uploaded to the PXIe-5451 over MXIe (a high-speed communication interface). When possible, discrete coaxial cables were used for signal transmission to reduce crosstalk and noise. RF waveforms for powering the four quadrupoles were generated from the MIPS.

2.2.3.2 Digitizers and readbacks. Secondary ion/electron signal measured by the CDEM and amplified by the CDEM preamplifier was digitized using a PXIe-5122 (8-channel 60 MS/s oscilloscope; National Instruments). A second channel on the PXIe-5122 was utilized to monitor the scanline waveform generated by the PXIe-6739, thus aligning the CDEM signal with the beam scanline so that an image could be reproduced. A high-speed PXIe-5105 digitizer (2-channel 100 MS/s digitizer; National Instruments) was utilized for recording the FT-ICR transient. Instrument pressures and other analog readbacks were digitized using a PXIe-6739 multifunction DAQ (National Instruments).

2.2.3.3 Timing and control. All functionality of the imaging mass spectrometer was controlled using DataStation One, which is discussed at length in Chapter 4.

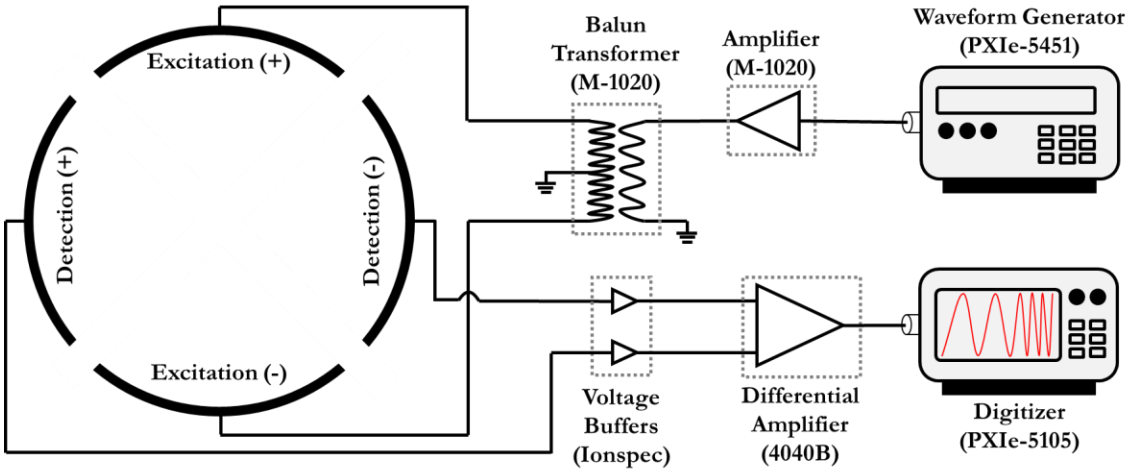

Scheme 2.3. Schematic representation of the FT-ICR excitation and detection signal paths. Waveform Generator and Digitizer graphics are for illustration purposes only.

2.2.3.4 Signal conditioning and amplification. Excitation is accomplished by loading a stored (calculated) waveform onto the PXIe-5451 waveform generator. This waveform is often a "chirp" (*i.e.*, frequency sweep) excitation waveform that transmits frequencies within a wide range by quickly scanning (although many other waveforms are possible). A properly-applied "chirp" excitation waveform causes the ions that are trapped within the ICR cell to be "excited" to a higher radius (i.e., closer to the excitation and detection curved plates depicted in Scheme 2.3). Additionally, chirp excitation induces coherency on ions with identical *m/z* that causes the ions to act as a single "packet". Once a waveform has been stored, the waveform generator can be triggered to emit said waveform at (± 1 $V_{b\text{-}p}$). This waveform is supplied to an amplifier (M-1020) which amplifies the waveform before it is sent into a balanced-unbalanced transformer (or balun) for the final voltage transformation (up to ± 300 $V_{b\text{-}p}$).. The balun also takes in the unbalanced waveform and "balances it" by producing an identical waveform that is 180° out of phase with the original waveform. These two, balanced (*i.e.*, inverted) waveforms

are then supplied to the excitation plates (inducing the aforementioned coherency and excitation of the trapped ions).

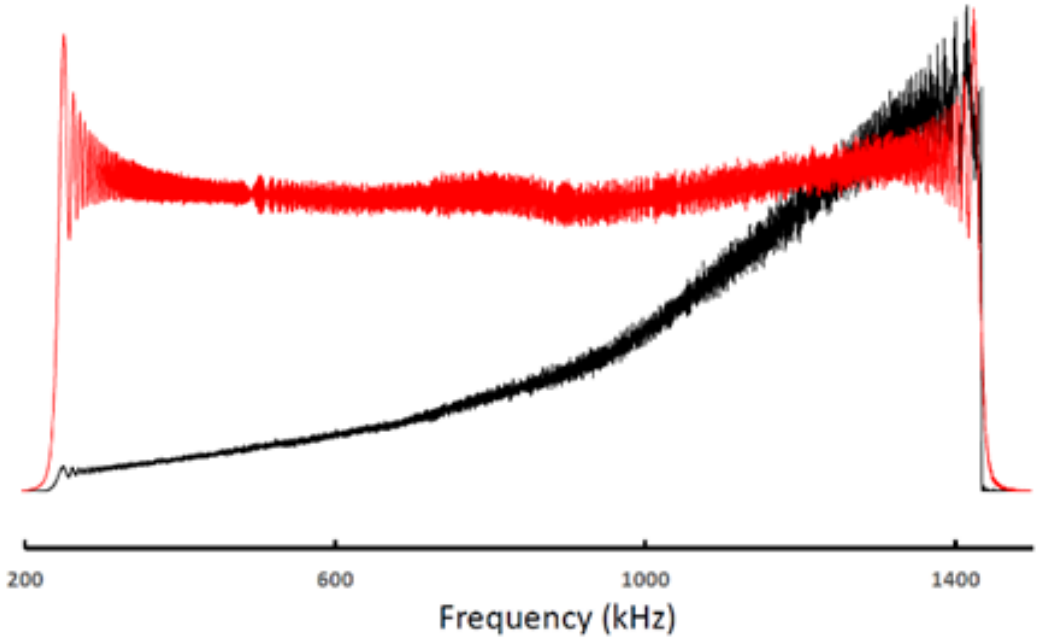

Figure 2.12. Power spectrum recorded on an individual detection plate for a chirp excitation (240-1460 kHz) generated and amplified by both an Ionspec FT-ICR (black) and the new PXIe/E&I excitation system (red). Excitation waveforms for the new system were found to be very flat in response, leading to more predictable ion excitation events.

Detection is accomplished by measuring the induced image current caused by ion packets in the ICR cell. As the ions pass by each detection plate (see Scheme 2.3, plates labeled Detection (+) and Detection (-)), the induced current is "buffered" (*i.e.*, the voltage level is maintained), thus allowing for the (relatively small currents) induced by the ions to be transmitted out of the (lengthy at 1 m) FT-ICR cell housing vacuum chamber. Both phases of the induced current are supplied to the Tegam 4040B differential amplifier (in a PXIe card slot configuration). The differential amplifier cancels out electromagnetic interference (like radio background noise) while amplifying the difference between these two signals (which should be inverse of one another for a given ion packet — as, when the ion packet is nearest the + plate, it will be farthest from the – plate and vice-versa). The

output of the differential amplifier is then digitized (using the PXIe-5105 card) and subsequently Fourier transformed for conversion into a mass spectrum.

2.2.4 Electromechanical Components

2.2.4.1 Sample positioning stage. When purchasing positioning systems, higher resolution (*i.e.*, step size) of the positioning system often comes with the tradeoff of reduced range (*i.e.*, total area moved). Piezoelectric positioning systems are no exception to this, as stacked-plate piezoactuators are capable of sub-nm resolution but over a limited range (only expanding by ~10 µm per cm of actuator length) and Stick-Slip piezoactuators are reliable only to about ~100 nm resolution but can travel over tens of mm. The positioning system used in the imaging mass spectrometer herein utilizes both stacked-plate and Stick-Slip piezoactuators to accurately positioning samples with single-nm precision in a large working volume.

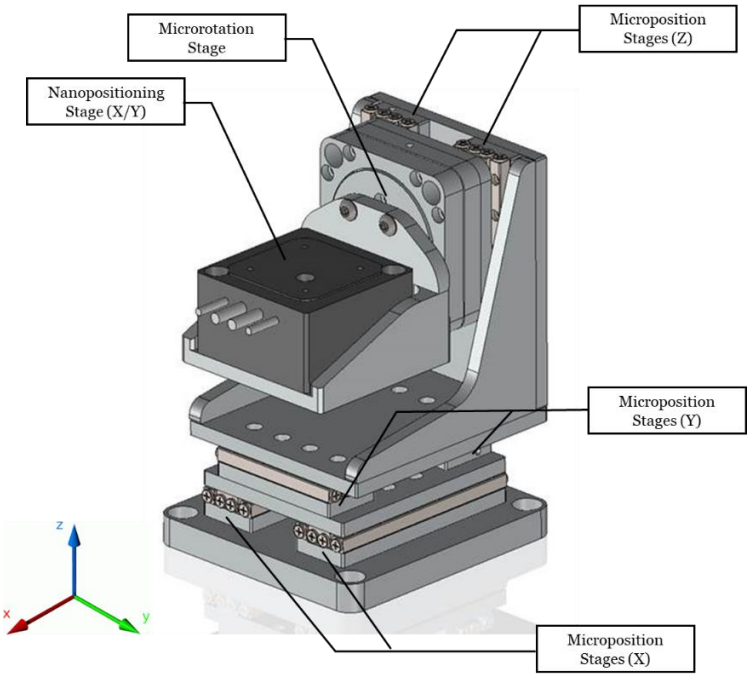

Figure 2.13. Computer render of the stacked-axis sample positioning stage with labels identifying the different piezoactuators.

The stacked-axis positioning system is show in Figure 2.13. Central to the positioning system is a 2-axis stacked-plate piezoactuator (PXY38; Piezosysteme Jena) onto which the sample is placed (Figure 2.13; Nanopositioning Stage (X/Y)). The PXY38 piezoactuator sits on a shelf attached to a rotation axis (SR-4513-3-HV; SmarAct) and is recessed such that the rotational axis is 2.0 mm above the top of the PXY38 (to account for sample height). The rotational axis is attached to a two Z-axis micropositioner (SLC-1740-S-HV; SmarAct) which are in turn attached to the Y-axis micropositioners by an angle bracket (SLC-1760-S-HV; SmarAct) and X-axis micropositioners by a bracket (SLC-1740-S-HV; SmarAct).

As assembled, the positioning system is capable of sample positioning within a 41 x 26 x 26 mm volume (X, Y, Z) thanks to the long travel range of the Stick-Slip micropositioners with a resolution of ~100 nm. Additionally, the sample angle (relative to the ion gun and extraction optics) is infinitely adjustable using the microrotation stage with a resolution of 5 µ°. High resolution sample positioning (less than 1 nm) is achieved with the nanopositioner and is always in reference to the rotation axis. Thusly, accurate and precise sample positioning can be made when the stage is rotated without modifying the working distance from the Ga^+ LMIS.

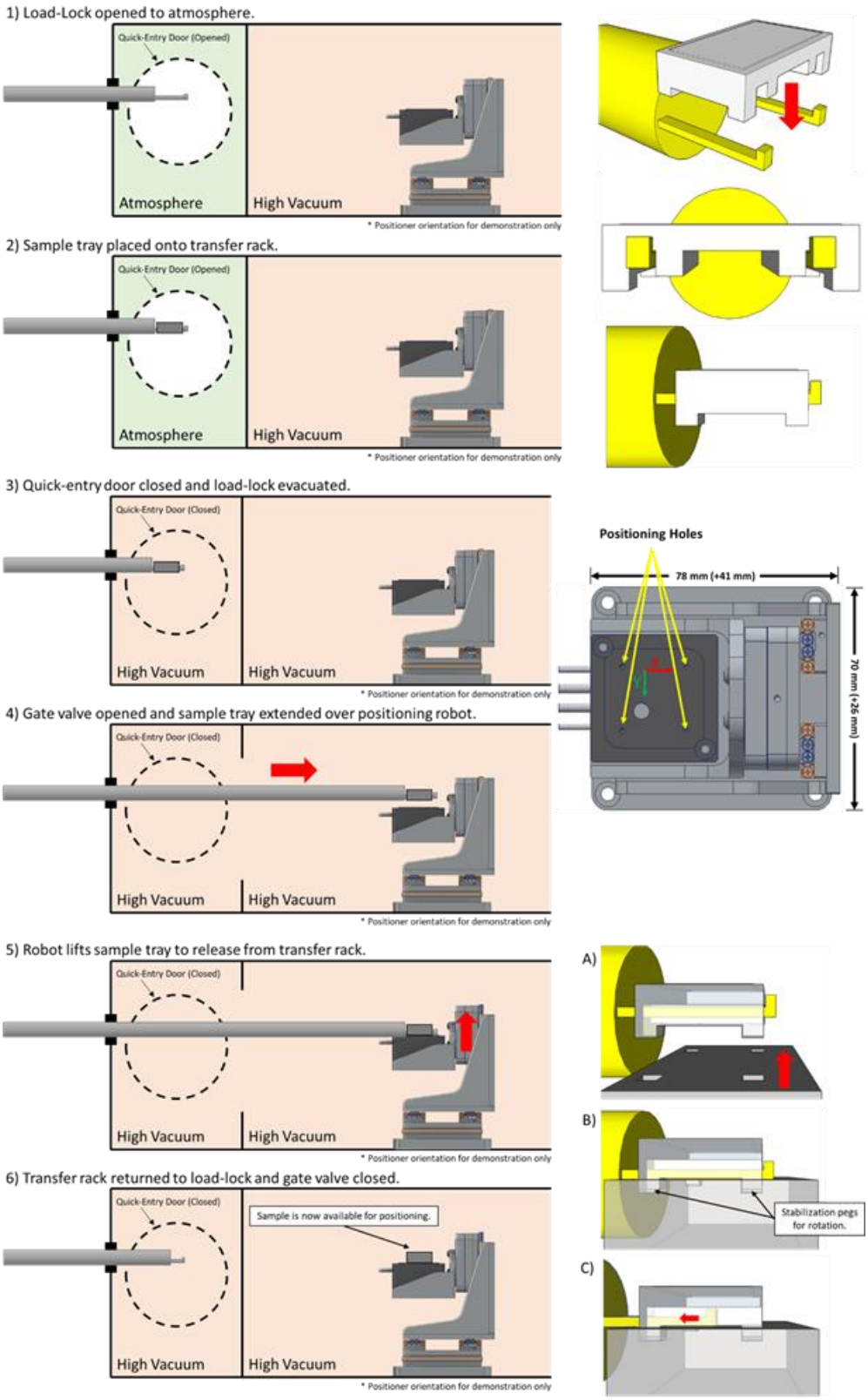

Figure 2.14. (Left) Diagrams showing the six steps of payload delivery from the load-lock chamber to sample positioner. (Right) Pictorial representation of the sample cart alignment geometries.

2.2.4.2 *Load lock sample transport mechanism.* To facilitate higher-throughput sample analysis, more reproducible sample positioning, and decreased need for venting of the instrument, a load-lock chamber was added that allowed sample transport into and out of the ion source chamber. Traditional, commercial FIB-SEM instruments generally have high-speed pump down capabilities. However, as a moderately-sized FIB FT-ICR MS image would likely take several hours to collect, rapid pump down was not as necessary as improved reproducibility and limited contamination of the ion column from frequent venting. To this end (and taking advantage of the 26 mm vertical travel distance of the micro positioning stage) a "forklift"-like mechanism of sample loading and unloading was devised (Figure 2.14, right-hand side).

The "forklift"-like mechanism of sample loading involves opening the load-lock chamber (Figure 2.14, step 1) and placing a sample "cart" onto two "fingers" that extended from the end of a robotic arm (Figure 2.14, top-right and Figure 2.14, step 2). The sample cart is secured by two upturned "fingertips" at the ends of the robotic arm "fingers" (Figure 2.14, top-right). The load-lock door is then closed, sealed, and the pressure evacuated *via* the turbomolecular pump (Figure 2.14, step 3). Once the load-lock chamber pressure has reached $1x10^{-7}$ Torr, the mechanical gate separating the load-lock and ion-source chambers is opened, allowing the mechanical arm to be extended into the ion source chamber (Figure 2.14, step 4). Once appropriately positioned, the positioning stage is raised to meet the sample cart. The sample cart has four alignment dowels that fit into the alignment holes of the nanopositioner and at sufficient height the sample cart is lifted above the robotic arm fingers (Figure 2.14, step 5). Finally, the robotic arm (free of the cart) is returned to the

load-lock chamber and the gate-valve shut (to enable higher vacuum and prevent any pressure fluctuations that might interrupt the imaging experiment; Figure 2.14, step 6).

2.2.4.3 High vacuum gas regulation. A new type of high-vacuum gas introduction system was developed for use with the imaging system. The previous standard technique involved two pulse valves connected to a tee junction on a leak valve.[162] Behind one pulse valve was a sample reservoir, behind the other was a roughing pump. For ion-molecule reactions, the pulse valve attached to the sample reservoir was actuated (thus supplying gas to the leak valve) for the length of the requisite reaction time. Afterwards, the sample reservoir pulse valve was de-energized, and at the same time, the vacuum pulse valve energized to quickly evacuate the remaining gas.

Three key limitations were observed with this system. (1) A noticeable delay occurred between opening of the vacuum pulse valve and return of normal ICR pressure. The delay resulted from the relatively high pressure (~5x10-2 torr) behind the sapphire leak valve feeding into the ICR chamber (~5x10-9 torr). (2) Finding the correct leak valve position for a desired vacuum pressure required trial and error. (3) Gas pressures behind the sample pulse valve would drift over long experiments.

To address the issues of the previous system, a new system was designed. In this system, a single pulse valve is connected directly to the vacuum chamber (thus removing the leak valve and one of the pulse valves) and was connected to a high-speed pulse valve driver (Iota One; Parker Hannifin). A closed loop PWM (200 Hz) control system was setup wherein the duty cycle of the PWM signal was adjusted dynamically in response to the pressure measured in the ICR cell. As a result, a specific pressure between $1x10^{-6}$ and $1x10^{-9}$ torr could be dialed in and maintained for upwards of hours without any of the negative

side effects of the previous system. This system was recently utilized in the FT-ICR analysis of carbohydrate HDX exchanges.[163]

2.3 Preliminary Results

2.3.1 Focused Ion Beam-Scanning Electron Microscope

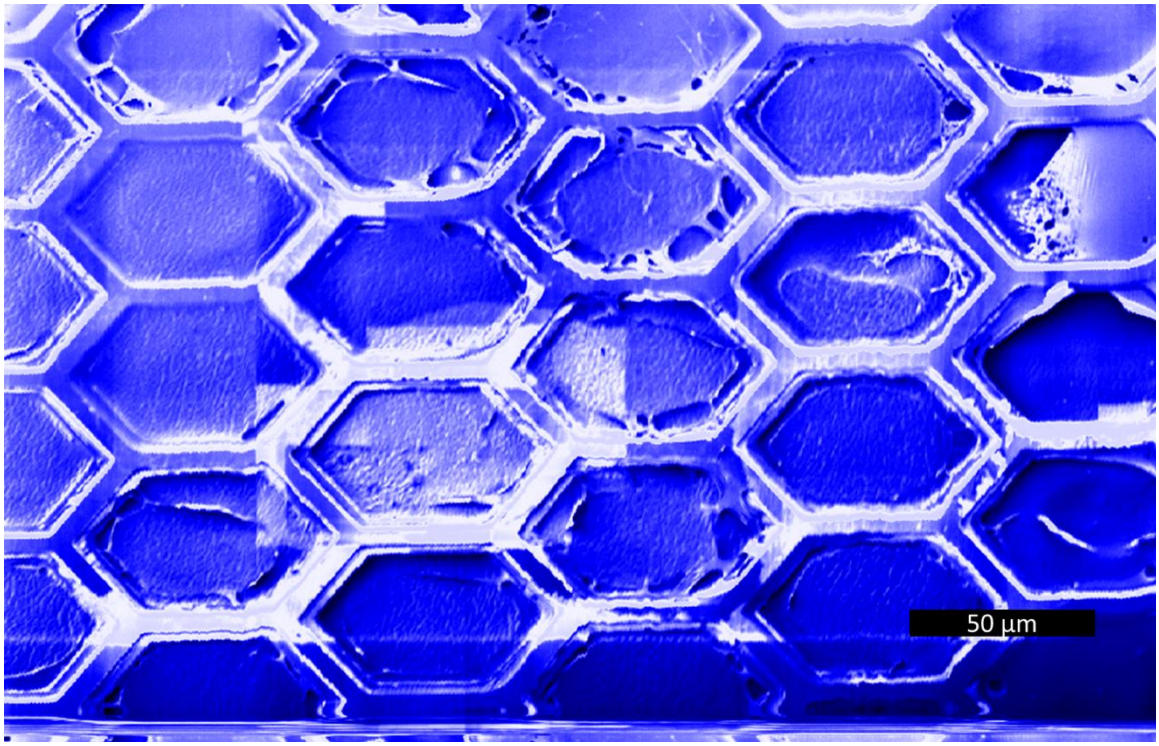

Figure 2.15. A FIB-SEM image of a standard TEM/SEM imaging grid with hexagonal cells. A scale bar (bottom-right) displays the length of 50 µm.

To validate the operation of the FIB-SEM, as well as assess potential spot size limitations for MSI, TEM/SEM imaging standard grids were imaged using our Ga^+ ion source and CDEM detector. Figure 2.15 displays one such grid as imaged by the FIB-SEM. Geometric areas of increased lightness or darkness in Figure 2.15 are the result of previous, zoomed-in imaging of the surface (surface charging or contamination can affect secondary ion yield). FIB-SEM imaging in this manner allows for pinpointing of regions of interest

(ROI) during the imaging process. These ROI can then be (much more slowly) imaged using MSI with confidence once that functionality has been completed. Without rapid imaging using FIB-SEM, the MSI results would be ambiguous at best and, at worst, imaging a region of no interest. Thus, the FIB-SEM operation is critical to the eventual goal of imaging mass spectrometry using this instrument.

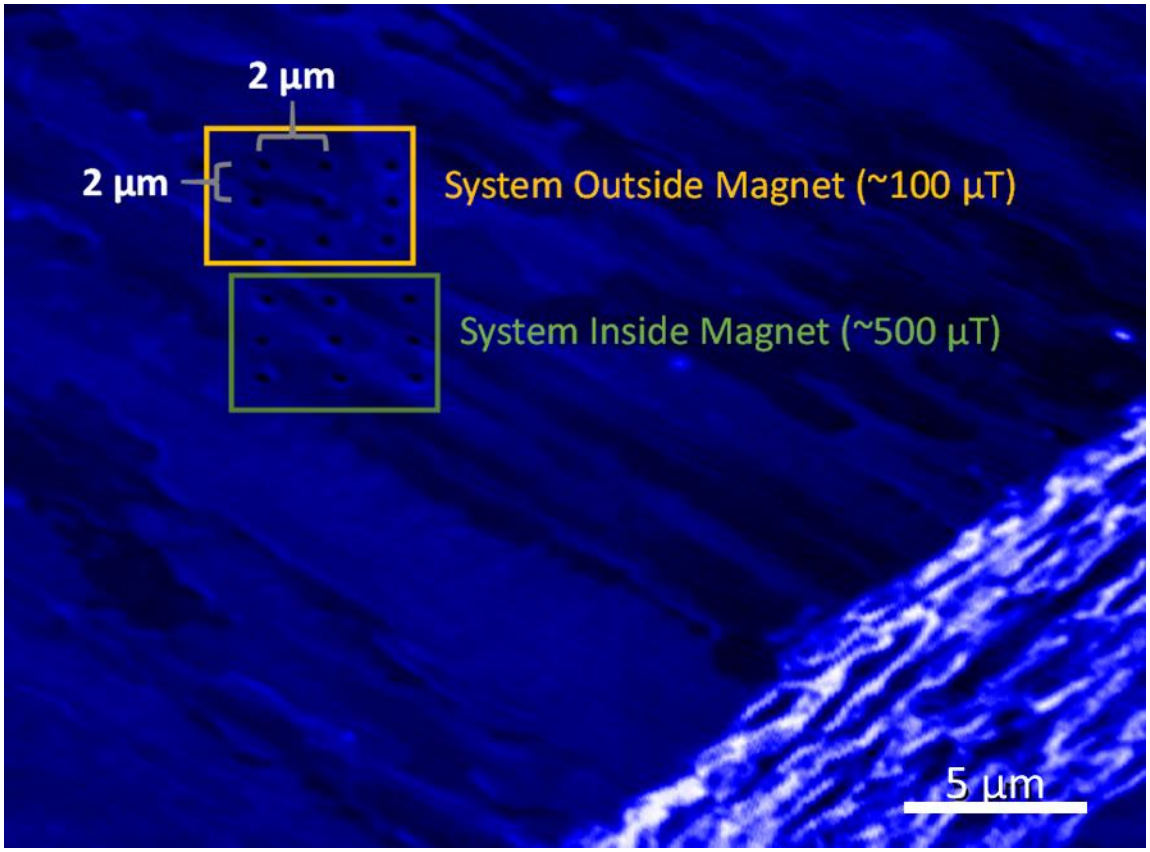

Figure 2.16. A FIB-SEM image of the same standard grid as presented in Figure 2.15, but zoomed-in further. "Holes" milled at intervals of 2 µm may be observed in the top-left corner. The bottom-right corner displays an image scale of 5 µm.

To determine the effects of the high magnetic field of the FT-ICR on Ga^+ ion column's stability (to ensure FIB functionality when using the FT-ICR), small "holes" were milled into the surface of an aluminum plate (See Figure 2.16 for examples of such holes) when the system was inside and outside of the magnet. Additionally, magnetic field

measurements were taken at the distance the Ga^+ column rests when the FT-ICR cart is outside of the superconducting magnet as well as at the distance the column rests when the cart is inside of the magnet (these readings were 100 and 500 µT, respectively). The results of these experiments demonstrated that the minimum, persistent "spot size" is ~750 nm with every "pixel" being ~200 nm. It also appears from the milling results that no significant difference beam stigmation is observed when the FT-ICR cart is inside the superconducting versus when it is not (a small shift is occurred though). Such results indicate that the current instrument may be suitable for MSI of large, eukaryotic cells but would be of little use for imaging of many important, smaller cellular organelles (e.g., vacuoles, mitochondria, etc.). After testing performed using vibration measurement devices, it was found that the multiple turbomolecular pumps are the principal cause of resolution-limiting vibrations. To that end we have purchased (but not yet installed) vibration-dampeners for said turbomolecular pumps.

2.3.2 Post-Ablation Capture

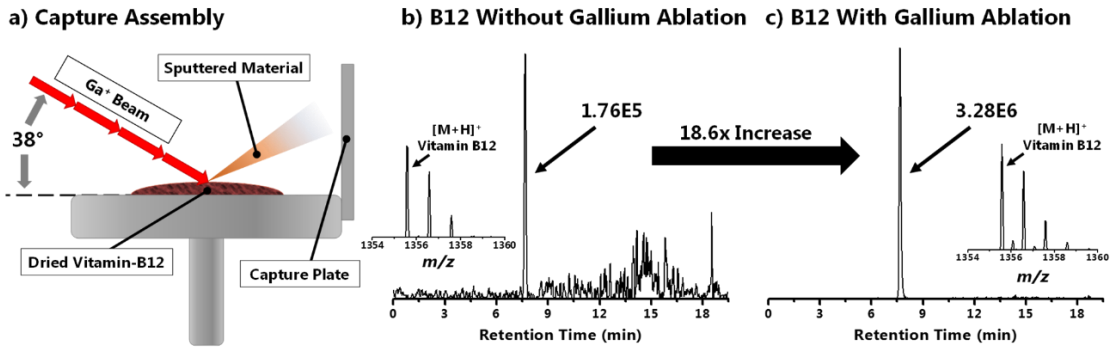

Figure 2.17. The scheme on the left shows an ion beam directed at a sample of vitamin-b12 at an angle of 38° and the ablated (sputtered) material being captured by a capture plate. The data collected in (b) are from a MS analysis of the capture plate after no Ga^+ ablation. The data collected in (c) are from MS analysis of the capture plate after Ga^+ ablation.

In order to probe the feasibility of ionizing intact, neutral molecules after Ga^+ ablation, a capture-plate device (Figure 2.17a) was constructed with dried vitamin b-12 as a test-analyte and subjected to Ga^+ ablation. After two capture plates (one with dried vitamin b-12 exposed only to pump-down and venting of the vacuum system and one that had been exposed to pump-down and venting of a vacuum system in conjunction with Ga+ ablation) had been obtained, each were swabbed with nanopore water and then injected into a ThermoFisher (Waltham, MA) Accella LC-Orbitrap LTQ-Discovery instrument with a reverse gradient beginning with water (with 0.1% formic acid) and ending with aceotnitrile. The chromatograms in Figure 2.17b and Figure 2.17c were generated using the selected ion chromatogram (SIC) from 1355 to 1360 *m/z* (the mass range of vitamin-b12).

Although vitamin-b12 was observed in both Figure 2.17b and Figure 2.17c, the relative abundance of the vitamin-b12 signal in Figure 2.17c is 18.6x higher than that of the signal in Figure 2.17b. These results indicate that, although some transfer of vitamin-b12 occurs from simple pumping down and venting of the ion source chamber, it is likely that the application of a focused Ga^+ ion beam can desorb intact neutral molecules (of at least an m/z of 1,355 *m/z*).

CHAPTER THREE

A Segmented Monte Carlo Approach for Unsupervised Optimization of Ion Optics in Mass Spectrometers

This chapter is prepared for publication in *Journal of the American Society for Mass Spectrometry* as: Brantley, M. R., Villacob, R., Solouki, T., A Segmented Monte Carlo Approach for Unsupervised Optimization of Ion Optics in Mass Spectrometers.

3.1 Abstract

Mass spectrometry (MS) is a rapidly growing field that is finding new applications across many domains of science. Many aspects of the mass spectrometer have been improved over time which required a deep understanding of ion motion to accomplish. Analytical solutions to ion motion problems have served to drive MS innovation in the past; however, numerical analysis of ion optics has rapidly become popular as computational resources have become increasingly abundant. Further, stochastic numerical approaches have proven a powerful tool for mass spectrometer analysis but are typically too computationally expensive to perform for complex systems.

In this manuscript, we introduce the Segmented Monte Carlo (SMC) technique for stochastic numerical optimization of ion optics used in mass spectrometers within the SIMION software package. Compared to other stochastic optimization techniques, SMC is simpler to implement, is more easily modified for unique applications, and produces solutions significantly faster than using Monte Carlo optimization alone (in some cases 100s-1000s fold faster). To demonstrate the use of SMC, we analyze three unique sets of ion optics and provide numerical results for discussion as well as compare with analytical solutions (when available). For all analyzed ion optics systems, SMC was capable of

providing rapid numerical results that facilitated the study of ion transmissions and elucidated useful information about individual ion optics components.

3.2 Introduction

Mass spectrometry (MS) has found ubiquitous application in fields such as food analysis,[164] elemental analysis,[165-166] environmental contaminate monitoring,[4-5] proteomics,[167] pharmaceuticals,[168] and more.[1] MS has also entered relatively new markets such as clinical diagnostics,[169] advanced imaging,[74-75] and portable hand-held analysis.[170] The growing prevalence of MS has come with an accelerating demand for increased mass resolution,[171] duty cycle,[74, 172] reproducibility,[173] portability,[170, 174] and sensitivity.[175-177] It goes without saying that the field of mass spectrometry has been, and continues to be, one of the most rapidly advancing fields of chemical instrumentation of current times.

The rapid improvement of mass spectrometer technologies has not happened by accident, it has instead been the result of concerted efforts by teams of engineers and scientist across the globe. In some cases, the improvements of mass spectrometers can be attributed to improvements in electronics,[178-179] analysis software,[180-182] and even vacuum chambers/pumps.[183] However, the most disruptive technological improvements of late have come in the form of new ionization sources,[27, 49, 184-185] mass analyzers,[186-187] ion optics,[188-189] and the advent of new ion mobility devices.[190-191] In each of these areas of improvement, an understanding of ion motions is critical.

Early on, analytical solutions to underlying physical motions drove instrument development, such as solutions to the Mathieu Equations driving the development of the quadrupole mass analyzer.[89] However, the continued growth of computational resources has facilitated the use of numerical approaches that, while computationally very expensive,

are simpler to implement and can facilitate unique geometries. Commercially available software, such as SIMION, COMSOL, Lorentz, QuickField FEA, *etc*., are available to facilitate these numerical calculations. Overwhelmingly, SIMION[192] has been the software of choice for the field of mass spectrometry with its application found in areas such as the development of mass analyzers,[92, 193-194] ion mobility devices,[195-197] ion guides/funnels,[189, 198-199] ion traps,[200-201] and others.[202-203]

Using these software-facilitate numerical approaches, entire arbitrary ion optics systems can be evaluated and optimized. Traditional ion optics optimizations are performed using deterministic optimization methods[204]; however, these approaches are limited in their ability to find a global optimized solution. Stochastic methods, such as Monte Carlo approaches[205-207] and genetic algorithms (GAs),[208-209] overcome many of the limitations inherent to deterministic approaches but require significantly more computational resources.[195] In this report, we introduce the Segmented Monte Carlo (SMC) approach for use with SIMION. SMC is a hybrid Monte Carlo implementation that includes several quality-of-life features and provides a framework for the rapid optimization and characterization of arbitrary ion optics. In many cases, SMC is over a hundred-fold faster to solution than traditional Monte Carlo approaches while still remaining a stochastic approach capable to finding global optimized solutions. To demonstrate the broad applicability of SMC, we examine three different ion optics systems with SMC and within each, highlight the various benefits and aspects of the SMC approach.

3.3 Experimental

3.3.1 Software

Segmented Monte Carlo (SMC) modules and components were written in LUA (V 5.3; PUC-Rio, Brazil) running within SIMION (v. 8.1.3; Scientific Information Systems, NJ, USA). All simulations referred to on this publication were performed on a Dell Precision 7810 Workstation (Windows 10 Pro; Xeon 10-core processor (2.4 GHz), 32 GB of ECC RAM) or on the Baylor University Kodiak cluster (CentOS 7; Cray CS400-AC, Xeon dual 18-core, 256 GB of ECC RAM per node). Data processing & plotting was performed utilizing MATLAB (v R2018a; The MathWorks, Inc., MA, USA) and Excel (v. 2016; Microsoft Corporation, WA, USA).

3.3.2 SIMION Workbench Generation

SIMION workbench files utilized herein were generated using the following steps. First, the SMC libraries were copied to the hard drive of the computer, only a single copy of these files in necessary. Next, a folder inside the SMC libraries containing all the necessary SMC workbench files ("SMC Clean Workspace") was copied and renamed to denote the particular workspace being generated. The contained files were then modified to perform the desired ion optics optimization by following the SMC documentation included with SMC. GEM file generation, PA refinement, and SIMION .IOB construction were performed automatically by running the included "SMC Setup.lua" file from within the SIMION graphical user interface (GUI).

3.3.3 Simulation Components

SMC components are LUA classes that contain the functionality for a specific ion optic component, such as a circular lens or a quadrupole mass analyzer. SMC components function by having a prescribed set of member functions that can called by the SMC workbench code. For example, GEM file generation for a particular component is contained within the "component.write" member function and utilizes information defined in the component declaration for customization. Various other member variables (such as adjustable electrodes) and functions contribute to the SMC functionality and are fully described in the SMC documentation included with SMC. In addition to the provided SMC component, new classes can be user created to represent practically any ion optics component of interest and be configured to work seamlessly within SMC.

3.3.4 Simulation Volumes

SMC volumes are also a LUA class serving the role of defining discrete simulation volumes within the SIMION workbench. For cases described in this manuscript where multiple segments are utilized, segments were defined manually based on the understanding of electric field overlaps and verified using potential energy plots.

3.3.5 Segmented Monte Carlo (SMC)

Notable SMC variables were specified in the "SMC Workbench.lua" file (matching the name of the SIMION IOB file "SMC Workbench.IOB") to determine the simulation bounds for *m/z* (SMC_Parameters.mz_start and SMC_Parameters.mz_end), the scanning mass interval (SMC_Parameters.mz_interval) and count (SMC_Parameters.mz_interval_ion_count), the number of failures between steps (SMC_Parameters.max_failures_for_step) and before full simulation restart

(SMC_Parameters.max_failures_for_reset), the maximum ion flight time (in µs) per step (SMC_Parameters.max_ion_flight_time), SIMION trajectory quality (SMC_Parameters.trajectory_quality), and a unique identifier for saving results (SMC_Parameters.identifier). Next a list of SMC component objects was created (SMC_Components) to detail the ion optic components used within this simulation and their various parameters. Ion checkpoints (which define the SMC optimization regions) and their cartesian bounds were then declared and added to a list (SMC_Checkpoints) as well as SIMION simulation volumes (SMC_Volumes). After specifying these values, SMC optimization was performed automatically by pressing the "Run" button in the SIMION GUI or by running the "Headless Win.bat" or "Headless Linux.bat" file, depending on the operating system used.

The core operation of SMC optimization consists of three primary steps, the last two of which are repeated indefinitely and are entirely automated. The first step includes defining the various SMC parameters, such as the .FLY2 parameters and the SMC settings (see previous paragraph). The second step involves the sequential optimization of SMC regions which are the areas between SMC checkpoints (see above). Starting with an ion generated using the .FLY2 parameters in SIMION, SMC parameters (defined in the various SMC component classes) are randomized and an individual ion is generated and its flight simulated until reaching the final SMC Checkpoint or (more likely) colliding with an electrode (*i.e.*, splatting)/exiting the simulation volumes. Each time an ion passes through a SMC checkpoint, it's velocity and position is recorded. Upon ion termination (*e.g.*, splatting or exiting simulation volume) the recorded position is recalled and all SMC components corresponding to electrodes *before* that SMC Checkpoint are locked (*i.e.*, their

Monte Carlo variables are static) and SMC components corresponding to electrodes *after* that SMC Checkpoint are randomized again. This process continues until either the ion reaches the final SMC Checkpoint or the number of ion terminations exceeds SMC_Parameters.max_failures_for_step (in which the recorded ion position/velocity is returned to previous SMC checkpoint) or SMC_Parameters.max_failures_for_reset, in which the process is restarted back at the initial ion generation step. When an ion enters the final SMC checkpoint the third step begins, all SMC components remained locked while a sequential series of ions (between SMC_Parameters.mz_start and SMC_Parameters.mz_end at intervals of SMC_Parameters.mz_interval; SMC_Parameters.mz_interval_ion_count number of ions per interval) are scanned and the total transmission per interval recorded in a comma separated value (CSV) file.

3.4 Results and Discussion

3.4.1 Segmented Monte Carlo

Segmented Monte Carlo (SMC) lowers the barrier of entry to Monte Carlo optimization and makes rapid characterization and optimization of an arbitrary ion optics system significantly easier and faster than previously possible. The underlying code for SMC is freely available, requires no proprietary libraries (other than SIMION and its included libraries), and can be executed by a conventional desktop PC. Furthermore, SMC can be implemented without the need for a database or even access to the internet. Each SMC instance runs entirely independently and records its output to a separate comma separated values (CSV) file. Parallel processing is achieved by simply running multiple SIMION instances on a single computer, multiple computers, or even a cluster and collating the CSV files afterwards. Depending on the size of the simulation volumes, the

limiting factor for the number of concurrent simulation instances is typically the available RAM (for large simulation volumes) or the number of physical CPU cores. Since data is output directly to CSV files in columnated form, it is easily human interpreted using software such as Microsoft Excel (although it should be noted not to lock the file from modification by opening it in Excel if it is being actively written to by a simulation instance).

The core functionality is contained within a set of core LUA scripts that are automatically loaded by the SMC workbench which contain all of the necessary code to facilitate generating GEM and PA files, refining PA, positioning electrodes within the SIMION workbench, running the SMC optimization, and writing outputs. All component-specific functionality is containing within the SMC component files, which provides an easy interface for defining custom ion optic geometries, electric/magnetic potential arrays (static or non-static), and variables for Monte Carlo optimization. SMC components typically include variables in their constructor to adjust various aspects, such as the position, rotation, rod length, rod radius, and inscribed radius of a quadrupole mass analyzer. Additionally, the SMC component constructor will allow for defining the bounds of the Monte Carlo variables, such as the rf amplitude, rf frequency, dc bias, and dc resolving potential of a quadrupole mass analyzer. Thus, only a single SMC component class is necessary to describe the different shape/sizes of a given ion optic component.

Scheme 3.1 outlines the workflow of SMC across the three previously discussed categories of functionality, preparation of SMC and the Ion Workbench (Scheme 3.1; I. Preparation), discovery of valid parameter solutions suitable for ion transmission (Scheme 3.1; II. Solution Discovery), and validation of the parameter solutions across a range of *m/z*

values (Scheme 3.1; III. Solution Validation). User input is only necessary for steps listed in Phase I (Preparation; steps A to C) while Phase II (Solution Discovery; steps D to S) and Phase III (Solution Validation; steps T to Z) are performed entirely automatically. Additionally, the Preparation Phase is only necessary the first time a workbench is prepared or when modifications have been made to the ion optic geometries.

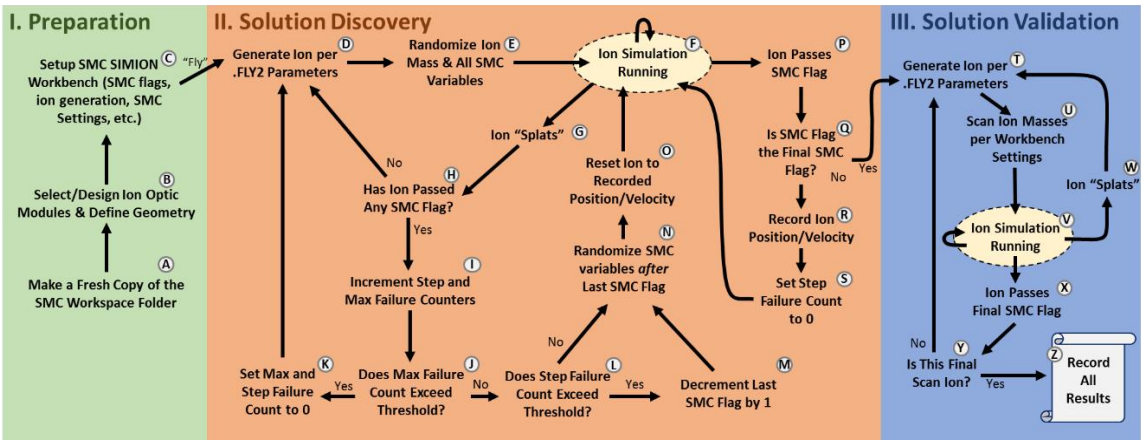

Scheme 3.1. Flowchart showing individual steps within the three phases of the SMC process, preparation (I; green), solution discovery (II; orange), and solution validation (III; blue). Individual steps are labeled to facilitate discussion in text. Yellow highlighted regions denote the simulation loop of the SIMION software.

The Solution Discovery phase (Scheme 3.1; II. Solution Discovery) is pictorially represented in Scheme 3.2. Initially, ions are generated per the FLY2 file parameters and the mass range set in the SMC Settings file. This process continues until an ion reaches an SMC checkpoint (Scheme 3.2A) at which the ion location and velocity are then recorded, and the ion continues until its eventual splat. After splatting, the ion is reset to the previously recorded position/velocity and all SMC components (removed from the scheme for simplicity) *after* the checkpoint are randomized while SMC components *before* the checkpoint are held constant. This process repeats (Scheme 3.2B) until the ion reaches the next SMC checkpoint and the new position/velocity is recorded. The maximum number of

attempts between steps is determined in the SMC Settings file (SMC_Parameters.max_failures_for_step) and, when exceeded, will result in the reset of the ion position to the previous SMC checkpoint (Scheme 3.2C). An additional settings value (SMC_Parameters.max_failures_for_reset), when exceeded, will result in complete reset of ion recordings to the initial FLY2 parameters (not demonstrated in Scheme 3.2). Should an ion eventually reach the final checkpoint (Scheme 3.2D), the Solution Validation phase will be initiated, and the results recorded.

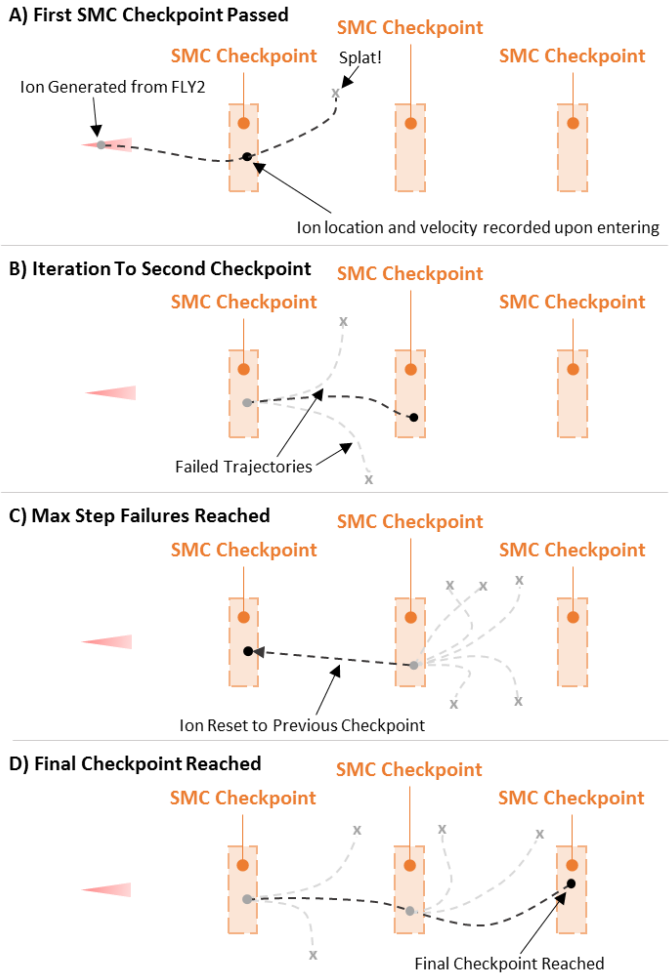

Scheme 3.2. Pictorial representation of the solution discovery process within SMC highlighting various steps. A) Recording of ion location and velocity upon first checkpoint entry. B) Iteration between checkpoints. C) Resetting of ion recordings after exceeding failures per step. D) Successful solution discovery and triggering of solution validation phase.

3.4.2 Resolving Quadrupole and Digital Quadrupole

A simple example of the benefits of SMC was demonstrated with a quadrupole mass filter (shown in Figure 3.1a). In this example, only a single SMC checkpoint was utilized and thus only steps D, E, F, G, H, P, and Q of Phase II (Scheme 3.1) are necessary. Specific geometry information can be seen in Appendix Table B.1**,** SMC settings can be seen in Appendix Table B.2.

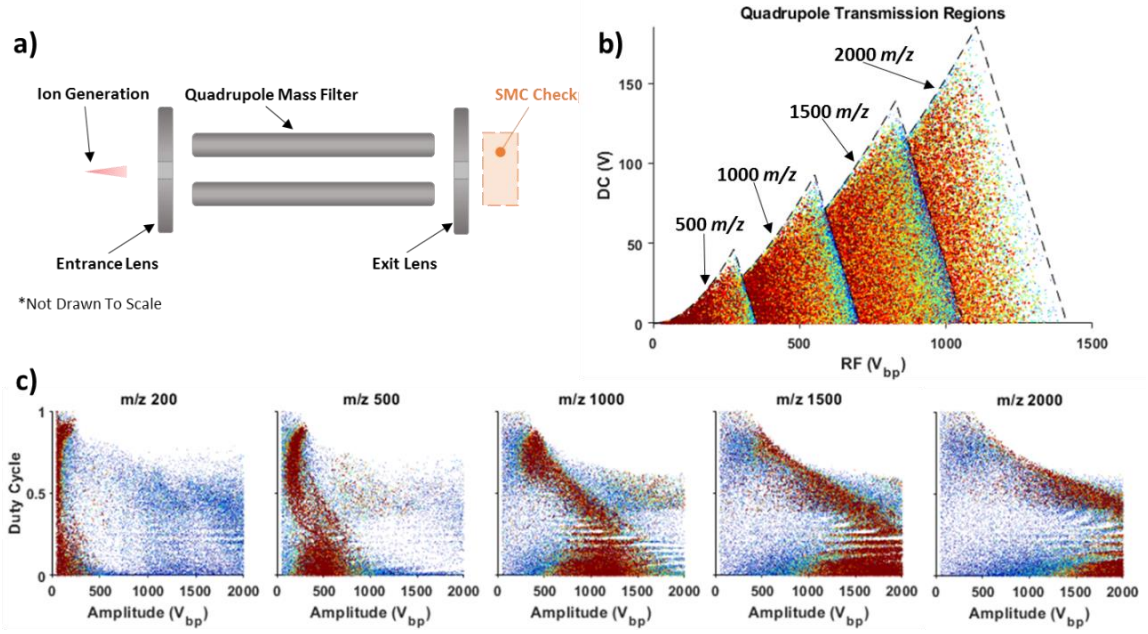

Figure 3.1. a) Schematic representation of the simulation components and their arrangement for both the conventional "resolving quadrupole" and "digital quadrupole" experiments. b) Overlaid scatter plots of all SMC simulations solutions for *m/z* values 500, 1000, 1500, and 2000 (where both size and color vary with transmission efficiency) at different RF amplitude and resolving DC potentials. Theoretical first transmission region boundaries are shown in dashed lines. c) Scatter plots of all SMC simulations solutions for *m/z* values 200, 500, 1000, 1500, and 2000 (where both size and color vary with transmission efficiency) at different square wave amplitude and duty cycles. Striations visible on all plots between 0.0 and 0.5 duty cycle are present in the data set and are not visual artifacts resulting from imaging scaling (aka, screen-door effect).

SMC was utilized to numerically solve quadrupole stability diagrams at 40 different masses (50-2000 *m/z* at linear increments of 50 *m/z*) and the results were compared against analytical solutions to the Mathieu equation.[89] For these experiments, 10 separate SMC

instances (Monte Carlo bounds can be seen in Appendix Table B.3) ran in parallel for a total of 710.9 worker hours and produced 64739 solution sets (averaging 91 solutions/hour per worker). Given the relative simplicity of this system, it was not surprisingly that approximately 1 in 12 trials produced a valid solution.

Figure 3.1b shows overlaid numerical (scatter points, color and size scaled with transmission efficiency) and analytical (first transmission region - dashed lines) quadrupole transmission regions for *m/z* values 500, 1000, 1500, and 2000. For all masses, numerical results were almost exclusively within the bounds of the analytical solutions. It should be noted that *all* data points with transmission efficiency greater than 0% (for a given mass) were utilized in this figure. The decrease in point density observed at increased RF amplitudes for *m/z* 2000 is attributed to a decreased number of solutions at *m/z* 2000 (see Appendix Figure B.1) being spread across a larger transmission region. Additionally, the numerical results generated using SMC revealed a sharper transmission line on the *lower* RF amplitude side relative to the *higher* RF amplitude side.

In another test, the standard resolving quad class was substituted for a "digital quadrupole" class which replaced the sinusoidal signal with a pulse width modulated (PWM) RF. The digital quadrupole geometries were identical to those of the resolving quad but was technically a different SMC component due to the difference in applied waveforms (Appendix Table B.4). Only two lines were modified in the SMC Settings file to facilitate this change (*i.e.*, changing the quadrupole SMC component and assigning a new SMC_Parameters.identifier). In a similar manner to the resolving quadrupole experiments, numerical solutions to the transmission region of the digital quad were generated and select masses are shown in Figure 3.1c. With increasing mass, it was observed that an oblong

shaped region of high transmission shifted towards higher RF amplitudes and valid solutions were observable at duty cycles between 0 (where the quadrupole was essentially off) to 0.95. Striated regions of no transmission were observed across all tested masses between duty cycles of ~0.1 and ~0.4 which could be falsely interpreted as visual artifacts (such as the "screen door" effect) but are actually present in the data set. The exact explanation for these regions of no transmission is currently unknown and, while interesting, remains beyond the scope of discussion in this manuscript.

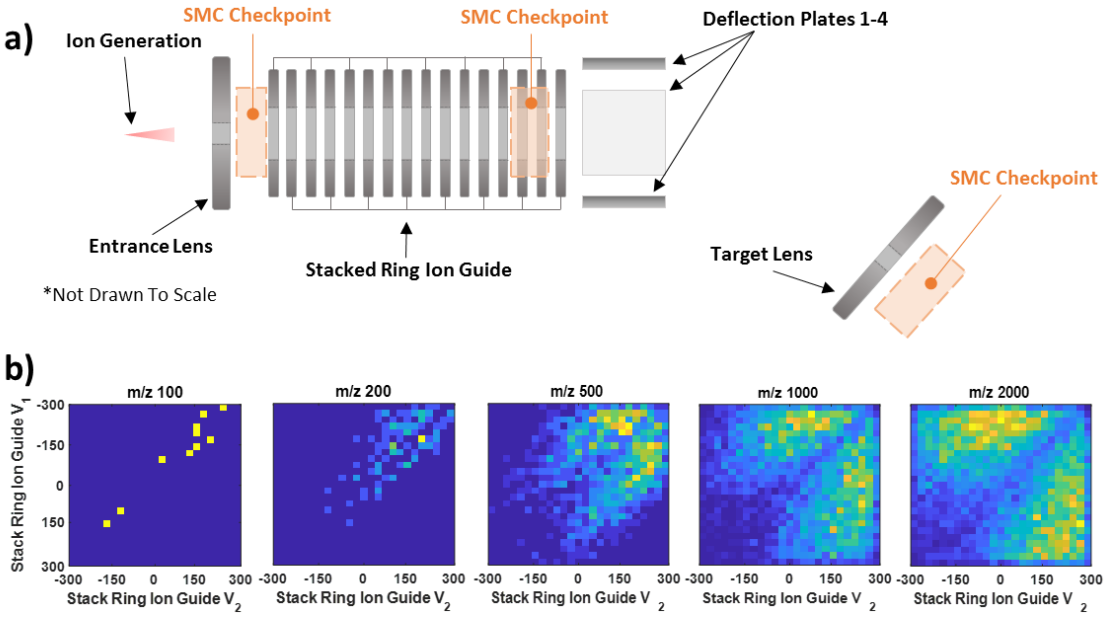

Figure 3.2 a) Schematic representation of the simulation components and their arrangement for the "arbitrary geometry" experiments. SMC checkpoint regions are represented in orange. Precise positioning and geometries (as well as ion generation and additional simulation parameters) are available in supplemental information. b) Images representing density of SMC solutions (equivalent of a 2d histogram) for *m/z* values 100, 200, 500, 1000, and 2000 as a function of alternating stacked ring ion guide voltages.

3.4.3 Arbitrary Geometry with Stacked Ring Ion Guide

A more complex geometry is shown in Figure 3.2a which consists of an entrance lens, a stacked ring electrostatic ion guide,[210] a set of deflection lenses, and a target lens positioned off-axis to the ion flightpath. Unlike the previous example, this geometry utilizes multiple SMC checkpoints (denoted in orange) which are necessary for the calculation time improvements of SMC. In this particular example, a ~3-fold reduction in the number of trials per solution (TPS) was observed when SMC was utilized (349±4 TPS for SMC and 1026±28 TPS for non-SMC; 95% confidence interval, n=4). Ion optic geometrics can be seen in Table B.5, SMC Settings in Table B.6, and Monte Carlo bounds in Table B.7.

All potential arrays used in the arbitrary geometry example are static, including the stacked ring ion guide which relies on ion motion through alternating polarity rings to emulate a time-varying signal.[210] Since each solution parameter is recorded, individual components can be analyzed even when they are part of a larger system. In Figure 3.2b, relative densities of solutions found for different masses (as a function of stacked ring ion guide voltages) are shown. Equal values for V_1 a V_2 showed few solutions across the different masses; however, as mass increased so did the spread of solutions across larger differences in V_1 and V_2. A greater difference in V_1 and V_2 would correspond to an increased amplitude in the pseudo-sinusoidal potential felt by the ions as they moved through the stacked ring ion guide, thus it is not surprising to see higher masses be tolerant to larger differences in V_1 and V_2.

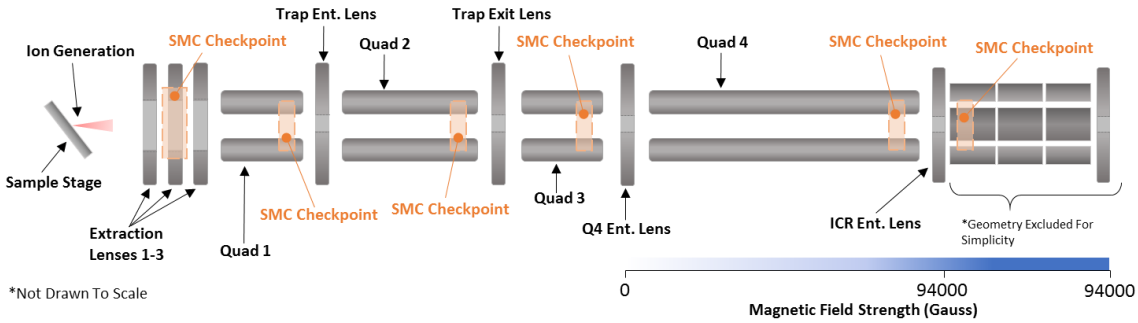

Figure 3.3. Schematic representation of the simulation components and their arrangement for the RFI FT-ICR MS "imaging system" experiments. Only components relevant to the ion flight path were included. SMC checkpoints regions are represented in orange. Simulation volumes were separated for memory optimization but are not demarcated here. An increasing magnetic field gradient is represented on the bottom right (drawing is only pictorial). Precise positioning, geometries (as well as ion generation, segmentation, and additional simulation parameters) are available in supplemental information.

3.4.4 Imaging System with Long Flight Path

SMC was utilized in the optimization of a novel imaging mass FT-ICR mass spectrometer currently being evaluated. In short, the instrument operates by ablation of solid material using a Ga^+ focused ion beam (FIB) and subsequent ionization using a gas phase ionization technique such as Radio Frequency Ionization (RFI),[49] Electron Ionization (EI),[36] or Field Ionization (FI),[60] For purposes of SMC optimization, only the ions generated from post-ionization event were modeled in SIMION as the proposed mechanism of ion generation is still currently under investigation. A representative schematic of this instrument is shown in Figure 3.3.

The imaging system being examined here contains numerous components. Beginning at ion generation, a sample stage, a series of three extraction lenses, and a short quadrupole guide ions towards a quadrupole ion trap (Trap Ent. Lens, Quad 2, and Trap Exit Lens in Figure 3.3). In many cases, this trap would be used for external ion accumulation; however, in this example we do not utilize this feature primarily in effort to reduce overall simulation times (ion trapping times are easily 100x that of ion transmission

times). After leaving the trap, ions travel through another short quadrupole and then a long (119.4 cm) quadrupole to the ICR cell. The imaging system additionally has a superimposed sigmoidal magnetic field (fitted to experimental measurements; Appendix Figure B.2). For further simplicity, all electrodes after the ICR Ent. Lens were removed from the simulation. Ion optic geometrics can be seen in Appendix Table B.8, SMC Settings in Appendix Table B.9, and Monte Carlo bounds in Table B.10.

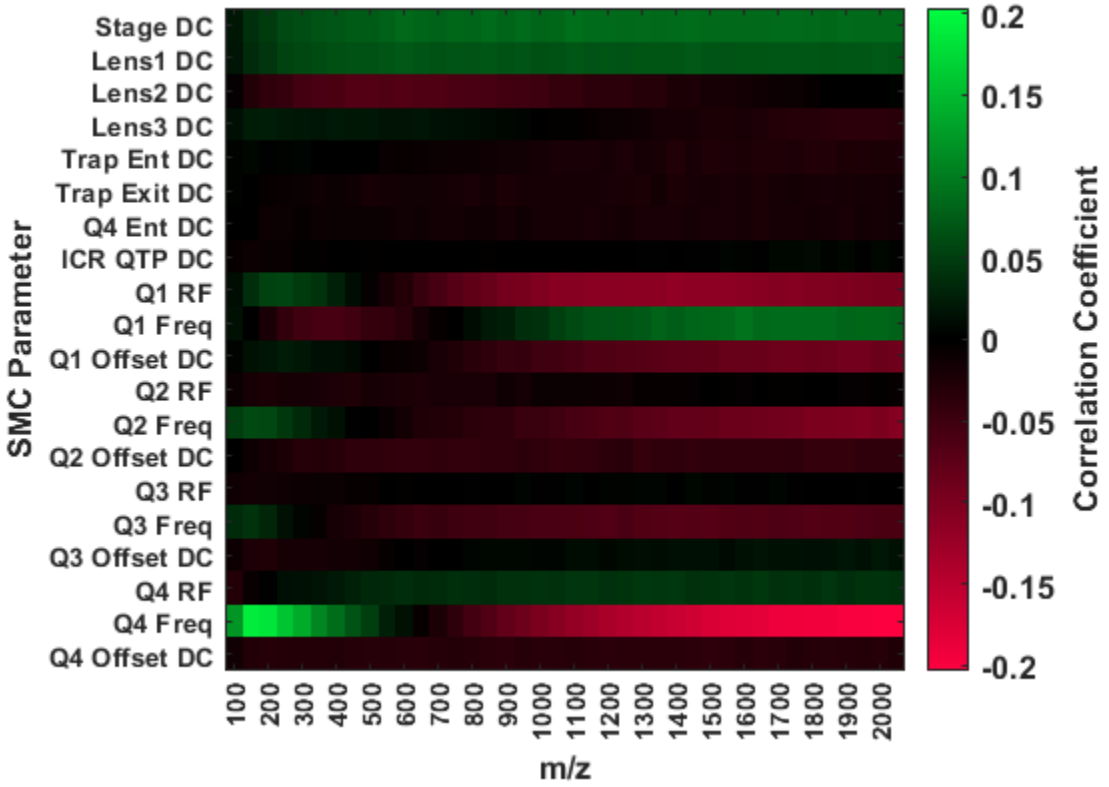

Figure 3.4. Correlation coefficients matrix (shown as colormap) for all tested *m/z* values against all SMC parameters. For any given SMC parameter, this plot highlights trends in correlation across the mass range.

Given the number of components making up the imaging system, simple manual analysis of each individual component became tedious. As such, correlation coefficients between each tested mass and each component parameter were calculated and are shown in Figure 3.4. Plots of correlation coefficients highlight parameters with the most

predictable influence on ion transmission (allowing targeted optimization) and guide manual optimization efforts in the future. One particularly interesting observation available in Figure 3.4 is the varying correlations between the frequency parameter of the different quadrupoles. For Q1, frequency shows a negative correlation between *m/z* 250 and 650 but a positive correlation between *m/z* 900 and 2000; however, Q2-Q4 show a somewhat inverse relationship with lower masses having a positive correlation and higher masses having a negative correlation. These results demonstrate the benefit of studying a system as a whole rather than as individual parts (where such differences in relationships may not be observable).

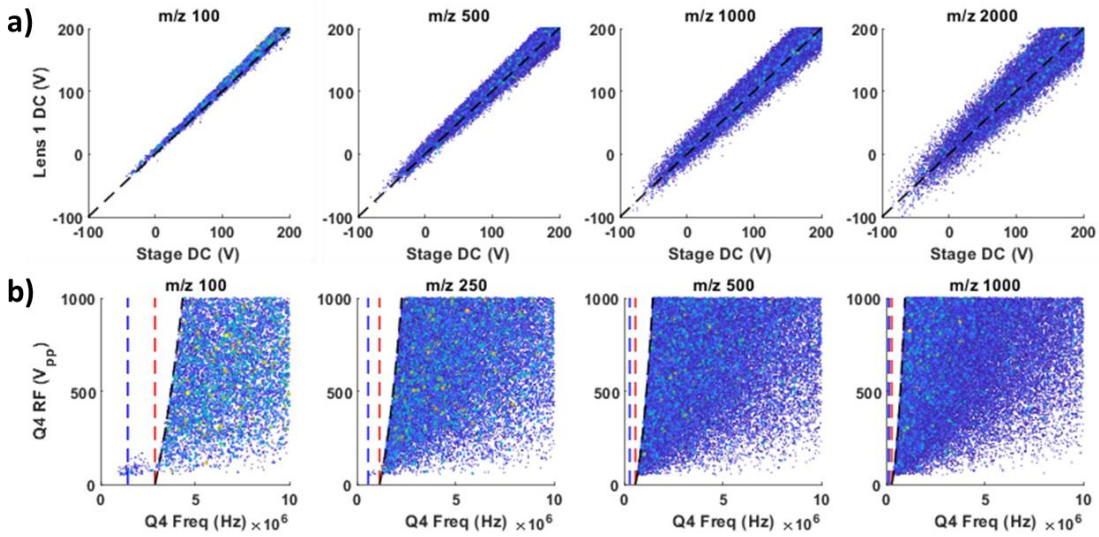

Figure 3.5. (a) Scatter plots of all SMC simulations solutions for m/z values 100, 500, 1000, and 2000 (where both size and color vary with transmission efficiency) at various Stage and Lens 1 DC potentials. The equal potential line (where Stage DC and Lens 1 DC are equal) is show as a overlaid dashed line. (b) Scatters plots of all SMC simulation solutions for m/z 100, 250, 500, and 1000 (where both size and color vary with transmission efficiency) at various Q4 frequencies and amplitudes. The cyclotron frequency (at 9.4 T) is show as a blue dashed line, 2x that frequency shown as an orange dashed line (second harmonic), and the analytical solution for mass cutoff is shown as a black dashed line.

Stage and Lens 1 DC voltages show positive correlations in Figure 3.4 which prompted further evaluation of this relationship. Figure 3.5a shows scatter plots of transmission values at all solved Stage DC and Lens 1 DC values for *m/z* 100, 500, 1000, and 2000. At *m/z* 100, the majority of solutions utilize a Lens 1 DC voltage that is higher than the Stage DC voltage. It may be initially confusing as to why valid solutions are more dominant when the ions have to overcome a repelling voltage from Lens 1 (as all ions shown are positive ions). This phenomenon is easily explainable as when Lens 1 DC exceeds the Stage DC voltage a funnel-like potential well is present around Lens 1 and directs ion through Lens 1; however, when Stage DC exceeds Lens 1 DC the potential well inverts into an unstable saddle that direct ions into the Lens 1 electrode. As mass increases, a greater spread in relative voltages is observed in addition to a more even representation on both sides of the equal potential line. This observation can be explained by how ions are generated for this simulation as ion velocities were independent of ion mass and thus ions with higher masses have higher kinetic energy and can overcome larger potential gradients *via* their initial velocities.

Strong correlations can be observed between Q4 frequency and mass (Figure 3.4), with a positive correlation being observed for *m/z* 50-500 and negative correlations being observed for *m/z* 750-2000. This relationship is demonstrated as scatter plots in Figure 3.5b for *m/z* 100, 250, 500, and 1000. Analytical solutions of quadrupolar transmission regions in the presence of a magnetic field have been previously discussed [211-212] and solutions to these equations are shown as black dashed lines in Figure 3.5b. As expected, numerical results generated using SMC were in agreement with the analytical solutions *except* at lower masses where numerical solutions were observed at lower RF frequencies and

voltages than would be expected (for *m/z* 100 and 250 in Figure 3.5b). While outside the scope of this manuscript, further insight into how these low RF frequency and amplitude transmissions occurred would be of interest to FT-ICR applications.[211]

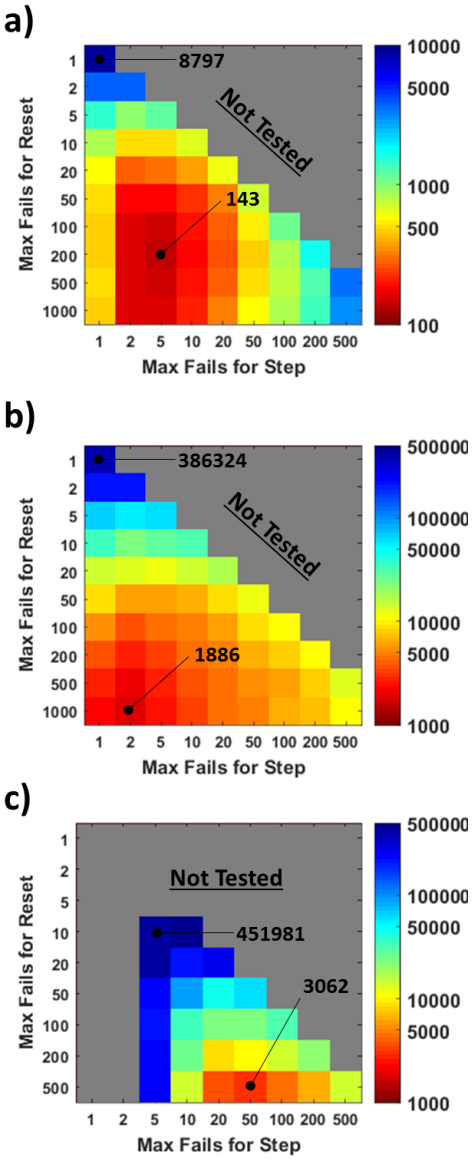

Figure 3.6. Average trials per solution (n=5) generated at various "max fails for reset" and "max fails for step" settings for a) no resolving DC, b) resolving DC of ±500 V on Q4, and c) resolving DC of ±100 V on Q1-Q4 after 24 hours of runtime. Gray regions were not tested as they correspond to "max fails for step" that exceed a given "max fails for reset" or did not produce a single solution after running for 24 hours.

Several combinations of values for SMC_Parameters.max_failures_for_step and SMC_Parameters.max_failures_for_reset were evaluated to find the lowest TPS possible for the imaging system. As shown in Figure 3.6, the optimal combination depends on a variety of factors, including the SMC variable domains. When compared to a non-SMC approach (where both SMC_Parameters.max_failures_for_step and SMC_Parameters.max_failures_for_reset were set to 1), a 62-fold efficiency increase was observed when the dc resolving variables are disabled (Figure 3.6a) which increased to 205-fold upon the addition of a ±500 V DC resolving variable on quad 4 (Figure 3.6b). Applying a ±100 V DC resolving component to all four quadrupoles (Figure 3.6c) increased the difficulty so much that we were unable to generate a single result (within 24 hours) for all 1 or 2 SMC_Parameters.max_failures_for_step but did find an optimal solution producing 3062 TPS. Should the optimization trends from Figure 3.6a and Figure 3.6b hold true for Figure 3.6c, it is reasonable to expect SMC's efficiency reached into the 1000s-fold improvement regime but would have required weeks of dedicated computation resources to validate.

Information about the relative difficulty of each SMC checkpoint can be obtained by calculating the fraction of trials originating at each checkpoint (information contained in the output generated by SMC). These fractions are calculated for four different simulation tests wherein the DC resolving component was removed (*i.e.*, set to ±0 V) from all but *one* quadrupole (*i.e.*, set to ±500 V) and displayed as stacked bar plots (Appendix Figure B.3). When comparing the fraction size of SMC checkpoints that correspond to a given quadrupole with the DC resolving component enabled, it can be seen that in each case the DC resolving component increased the relative difficulty of that checkpoint.

3.5 Conclusions

Segmented Monte Carlo (SMC) has been demonstrated as an efficient tool for characterizing and optimizing arbitrary ion optics systems. Analysis of three different ion optics systems using the SMC library running inside SIMION were performed and, in cases where multiple SMC checkpoints can be utilized, efficiency of stochastic solution searches were demonstrated to increase by up to 205-fold with certain highly-complex scenarios demonstrating theoretical efficiency improvements of several 1000-fold compared to Monte Carlo alone. For each ion optic solution, numerical results were discussed and, where applicable, compared against analytical solutions. Additionally, discussion into optimizing the SMC search parameters was provided.

3.6 Acknowledgements

The authors gratefully acknowledge funding provided by the National Science Foundation (IDBR-NSF 1455668). The authors thank Mike Hutcheson of Baylor University High Performance and Research Computing Services for assistance with running SIMION on the Baylor Kodiak Cluster. Additionally, the authors thank David Manura of Adaptas Solutions for the generous technical assistance with SIMION.

CHAPTER FOUR

Data Station One: An Open Source, Modular Control Platform for Custom Imaging Mass Spectrometers

This chapter is prepared for publication in *Journal of the American Society for Mass Spectrometry* as: Brantley, M. R., Anthony, I. G. M., Solouki, T., Data Station One: An Open Source, Modular Control Platform for Custom Imaging Mass Spectrometers

4.1 Abstract

In recent years, scientific instrument control software has increased in complexity to the point where it is now becoming unfeasible for custom instrument control platforms to be developed without significant investment. Other complex software domains, such as video games and internet websites, have remedied the problem of software complexity through the use of centralized software development kits (SDKs) and content engines. These engines and SDKs provide standardized tools, easy-to-use interfaces, and a myriad of other features in an "all-in-one" solution that increases software quality while dramatically reducing development times. Here we introduce DataStation One (DSO), a development platform and SDK for the implementation of complex scientific instrument control systems. DSO provides a "core" set of functionalities that serve to reduce the amount of work needed to begin instrument development. Further, DSO is easily extended by simple-to-write user scripts (DSO comes with many such scripts, built-in as well as template scripts for instrument developers to write their own). Additionally, we demonstrate the capabilities of DSO by developing and acquiring data from three scientific instruments: a Fourier-transform ion cyclotron resonance mass spectrometry (FT-ICR MS) instrument, a focused ion beam-scanning electron microscopy (FIB-SEM) instrument, and

a vacuum measurement instrument. All three of the instruments can be combined to enable a mass spectrometry imaging (MSI) instrument, which is currently under development.

4.2 Introduction

Scientific instruments are the devices we use to make measurements about the physical world around us[213]. Complex devices, such as explosives detectors used in airports,[214] as well as simple handheld devices, such as glucose meters that interface with cellphones,[215] are all forms of scientific instruments. As technology progresses, the improved quantity and quality of these measurements has enhanced the everyday life of society through improved healthcare (through advancements in techniques such as magnetic resonance imaging[216]), productivity (by enabling efficient planning due to enhanced forecasting abilities[217]), and safety (via sensors that can detect hazards such as indoor air contaminates[218]). However, the improvement of scientific measurements often requires more complex instrumentation and, as instrumentation become more complex, increased development time and expertise.

Mass spectrometers are highly robust instruments used in practically every field of science[89, 219-220] and are some of the most complex scientific instruments available today.[178, 221] Mass spectrometers require high-voltage electronics, complex vacuum systems, precise manufacturing, and various other difficult to handle accessories (such as cryogens, high-field magnets, compressed gases, lasers, etc.).[222-224] The data generated by modern mass spectrometers can readily exceed gigabytes in size for a single experiment[225] and operating mass spectrometers in advanced collection modes, such as data-dependent acquisition (DDA[226]), requires that data be processed and analyzed within very short timespans (i.e., milliseconds to microseconds) and in real-time.[227-228] Advances in computation speed and

algorithms have enabled breakthroughs in mass spectrometry (MS) data collection and processing capabilities; however, these capabilities often come at the cost of further increased complexity.

One of the most complex MS techniques is mass spectrometry imaging (MSI)[74]. In MSI, an image of a sample is constructed where every pixel corresponds to a full mass spectrum[73]. Although providing highly useful scientific information, MSI requires that many complex components (such as lasers, ion guns, robotic positioners, etc.) be precisely controlled in a synchronized manner with the mass spectrometer[229-230]. Furthermore, analysis of MSI data is also more complex as it requires incorporation of the additional information axes presented in MSI[231]. One notable difficulty is development of the instrument control systems utilized in MSI[232]. Such control systems must interact with numerous components, synchronize various subsystems, process complex data, and provide a user-friendly method of operation. However, these difficulties (of analyzing complex data and controlling advanced instrumentation) are not unique to imaging mass spectrometers. Many types of scientific instruments (e.g., NMR spectrometers[233], particle accelerators[234], electron microscopes[235], etc.) require (or can be improved by) powerful instrument control systems and have reached a point of complexity where large teams of scientists and engineers are required to design the necessary software and hardware components.

Rapid, collaborative development of highly complex software, such as 3D video games and modern websites, has been enabled through the development of standardized tools and platforms. For instance, video game engines (Unreal Engine,[236] Unity,[237] etc.) provide most of the functionality required for practically any form of modern, complex

game without necessitating development of the underlying subsystems (e.g., physics engines, rendering, etc.).[238-239] Similarly, creation of content-rich, interactive websites has been accelerated by the use of standardized platforms (i.e., content management systems (CMS)) like WordPress[240] and Drupal[241 242]. As a result of standardizing development platforms: (1) development times are dramatically reduced (as only development of unique functionality and content is required), (2) final product quality is significantly improved (as shared functionality and tools are often highly optimized and robust), and (3) the development skills and end-products have increased longevity (as skills are transferrable between projects and standardized platforms are regularly updated). However, despite platforms like LabVIEW[243] reducing the complexity of communicating with instrumentation hardware, a comprehensive platform and software development kit (SDK) has not been introduced for controlling complex scientific instrumentation.

Herein, we describe the development and design of DataStation One (DSO), the first comprehensive, open-source scientific instrument control platform and SDK. DSO provides asynchronous communication with numerous hardware devices, arbitrary instrument control, data analysis and management, as well as customizable user interfaces. Furthermore, we demonstrate the capabilities of DSO by utilizing it to control the various subsystems of an imaging mass spectrometer currently under development (i.e., Fourier transform ion cyclotron resonance (FT-ICR) MS, focused ion beam-scanning electron microscope (FIB-SEM) imaging, and vacuum measurement).

4.3 Experimental

4.3.1 Fourier Transform-Ion Cyclotron Resonance Mass Spectrometry

The FT-ICR system utilized herein is a repurposed IonSpec FT-ICR mass spectrometer (formerly IonSpec Corp. — now a division of Agilent Technologies, Santa Clara, CA) with a segmented, cylindrical ICR cell equipped with a tungsten filament for in-cell electron ionization. A 9.4 T superconducting magnet (Cryomagnetics Inc., Oak Ridge, TN) was used to induce cyclotron motion.

Acetone was added inside a glass bauble fixed to a Swagelok® fitting and connected to the inlet of a pulse valve (model 009-1670-900, Parker Hannifin Company, Cleveland, OH) that was mated to the vacuum chamber housing of the FT-ICR cell. The pulse valve was actuated using an Iota One pulse valve driver (model 060-0010-900, Parker Hannifin Company) that enabled precise control of the pulse of Acetone introduced into to the FT-ICR for analysis. The FT-ICR cell electron ionization (EI) filament was powered in constant-current mode at 7 A using an DC lab power supply (model 6554A; Agilent Technologies, Santa Clara, CA). Arbitrary waveforms (utilized for FT-ICR chirp excitation) were generated using a PXIe-5451 (National Instruments, Austin, TX) arbitrary waveform generator and amplified using a repurposed radio frequency (RF) amplifier (formerly IonSpec Corp.). ICR image current was measured using a differential amplifier (model 4040B; Tegam Inc., Geneva, OH) and PXIe-5112 digitizer (National Instruments). All DC bias potentials were generated using a custom MIPS system (GAA Custom Engineering LLC, Benton City, WA).

Inner trapping rings, filament trap plate, and quadrupole trap plate were held at -9.00 V, -30.0 V, and 30.0 V, respectively, for 5 ms to remove any remaining ions in the Penning

trap (ion quench). Afterwards, the inner trapping rings and trapping plates were held to 2.00 V and 5.00 V, respectively. Beginning 500 ms after ion quench, the EI filament was biased to -70 V for 4 seconds, and then set to 0 V. A series of 3 pulses (30 ms long) of the pulse valve were performed at 500 ms intervals, starting 100 ms after ion quench. At 8 seconds, ion excitation was performed by a 4 ms broadband "chirp" excitation between 30 and 150 *m/z* at ~180 V_{p-p}. Image current detection was performed 1 ms after the end of excitation and collected for 60 ms.

4.3.2 Focused Ion Beam-Scanning Electron Microscopy

The FIB system consisted of a commercial liquid metal ion source (LMIS) and associated electronics (UHV Magnum Ion Column BDS-50/BDS-200; FEI Company, Hillsboro, OR). Detection of secondary electrons was accomplished using a continuous dynode electron multiplier (CDEM) detector (part number 4035 272 05751, Detector Technology, Inc. Palmer, MA).

A custom, piezo positioning stage was manufactured by SmarAct Inc. (Up-ton, NY) using a high-precision, high accuracy, low-travel-distance stage (model PXY 38, Piezosystem Jene, Inc., Hopedale, MA) secured on top of a lower-precision, lower-accuracy, higher-travel-distance stage (model SLC-1760-S-HV positioner, SmarAct Inc., Upton, NY). The high-precision stage was not utilized in this study other than to hold the SEM imaging standard. The lower-precision stage was adjusted to optimize the FIB-SEM focal length (approximately 19.4 mm from the end of the LMIS) and to center the FIB-SEM standard grid. CDEM current data was acquired using a PXIe-5105 (NI) 60 MHz oscilloscope. Analog signals were supplied using a PXIe-6739 (NI) 16-bit, 64-channel output card.

An electron microscopy imaging grid (3.05 mm dia., 200 lines in^{-1}, Polaron Equipment, Watford, England) was adhered via conductive carbon tape to a pin mount standard holder (equivalent product number: 16119, Ted Pella, Inc., Red-ding CA) and placed on the positioning stage with the pin through the pico-positioning stage's TEM hole. The electron microscopy standard grid was imaged using the FIB-SEM system in raster mode.

4.3.3 Vacuum Measurement

The FIB-MSI system's vacuum was generated using four turbomolecular pumps, (model TMU 260, Pfeiffer Vacuum SAS, Annecy, France) backed by three Maxima C Plus roughing pumps (model 01-257-80, Fisher Scientific, Hampton, NH). Low vacuum regions (i.e., the sample gas chamber and the turbo-molecular pump exhaust tubing with pressures approximately 10^{-2} to 10^{-3} torr) were measured using four Pirani vacuum gauges with integrated controllers (275i Series Convectron Gauge, Kurt J. Lesker Company). High Vacuum regions (i.e., the FIB source chamber and differential pumping section with pressures approximately 10^{-6} to 10^{-9} torr) were monitored using two enclosed ion gauges with integrated controllers (model 354 Series Ion Gauge, Kurt J. Lesker Company). The ultra-high vacuum region that included the FT-ICR cell was monitored using a nude ion gauge (model 432004, MDC Vacuum Products LLC) with an external controller (Granville-Phillips Series 350 UHV Gauge Controller, MKS Instruments, Inc., Longmont, CO). Analog data were acquired using a PXIe-6345 (NI) multifunction data acquisition (DAQ) card (NI).

4.3.4 Instrument Control Workstation

The instrument control workstation was a Precision Tower 5810 (Dell Corp. Ltd., Round Rock, TX) equipped with 32 GB of ECC ram and a Xeon E5-1620 V3 Processor at 3.5 GHz. All National Instrument and Tegam hardware devices were housed in a PXIe-1075 (National Instruments) chassis that was interfaced to the control workstation *via* an MXI-Express x8 card (model PXIe-8381; National Instruments). Control of the GAA Custom Engineering MIPS system was performed over USB.

4.3.5 DataStation One

DataStation One (DSO) was written in Python (CPython version 3.7.0; Py-thon Software Foundation, Wilmington, DE). FT-ICR, FIB-SEM, and vacuum measurement instruments were implemented *via* both default and custom DSO modules. DSO primarily uses NumPy[244] for internal numerical data storage and PyQT5 (Riverbank Computing, LTD., Dorchester, England) for graphical user interfaces. The DSO source code is available at https://github.com/MattBrantley/DataStation. See Supplemental Material S1 for a scheme and walkthrough of the logic and internal connections comprising DataStation One.

4.4 Results and Discussion

4.4.1 DataStation One

DataStation One (DSO) is a platform and development kit for instrument control systems. DSO development was guided by eight core tenets, all towards the goal of progressing science by enabling more efficient and effective scientific instrument development. The eight core tenets are as follows:

1) Expandability: instrumentation control software should be adaptable to new scientific techniques, hardware, and project requirements with minimal effort.
2) Shared Functionality: software functionality should be transferrable between various instrument control systems whenever possible.
3) Easy-to-Use: the limiting factor of instrumentation development should no longer be the creation of instrument control software.
4) Performant: instrument control software should be responsive and not hindered by complex project demands (such as large data, numerous hardware components, or precise signal timings).
5) Instrument Agnostic: should be capable of controlling practically any form of scientific instrumentation.
6) Compatible with Existing Standards: should be capable of interfacing with all current and future standards (including hardware I/O, data storage formats, and audit/security).
7) Open-Source: all source code should be open, easily inspectable, and readily available from an online repository.
8) Providing an "All-In-One" Solution: effort should be made to equally facilitate the instrument control requirements of the design, prototyping, and deployment phases of instrument development.

DSO is written almost exclusively in Python (ten. 7), which is often used as a teaching and introductory programming language due to it's easy-to-grasp syntax (ten. 3) and numerous libraries (ten. 6). Expanding the functionality (ten. 1) of DSO is accomplished *via* simple Python scripts that are automatically loaded (ten. 3) and are abstracted from the

specific instruments being controlled (ten. 2 & 5). At its core, DSO makes use of powerful libraries such as NumPy and PyQT5 (ten. 4 & 7) and includes much of the necessary functionality for instrument control “out of the box” (ten. 2, 3, 5, 8). Additionally, DSO includes a robust library for creating customizable (ten. 1) and interactive user-interfaces.

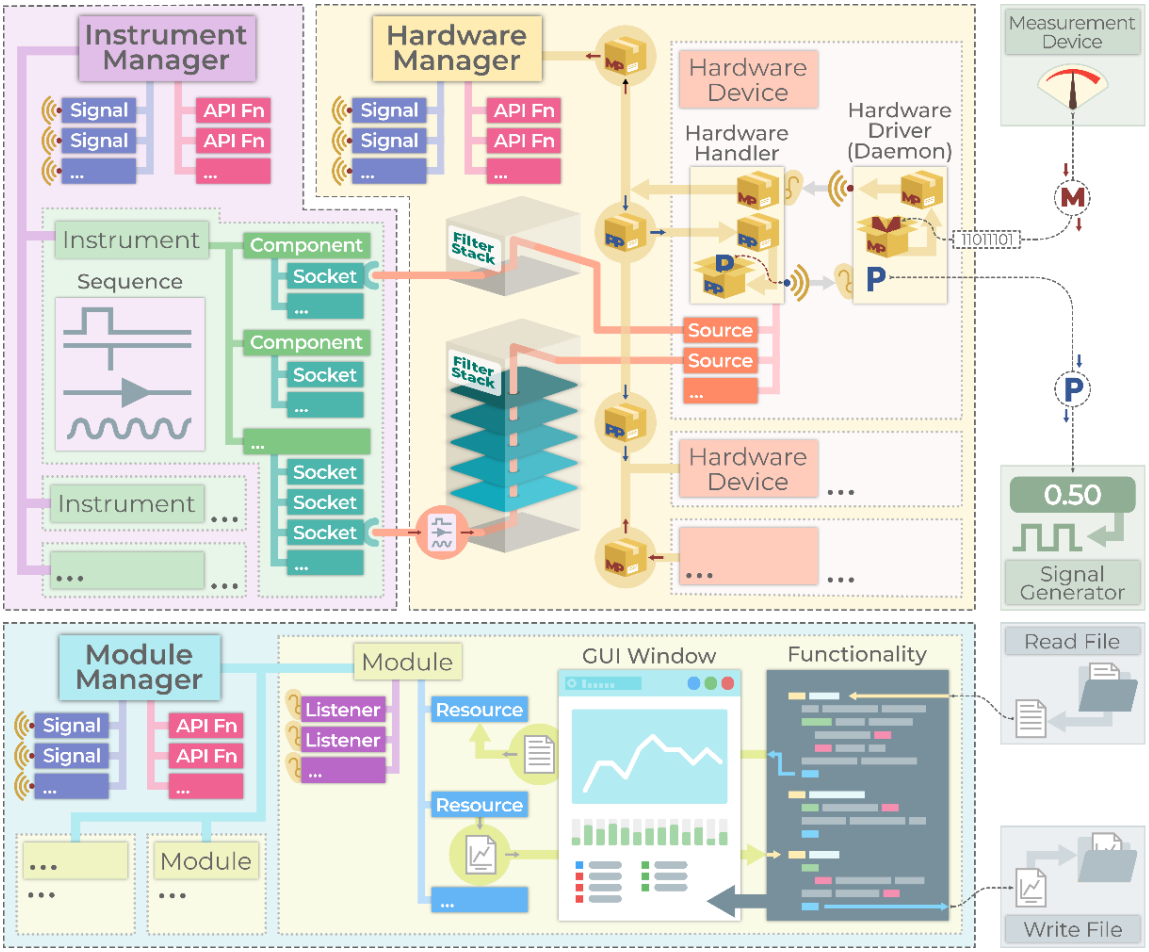

Scheme 4.1. displays the “core” of DSO and shows how the various parts of DSO interact with one another. Lightly-colored “connection” lines (e.g., the lines that travel from the green “Instrument” box to the three green boxes labeled “Component”, etc.) in Scheme 1 indicate a Python or PyQt-based connection. Where applicable, arrowheads indicate the directionality of the connection. Dashed lines with arrowheads indicate access to or from an object or file outside of DSO. Ellipses in Scheme 1 indicate a continuation of the pattern of boxes that appear similar (e.g., two green boxes labeled “Instrument” are proceeded by a third, similar green box labeled with an ellipsis, indicating that more such “Instrument” boxes could follow below).

The aforementioned capabilities of DSO are accomplished by three principal subsystems called “managers”. The internal functionality of the three managers is shown in Scheme 4.1. The Instrument Manager (Scheme 4.1; top-left), Hardware Manager (Scheme 1; top-middle), and Module Manager (Scheme 4.1; bottom-left) serve to organize the various aspects of instrumental control present in DSO. Each manager contains a list of functional pieces (i.e., Instruments in the Instrument Manager, Hardware Devices in the Hardware Manager, and Modules in the Module Manager). Each manager may be interfaced with using a series of Application Programming Interface (API) Functions (viz., pink boxes labeled “API Fn” that are connected by pink lines to the respective managers). Additionally, each manager emits Signals (viz., purple boxes labeled “Signal” that are connected by purple lines to the respective managers). Signals are emitted when the state of a manager changes (i.e., a manager receives new information about the parts it manages) or an API function is called that results in a Signal.

4.4.2 DataStation One: Instrument Manager

What is typically referred to as a scientific instrument is often comprised of multiple functionally smaller instruments combined into one package (for example, a gas chromatograph-mass spectrometer could be considered as four separate functional Instruments: the autosampler, the gas chromatograph, the mass spectrometer, and the vacuum measurement system). The Instrument Manager coordinates the many individual Instruments (Scheme 4.1; green boxes labeled “Instrument”) that are often combined to form a more complex scientific instrument. Each Instrument contains an Event Sequence (Scheme 4.1; light-indigo box labeled “Sequence”) and a set of Components (Scheme 4.1; green boxes labeled “Component”). The Event Sequence is a set of temporal instructions

for each Component which corresponds to virtually any type of input or output signals. Components may be very simple (e.g., pulse valves, triggers, switches, etc.) or more complex (e.g., quadrupoles mass filters, charge-coupled devices (CCDs), ion gauges, etc.) and define a set of Component-specific Events for use in programming the Event Sequence. Additionally, each Component contains one or more Sockets (Scheme 4.1; teal boxes labeled “Socket”) that can perform the various Component Events specified in the Event Sequence (e.g., RF waveform output, DC voltage input, etc.). Sockets are connected through Filter Stacks (Scheme 4.1; transparent boxes labeled “Filter Stack”) to Sources (Scheme 4.1; orange boxes labeled “Source”). Filter Stacks and Sources are managed by the Hardware Manager and are discussed below.

4.4.3 DataStation One: Hardware Manager

The Hardware Manger coordinates the many Hardware Devices (Scheme 1; boxes labeled “Hardware Device”) necessary for signal generation and measurement. Hardware Devices are capable of programming a single piece of physical, electronic hardware (e.g., a digital power supply or oscilloscope). Each Hardware Device contains a Hardware Handler (Scheme 4.1; tan box labeled “Hardware Handler”), a Hardware Driver (Scheme 1; tan box labeled “Hardware Driver (Daemon)”), and one or more Sources. Each Source corresponds to a single input or output channel on the hardware device (e.g., channels 1 and 2 on a 2-channel oscilloscope).

The Hardware Handler within a Hardware Device is automatically generated upon creation of a Hardware Driver and facilitates asynchronous communication between DSO and the Hardware Driver. Each Hardware Driver is a Python script that interfaces directly with a given electronic device (such as the, previously mentioned, digital power supply or

oscilloscope) by sending programming instructions and/or receiving measurement data. The paired Listeners (Scheme 4.1; ear icons) and Signals between the Hardware Handler and Hardware Driver pass Measurement Information (Scheme 4.1; dark-red "M") and Programming Information (Scheme 4.1; dark-blue "P") to each other.

As depicted in the Hardware Driver in Scheme 4.1, the Hardware Driver receives Measurement Information from a Measurement Device, packages the Measurement Information as a Measurement Packet (Scheme 4.1; the iconic representation of putting the "M" in a cardboard box labeled with "MP"), and emits the Measurement Packet as a Signal to the Hardware Handler. Conversely, the Hardware Driver takes Programming Information and relays it to a Signal Generator. As depicted in the Hardware Handler in Scheme 4.1, the Hardware Handler receives a Measurement Packet and relays that Measurement Packet to the Hardware Manager. The Hardware Handler also receives and extracts Programming Information from a Programming Packet (Scheme 4.1; the iconic representation of removing the "P" from a cardboard box labeled with "PP") before emitting a Signal containing the Programming Information to the Hardware Driver's paired Listener.

Filter Stacks are DSO representations of analog signal processing that occurs between a Signal Generator/Measurement Device and the scientific instrument. For instance, an ion lens (indicated within DSO as a Component) might require a DC voltage (indicated within DSO as a Socket) of 20–40 V. However, a digital power supply may only be able to produce a maximum output of 2 V (indicated within DSO as a Source). A 20x voltage-amplifier might be placed after the output of the digital power supply to boost the produced voltage into the 20–40 V range. DSO allows the amplifier to be represented as a Filter

within a Filter Stack and automatically translates between the Source-Socket connections (e.g., an Event corresponding to 30 V would be modified to program the Socket to output 1.5 V). Many Source-Socket connections do not have any filters applied (but will still have an "empty" Filter Stack, as indicated by the transparent "Filter Stack" box in Scheme 4.1).

4.4.4 DataStation One: Module Manager

The Module Manager coordinates Modules (Scheme 4.1; lime-green boxes labeled "Module"), which are self-contained scripts of Python code that may contain any Functionality (Scheme 4.1; dark gray box labeled "Functionality") that a Python script might have (e.g., data processing, web scraping, Sequence creation, etc.). Additionally, each Module may also possess a custom Graphical User Interface (GUI) Window (Scheme 4.1; white box labeled "GUI Window") generated using PyQt5. Examples of GUI Windows are: an interactive plot, a list of readbacks and settings, a user-profile window, a fully-functional web browser, etc. Modules create and contain Resources (Scheme 4.1; light blue boxes labeled "Resource"). Resources are similar in nature to Measurement Packets and store data that can be saved or loaded from files. Resources can be accessed from other Modules for use in data processing, modifying module behavior, etc. Modules are capable of interacting with the various Managers by calling the Managers' API Functions as well as creating Listeners for receiving the various Manager Signals. More information on Scheme 1, including a walkthrough of a FT-ICR workflow may be found in Appendix Scheme C.1.

4.4.5 DataStation One: User Scripting

In alignment with the tenant of Expandability, many of the constructs within DSO are defined by scripts which can be written or expanded by the instrument developer.

Within the Instrument Manager, Components and their Events are all described in simple scripts (an example Component script of a DC electrode can be seen in Code C.1). Hardware Drivers utilized by the Hardware Manager are also user scripts which supply the various state-machine functions required for operation (an example Hardware Driver of a PXIe 5451 waveform generator can be seen in Code C.2). Filters are scripts defining the analog signal processing occurring outside of DSO (an example Filter of a log-linear voltage transform for a 275i vacuum gauge can be seen in Code C.3). Modules utilized by the Module Manager are also Python scripts, although Modules can be notably more complex when incorporating GUI elements (a simple Module that implements an interactive Python console example can be seen in Code C.4. This Python console module can be used to observe the internal state of DSO in real-time, as shown in Appendix Figure C.1).

Although the individual user scripts may have seemingly limited capabilities, the true power of DSO is realized when many of these small scripts are combined. As such, DSO provides instrument developers a streamlined interface for developing "bite-sized" functionality without becoming encumbered by scale (for instance, identifying and correcting bugs in code is far simpler when contained in this manner). The truly modular nature of DSO allows for extensive re-use of scripts and is in alignment with the tenant of Shared Functionality**.**

4.4.6 Imaging Mass Spectrometry System

To demonstrate the capabilities of DSO, three different Instruments (an FT-ICR MS, a FIB-SEM, and a vacuum measurement instrument) of an imaging mass spectrometer currently being developed were controlled. The parts of each Instrument

(and their relative locations) are depicted in Scheme 4.2. For each Instrument described below, custom Component, Hardware Driver, Filter, and Module scripts were written and are discussed.

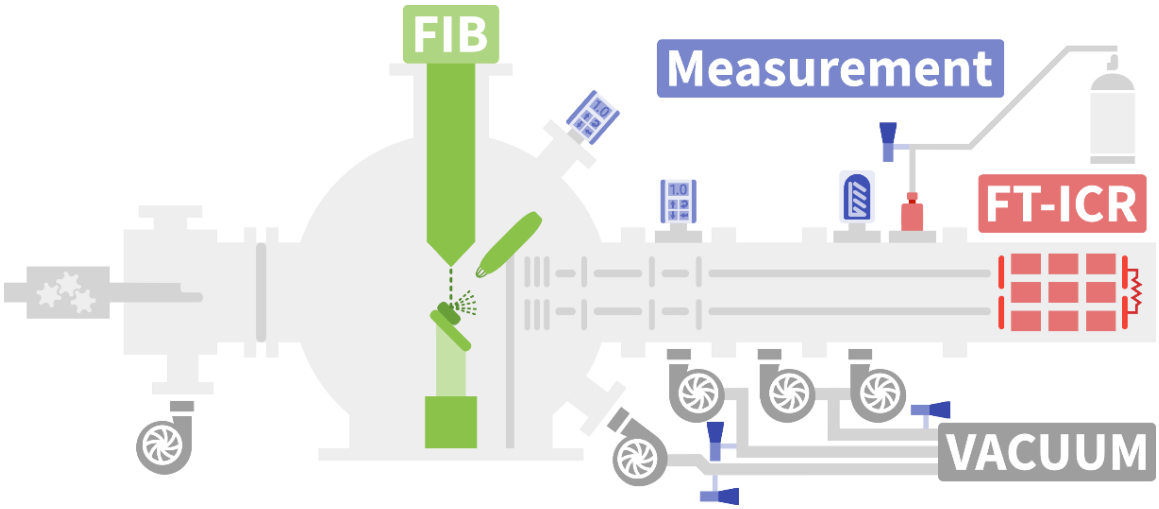

Scheme 4.2. displays the physical layout (not to scale) of the three Instruments controlled by DSO. The FT-ICR MS Instrument (in red) displays the pulse valve used to introduce Acetone into the ICR cell, the trapping rings, the trapping plates, the excitation and detection plates, and the EI filament. The FIB-SEM Instrument (in green) displays the positioning system, the gallium ion source, and the CDEM that allows for imaging. The Vacuum Measurement Instrument (in purple) displays the four Pirani gauges, the two enclosed ion gauges with integrated controllers, and the nude ion gauge.

4.4.7 Fourier Transform-Ion Cyclotron Resonance Mass Spectrometry

This first demonstration of DSO was control of the FT-ICR mass analyzer portion of the imaging mass spectrometer described above. FT-ICR is a high-resolution mass spectrometry technique wherein the cyclotron frequency of ions are determined by measuring the differential image current generated as they pass across two detection plates.[93] The flight path of ions in FT-ICR is very long and thus requires trapping ions for seconds at a time using highly stable trapping potentials. In addition, timings of ion excitation, detection, trapping potentials, and pulse valve must all be executed with sub-µs precision.[161]

For the FT-ICR, all DC biases and timing pulses were provided by the MIPS system (GAA Custom Engineering). The MIPS system used a sparse data lookup table for adjusting signal outputs, which enabled the long (> 8 seconds) experimental sequence to be stored fully in MIPS memory with the required sub-μs precision timepoints. For comparison, a sub-μs granularity (i.e., >1 MHz) continuous waveform with 8 channels of information would be tens to hundreds of MB in size. Two digital output channels of the MIPS were dedicated to triggering the excitation and detection events.

Three Hardware Driver scripts were written to interface with (1) the MIPS system, (2) the PXIe-5451 (excitation) device, and (3) the PXIe-5105 (detection) device. For each Hardware Driver, a script was written that defined each state of the Instrument state-machine (e.g., program, run, abort, etc.) with a predetermined function. DSO requires that Hardware Driver scripts account for all possible states and will not load any scripts that are only partially completed (to prevent accidental system lock-up).

Six custom Component scripts were written, each representing electrode(s) in the FT-ICR instrument. The first three scripts (representing the trapping plates, inner trapping rings, and EI filament) were simply the generic, DSO-provided "DC Bias Electrode" Component, with new graphical icons. The Component script representing the pulse valve was created using the included "TTL Pulse" Component. The Component script representing the FT-ICR detection plates was written without using a template component. However, the FT-ICR detection plate Component script was facile as only a single Event type ("N-Count Measurement") needed to be defined. In contrast, the Component script representing the FT-ICR excitation plates required multiple Event types be defined to describe the many possible arbitrary waveforms used in FT-ICR excitation (e.g., "chirp"

excitation, sustained off-resonance irradiation (SORI), stored waveform inverse Fourier transform (SWIFT), etc.). Additionally, each Event in the FT-ICR excitation plate Component script included the relevant code for digital waveform synthesis.

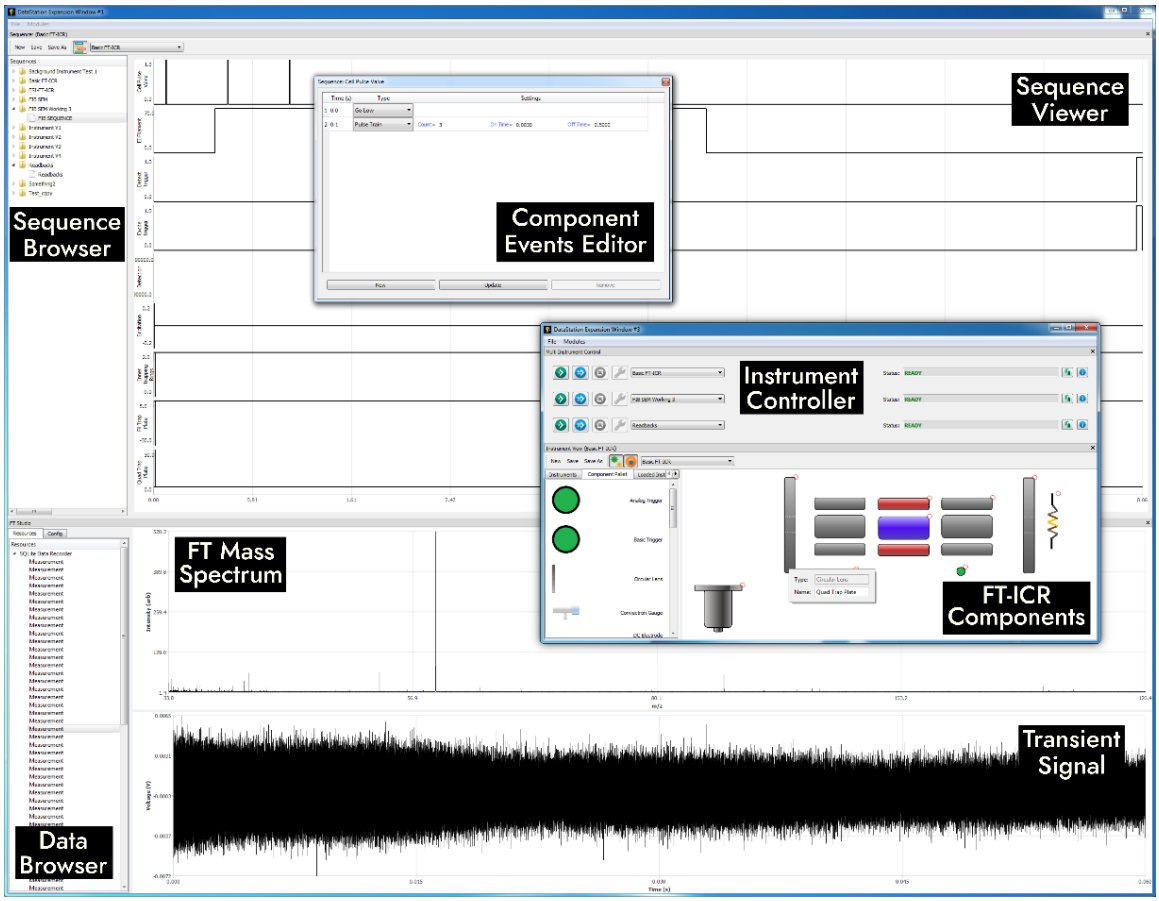

Figure 4.1. displays a screenshot of the GUI Windows of modules used in the control of the FT-ICR. The GUI Window labeled "Sequence Viewer" displays temporal plots of the Events that are performed by the various FT-ICR Components (labeled in small text to the left of each temporal plot and displayed as icons above the "FT-ICR Components" label). The pop-out window is a sub-window that is generated for each Component to allow editing of the Component's Events. The Sequence Browser allows for saving and loading of Sequences. The Instrument Controller checks whether each of the three Instruments (FT-ICR, FIB-SEM, and Vacuum Measurement) is ready and allows execution of each of the Instruments' Sequences (by clicking a "run" button). The Data Browser displays past measurements (all labeled "Measurement") and allows loading of previously-acquired data. The plots labeled "Transient Signal" and "FT Mass Spectrum" display the acquired raw data (the Transient Signal) as well as the automatically Fourier-transformed signal that has been converted to a mass spectrum.

Once the necessary Component scripts had been constructed, a new Instrument was created in DSO and instances of the Component scripts added to the Instrument. These tasks were performed using the "Instrument View" module included with DSO, which can be seen in Figure 4.1 (window labeled FT-ICR Components). When Component instances had been added to the Instrument, the desired experiment was described using the "Sequencer" module included with DSO (Figure 4.1; window labeled "Sequence Viewer") by right-clicking on the relevant timeline to open the event editor dialog and selecting from a drop-down list of Events (as defined in Component script). DSO uses a universal JSON storage format for Sequences, which can be serialized and deserialized using simple API functionality within the Instrument Manager (for saving and loading of Sequences, Figure 4.1; window labeled Sequence Browser).

Only universal modules included with DSO have been utilized for setting up the FT-ICR Instrument and configuring its Event Sequence. For instance, an included module (Figure 4.1; window labeled Instrument Controller) allows each instrument to be run and various ready-check information be inspected. However, FT-ICR transient data is not easily understandable until after Fourier analysis and conversion from frequency to mass-to-charge (*m/z*). Unlike the previous tasks, the Fourier analysis functionality is highly specific to the operation of a single type of instrument (Fourier transform-mass spectrometers). Although it is possible to export the transient data to an external data analysis suite, DSO allows development of custom Modules. These custom modules provide advantages over traditional data acquisition and analysis workflows as, for instance they can remove the need for cumbersome data transport between software or even supply the ability to automatically upload data to a web server.

The “FT Studio” Module was developed specifically for analysis of FT-MS transient signals within DSO and makes use of the Module Resource functionality (the Data Browser section of the FT Studio Module in Figure 4.1 shows transients contained as Resources in other Modules, in this instance from the “Universal SQLite DataLogger” Module). Various FT-ICR-specific functionalities have been implemented in the “FT Studio” Module, such as Fourier transform, windowing functions, and adjustments for magnetic field strength. Additionally, a GPU-accelerated user interface was incorporated for displaying and interacting with the transient and resulting mass spectra. An example FT-ICR spectra collected for acetone is shown is displayed in the “FT Studio” Module shown in Figure 4.1.

4.4.8 Focused Ion Beam-Scanning Electron Microscopy

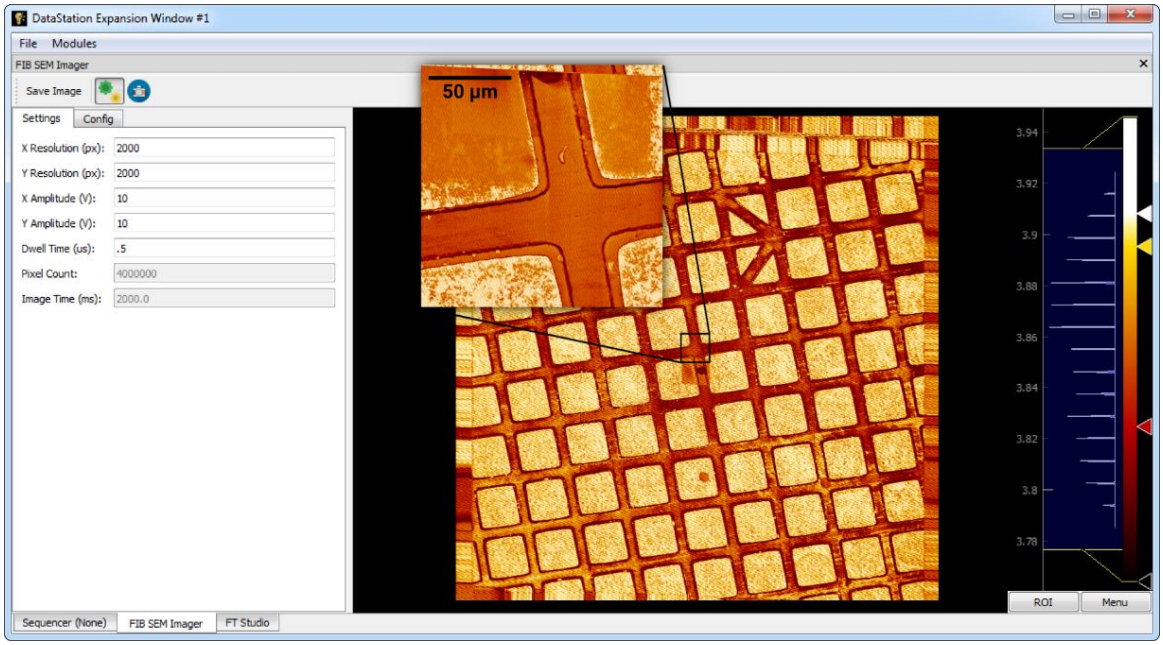

Figure 4.2. displays a screenshot of the GUI Window of the Module used for control and data acquisition for the FIB-SEM Instrument. The zoomed-in "pop-out" (including the scale bar and black zoom-in lines) was manually added from an additional screenshot (not shown) where the settings (a list of the changeable settings is displayed on the left-hand side of Figure 4.2) had been altered to magnify the image. A histogram of the intensity values detected is displayed on the right-hand side of Figure 4.2.

The second demonstration of DSO is the control of the focused ion beam-scanning electron microscope (FIB-SEM) in the source of the imaging mass spectrometer. FIB-SEM imaging is performed by ablating a sample with focused Ga^+ ions from the FIB and measuring the emitted electrons (i.e., secondary electrons) emitted from the surface by a continuous dynode electron multiplier (CDEM). By moving the Ga^+ beam in a raster (i.e., line-by-line) and detecting the secondary electron current, an image of the sample can be reconstructed.

In contrast to the FT-ICR experiments discussed previously, the FIB-SEM experiments were shorter (100–2000 ms) and occurred in rapid succession to generate a video signal. Two sawtooth waveforms were generated using a PXIe-6739 (National

Instruments) to deflect the Ga^+ beam in the X (scan-line) and Y (vertical) directions. A single channel of an 8-channel oscilloscope (PXIe-5105; National Instruments) was used to observe the secondary electron signal (from the CDEM). Synchronization of the beam deflection signals and the signal acquisition was achieved by splitting the Y (vertical) beam deflection signal to a second channel on the 8-channel oscilloscope and configuring the analog acquisition trigger to monitor the second channel. The signal acquisition was configured to start in sync with the rise of the Y (vertical) beam deflection signal. Clock sources for the PXIe-5105 and PXIe-6739 were configured to utilize the 100 MHz reference timer of the PXIe-1075.

Two Hardware Driver scripts were written to interface with the PXIe-6739 and PXIe-5105 devices, respectively. All signal inputs and outputs used in the FIB-SEM Instrument were not modified by any analog signal processing (such as amplifiers, filters, etc.) so no Filter scripts were necessary. A Component script was written for the deflection plates, which allowed for the generation of the necessary sawtooth waveforms. The CDEM detector Component was almost identical to the detection plate Component used in the aforementioned FT-ICR Instrument.

A Module called the “FIB-SEM Imager” (Figure 4.2) was developed so the FIB could be controlled and SEM images visualized in a user-friendly manner. On the left panel of Figure 2, various instrument parameters can be adjusted. Each time an adjustment is made, the FIB-SEM Imager Module recalculates the necessary sequence parameters for the FIB-SEM Instrument so that the next image is produced using the updated settings. Additionally, various image statistics are calculated (such as imaging time).

During the operation of DSO, each time a Measurement Packet is registered by the Hardware Manager a Signal is emitted. The FIB-SEM Imager Module includes a Listener for this Signal that indicates a new image has been collected and should be displayed. However, not all Measurement Packets being registered by the Hardware Manager necessarily correspond to the FIB-SEM Instrument (since DSO can run multiple Instruments simultaneously). Thusly, the FIB-SEM Imager Module intelligently filters the Measurement Packet Signals it receives and only operates on those Signals corresponding to the FIB-SEM Instrument. When a Measurement Packet corresponding to the FIB-SEM Instrument is received, the FIB-SEM Imager Module reshapes the incoming 1D waveform from the CDEM into a 2D array corresponding to the image pixel intensity values. This 2D array is then displayed as an image (as shown on the middle of Figure 4.2).

4.4.9 Vacuum Measurement

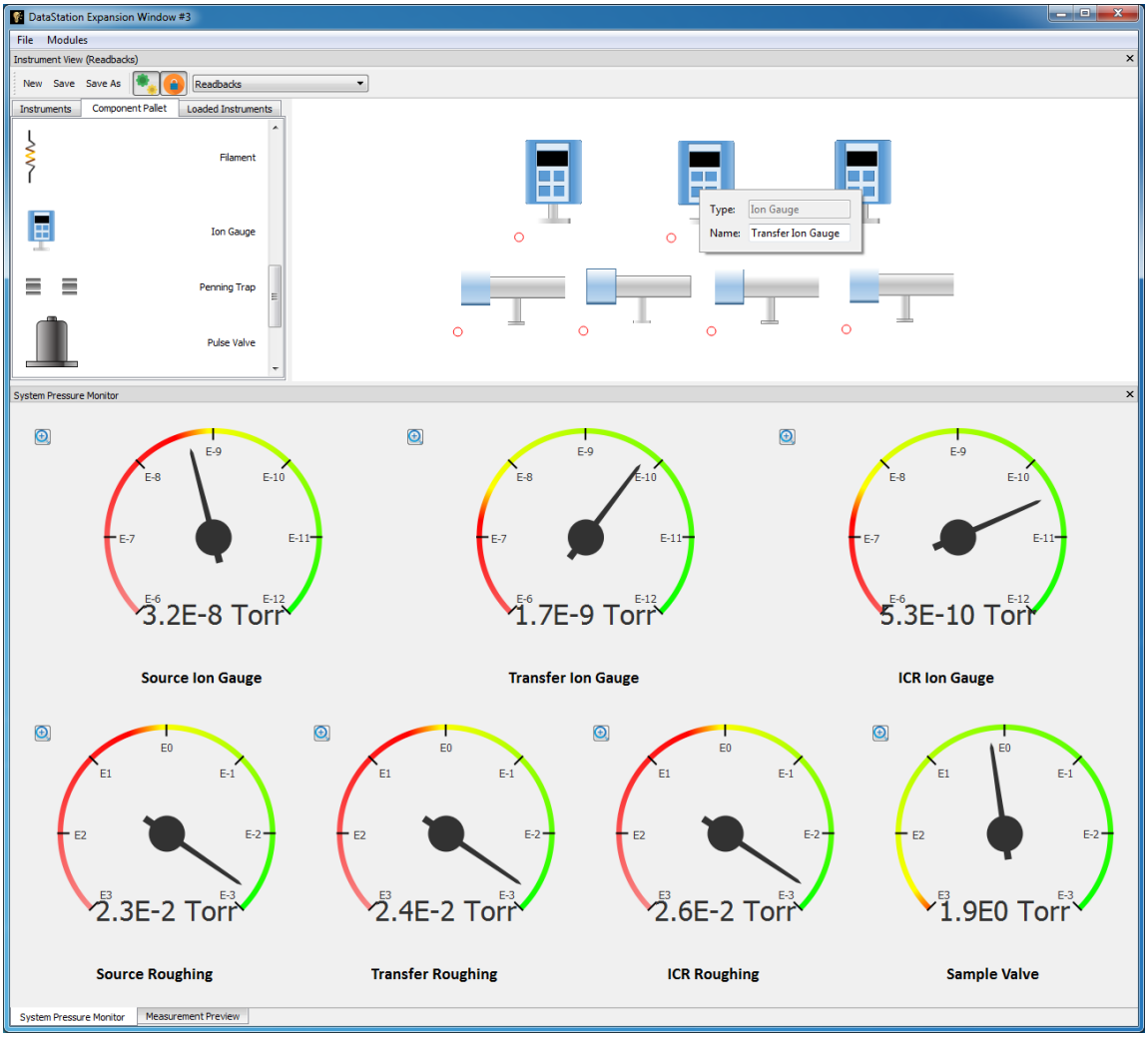

Figure 4.3. displays readbacks for the seven pressure measurement devices. The Source, Transfer, and ICR roughing readbacks as well as the Sample Valve readback (depicted as dials at the Bottom of Figure 3) are measured from the four Pirani gauge Components (depicted as icons in the top portion of Figure 3). The Source, Transfer, and ICR ion gauges (depicted as dials in the middle of Figure 3) are measured from the three ion gauge Components (depicted as icons in the top portion of Figure 3). The nude, ICR ion gauge has a different Hardware Driver than the two, integrated, Transfer and Source ion gauges but is the same Component due to the abstractions provided by DSO.

The final demonstration of the broad applicability of DSO is an Instrument corresponding to the vacuum measurement devices. Unlike the previous two examples, the vacuum measurement Instrument was designed to run continuously (instead of only when

an experiment is being performed). The vacuum pressures of a scientific instrument are very important (especially when working with pressure sensitive Instruments like the FT-ICR) and should be easily visible to the instrument operator. Each pressure measurement device (i.e., Pirani or ion gauge) was configured to report the pressure as a log-linear voltage and the appropriate sense-lines were connected to a PXIe-6345 (National Instruments).

A single Hardware Device script for interfacing with the PXIe-6345 was created for the vacuum measurement Instrument. Three different types of measurement devices were utilized (a nude ion gauge, two enclosed ion gauges, and four convectron-enhanced Pirani gauges), each of which provided a different log-linear voltage scale. As such, one Filter script was created for each measurement device type (a total of 3 Filter scripts). Two Component scripts were written, corresponding to the ion gauges and the convectron-enhanced Pirani gauges. In both cases, a single Event was added to the Component script that enabled the collection of a single-point voltage measurement. The Instrument Sequence file was populated with each of the gauges' collection Events.

As with the previous examples, a custom Module (Figure 4.3; window labeled "System Pressure Monitor") was created for integrating with the vacuum measurement Instrument. The System Pressure Monitor Module was written to update a series of seven logarithmic gauges upon a Measurement Packet Signal. Because the pressure values were already converted from voltage to Torr units by the Filter script (previously mentioned), no additional data operations were necessary. However, it would be relatively trivial to introduce logic in this Module to sound an alarm or send an automated email about Instrument pressures should a pressure threshold be exceeded.

4.5 Conclusion

We have developed an "all-in-one" instrument control platform and SDK, DataStation One (DSO), that allows for development of expandable, easy-to-use, and performant, instrument control software that maintains compatibility with existing standards. We have described the use of DSO in the creation and operation of three separate scientific instruments (an FT-ICR, a FIB-SEM, and a vacuum measurement system) that all can combine to form an MSI system (currently under development). We have provided instructional materials and example scripts (of the four kinds of scripts that a user of DSO would be required to write or supply: the Component, Filter, Hardware Device, and Module scripts) for assisting users of DSO to perform rapid instrument development. Although DSO was created to enable rapid, complex instrument development, we also anticipate DSO to be useful for both simple and prototype instrument development.

CHAPTER FIVE

Overview of Dissertation and Future Directions

5.1 Dissertation Overview

Chapter One begins by providing an introduction into the field of mass spectrometry and its broad application in scientific research. Next, the three core sections of the mass spectrometer (the source, analyzer, and detector) are introduced with examples and fundamental discussion. In the second half of Chapter One, discussion into the unique engineering considerations of mass spectrometers starts by describing the application and theory of vacuum pumps, electronics, and software. Towards the end of Chapter one, a survey of the field of imaging mass spectrometry is presented with a specific focus on the unique capabilities and engineering difficulties it entails.

In Chapter Two, progress towards the development of a custom imaging mass spectrometer is presented. Chapter Two begins by explaining the theory of operation for the imaging mass spectrometer and offers discussion into the benefits and drawbacks of this approach. The middle of Chapter Two highlights the many various developments made, such as the vacuum system, ion optics and simulation, electronics, and electromechanical components. Throughout the development of the imaging mass spectrometer, unique solutions to various engineering and experimental requirements were addressed and are discussed here. Chapter Two concludes by discussing preliminary results related to the certain aspects of the imaging mass spectrometer.

Chapter Three introduces a new technique for rapid characterizations of ion optics called Segmented Monte Carlo (SMC), using the ion trajectory simulation software

SIMION. SMC utilizes a hybrid Monte Carlo and genetic algorithm approach that is orders of magnitude faster at solving arbitrary ion geometries than Monte Carlo alone. In addition, SMC includes many quality-of-life features that lower the barrier of entry for ion trajectory simulations while still providing high-quality numerical descriptions of arbitrary ion geometries. Three different ion optics arrays were evaluated using SMC. In each case, results were stringently compared against known theory. For ion trajectories capable of being solved from first principles, analytical results (first principles) and numerical results (simulations) were in excellent agreement.

Chapter Four describes Data Station One (DSO), a new development platform for instrumentation control software. In this chapter, the problems arising from the increasing complexity of scientific instrument (and especially mass spectrometers) are discussed and explanation for how DSO addressed these problems are provided. DSO is unique in that it is capable of controlling practically any type of scientific instrument, which is demonstrated in three detailed examples of unique instruments controlled using DSO. Furthermore, each example instrument controlled using DSO corresponded to an individual subsystem of the imaging mass spectrometer being developed – highlighting the applicability for DSO for both simple and complex instrument control software problems.

5.2 Future Directions

5.2.1 Field Ionization

While RFI as a post-ionization technique has several unique benefits (no heat emission, no light emission, and can be pulsed; see Section 2.1.2). The underlying ionization mechanism is understood to be an electron ionization mechanism[51] which, as previously discussed in Section 1.2.1.1, is considered to be a very "hard" (*i.e.*, destructive)

ionization technique. As such, under best-case conditions the post-ablation ionization spectra would be complicated by the introduction of numerous fragment ion species for each molecular ion. Exploring other ionization techniques capable of softer ionization would be beneficial to the goals of the project, if available.

One potential alternative to RFI, for application in the proposed imaging mass spectrometer, is field ionization (FI).[61] FI is performed by passing a molecules through a high electric field gradient (upwards of 10^8 V/cm).[60] These high field gradients are achieved using special emitters that resembles a very small pipe cleaner, with many tiny "hairs" or bristles. When traveling through this high field gradient, a gas molecule can have inner-shell electrons tunnel out of the molecule to FI emitter producing radical cations ($M^{\bullet+}$). This tunneling event is non-disruptive to the bonds of the analyte molecules and, thus, FI is a very "soft" ionization mechanism. FI possesses several properties that make it ideal for the imaging mass spectrometer described in this document, namely: it is a soft mechanism of ionization, compatible with high and ultra-high vacuum, and capable of pulsed and continuous operation.

Field ionization has fallen out of use in recent decades and is commercially available in only two forms today, as an optional ion source on the AccuTOF GCx (Jeol USA, Inc.) and as a hybrid device called a liquid introduction field desorption ionization (LIFDI) source from Linden CMS. The FI source utilized in the AccuTOF GCx is not separately purchasable and thus a LIFDI source is the only option available (aside from custom implementations that could take years without the proper expertise). The LIFDI

source is unique in that it allows for both the ionization of gaseous molecules and (*via* a fine capillary) introduction of liquid samples followed by field desorption/ionization (FDI).

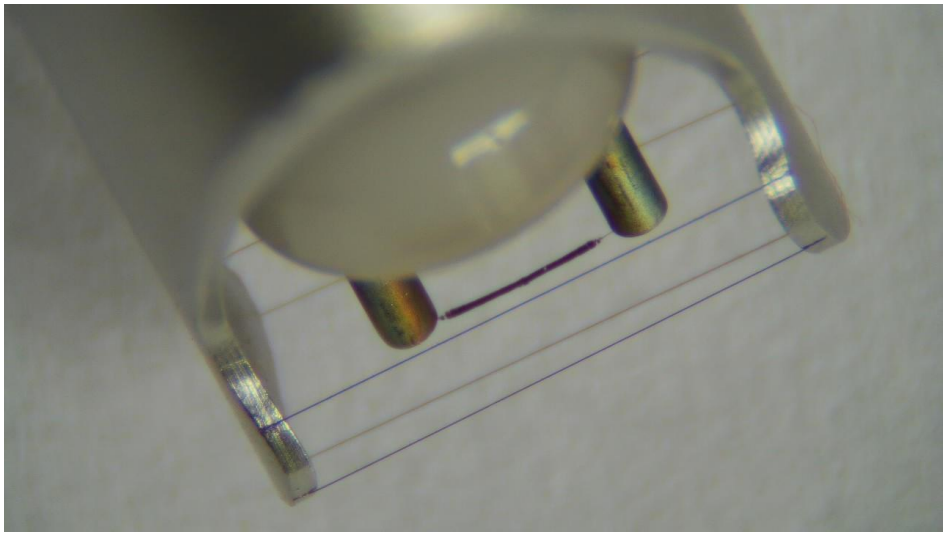

Figure 5.1. A picture of a custom-designed LIFDI source to accommodate for a large ion volume. The emitter is visible between the two "posts" of metal.

A custom prototyped LIFDI probe was designed and tested by Linden CMS and is shown in Figure 5.1. Four distinct benefits of this probe design exist, which are of particularly unique advantage for this imaging mass spectrometer. (1) The ionization volume is much larger than other FI sources (>1 cm^3) through the use of multiple counter-electrodes. (2) The counter-electrodes are grounding electrodes, thus allowing the Ga^+ LMIS to operate with minimal interference. (3) The LIFDI source is designed for aftermarket use and can be inserted vertically through a hole in the bottom plate of the source vacuum system for positioning between the sample stage and extraction optics assembly. (4) The liquid introduction system would allow ion generation (and even unique

experiments) immediately before the ion extraction optics – thus allowing ion accumulation, transfer, and FT-ICR testing independent of the post-ablation ionization.

5.2.2 Super-Resolution Imaging Mass Spectrometry

5.2.2.1 Proposal summary. Imaging mass spectrometry is a valuable tool for studying biological tissues. Common imaging ionization methods, such as matrix-assisted laser desorption/ionization (MALDI) have been combined with time of flight (TOF) mass analyzers and Fourier transform-ion cyclotron resonance (FT-ICR) mass analyzers to form imaging mass spectrometers (IMS). TOF MSI is impressive in its ability to generate an image quickly (>50 pixels per second). However, it is unable to reliably achieve mass resolutions above ~20,000. FT-ICR MSI is equally impressive in that it is able to achieve ultra-high mass resolving power (~300,000+). However, FT-ICR MSI is unable to generate an image at more than ~0.5 pixels per second.

There is a growing problem in that, as MALDI and focused ion beam (FIB) ionization sources are improved to allow higher spatial resolution imaging, the need for faster scanning mass spectrometers is also increasing. At the same time, the growing understanding of biochemical processes means the need for better mass discrimination (i.e., mass-resolution) is increasing as well. The balance of mass-resolution and spatial-resolution has long been a discussion for imaging mass spectrometry, yet a single approach allowing both has yet to be introduced.

Herein, we propose a chemometric method of combining the rapid image generating capabilities of a TOF MSI with the ultra-high re-solving power of an FT-ICR MSI. Utilizing this algorithm, sporadic (i.e. spatially limited) FT-ICR MSI data may be used to elucidate fully-imaged TOF MSI data, generating a ‘super-resolution’ image

comparable in mass discrimination to that of an image created fully with FT-ICR MSI data, but in a fraction (i.e., 1-2 orders of magnitude) of the time of FT-ICR MSI alone. In this proposal, we report preliminary results using the 'super-resolution' algorithm which exhibit its ability to discriminate previously TOF-unresolvable isobaric peptides using sporadic high-resolution mass spectral information.

5.2.2.2 Background. Mass spectrometry-based imaging of tissue samples is predominately accomplished using matrix-assisted laser desorption/ionization time of flight imaging mass spectrometry (MALDI-TOF MSI).[74, 79, 245] In MALDI,[246] a sample is suspended or coated in a suitable matrix and then bombarded with a (typically ultraviolet) laser. MALDI is a relatively soft ionization technique[247] and is commonly used in conjunction with TOF[90] mass analyzers, which discriminate mass-to-charge ratios (*m/z*) of ions based on the time it takes each for species to hit a detector (after receiving a constant acceleration potential).

Additional types of imaging mass spectrometers exist, such as secondary ion mass spectrometry (SIMS) which replaces the ultraviolet laser used in MALDI with a focused atom[81-82] or ion[248] beam. While greatly outperforming MALDI in terms of beam size,[230] SIMS is limited in its ability to generate large (> m/z 500) ions.[249] An additional technique known as desorption electrospray ionization (DESI)[250-252] is capable of softly ionizing tissue surfaces by directing a charged electrospray plume directly onto a tissue surface. While this technique is capable of producing intact ions of relatively large biomolecules, it suffers in spatial resolution when compared to MALDI.[154]

Cutting-edge MALDI-TOF MSI have been assisted by Fourier transform ion cyclotron resonance (FT-ICR)[93] for high mass-resolution imaging of tissue samples.[253-255]

This is typically performed by taking a 'first pass' using a MALDI-TOF MSI, then transferring the sample to an FT-ICR MSI and reimaging. Due to the relatively lengthy duty cycle of an FT-ICR MSI experiment (0.1–0.5 pixels per second (pps) when compared to 50+ pps for a TOF MS), the pixel size of an image must be increased many times (100 or more when compared to the TOF pixel size) to be able to fully scan the tissue sample in a reasonable time (i.e., several hours).[253, 256] Because of this, most tissue imaging with MALDI FT-ICR has been done with pixel sizes in excess of 100–400 μm[79, 245, 257-259] Thus, there is a problem with MSI in that it is not possible, within a reasonable timeframe, to obtain both ultra-high mass resolution (i.e. ≥ 300,000 M/ΔM) and high spatial resolution.

This problem is increasing as advancements in MALDI MSI and SIMS MSI have reduced the possible pixels size to below 100 nm^2.[260-261] The difficulties of improving instrument duty-cycle while maintaining sensitivity, and resolution (in both the image and mass spectrum domains) dramatically increase as pixel size decreases.[262-263] Our group has been making advances in the field of chemometrics (i.e., the study of applying mathematical and statistical models on chemical data) by improving the ability to resolve isobaric and isomeric compounds with traveling wave-ion mobility mass spectrometry.[264-269] Additionally, our group has experience with both the development of custom instrumentation[49, 51, 270] as well as theoretical simulations of ions under various electric and magnetic fields.[211]

Table 5.1. A comparison of current MALDI imaging methods to the proposed chemometric method utilizing an FT-ICR/TOF MS.

	TOF IMS	FT-ICR IMS	'Super-Resolution' IMS
Duty Cycle (pps)	50+	0.1 to 0.5	50+
Resolution (ΔM)	< 20,000	> 300,000	> 300,000
Sensitivity	High	V. High	High
Imaging time (145 k pixels)	< 48 min	80 – 400 h	1.5 h (spot checking)

Proposed is a chemometric method whereby the simultaneous collection of sporadic high mass-resolution data with low mass-resolution MS images can be combined to yield an image comparable to that of one composed only of high mass-resolution data. Utilizing our 'super-resolution' algorithm, data may be deconvoluted through data-independent (direct measurements) and improved through data-dependent (spot checking) analysis. Thus, the image generated using the techniques and algorithms presented herein can maintain the operating speed of a low mass-resolution image but contain comparable information to an image generated with only high mass-resolution data.

5.2.2.3 Specific aims. The three specific aims of this project are as follows:

Aim 1: Improve current algorithms for deconvoluting images composed of low-resolution mass spectral data by utilizing sporadic high mass spectral data.

Aim 2: Modify our existing FT-ICR imaging system to allow for tandem TOF experiments without spatial, ionization, or temporal variations of the sample to be imaged.

Aim 3: Image rat brain tissue at a pixel size of ≤ 200 nm^2 with an FT-ICR and TOF, utilizing limited, sporadic FT-ICR data to resolve convoluted mass spectral peaks in the complete TOF image.

5.2.2.4 Chemometric approach – tandem mass spectrometry imaging. With the proposed 'super resolution' method the acquisition may be performed in parallel. The benefits of this are, first, that the low duty-cycle instrument (FT-ICR) is able to detect as the high duty-cycle instrument (TOF) is concurrently sampling (Figure 5.2). Second, with a tandem approach a single imaging and ionization source may be utilized. The benefits of this are reduced sample variations between detectors and minimization of potential sample degradation or chemical modifications associated with long imaging times or sample movement.

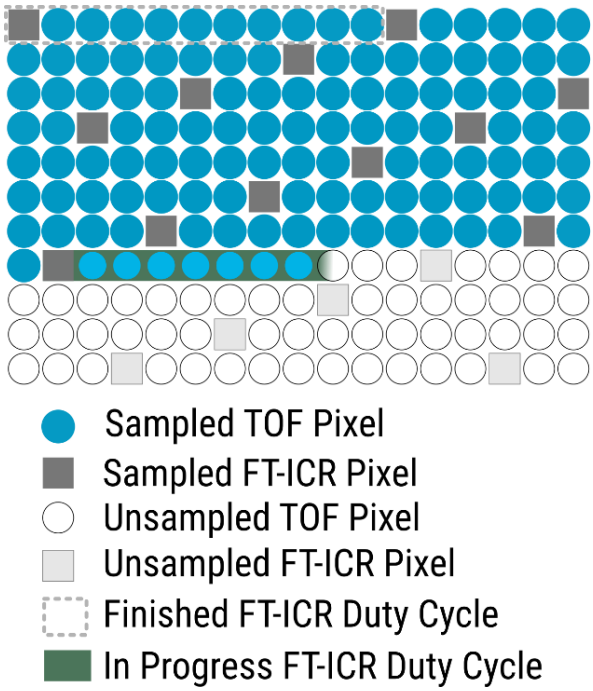

Figure 5.2. Simplified representation of the proposed tandem raster imaging approach interlacing FT-ICR (*i.e.*, high mass-resolution) and TOP (*i.e.*, high spatial-resolution) measurements on a single sample.

As both MS detectors are operated simultaneously on the same sample and the results temporally interlaced, the sample itself may be prepared once and fully imaged. While the benefits of a single sample preparation are manifold, the true advantage of this approach is an increase in spatial resolution and reproducibility (as rastering the image, or relative positioning, is far more accurate than attempting to find a previously scanned pixel's location, or absolute positioning).

Once the tandem imaging is complete, the sporadic high mass-resolution data is then peak picked for centroids and intensities. This data is then interpolated across the full spatial-resolution of the image to generate a prediction map for each centroided peak (Figure 5.3).

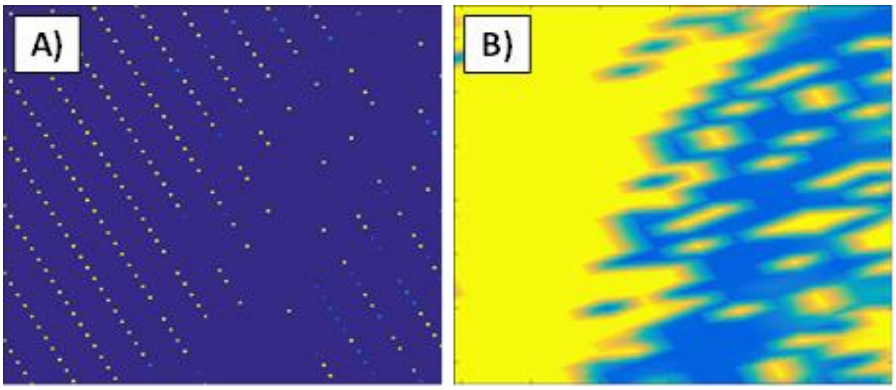

Figure 5.3. (A) Sporadic high mass-resolution image data for a single mass centroid. (B) Interpolation map of data in A.

Using the interpolated prediction map, a poly-modal model of Gaussian distributions is generated for each low mass-resolution pixel. These models are generated using fixed centroids (*i.e.*, μ's; from high mass-resolution interpolation maps) and predicted peak widths (*i.e.*, σ's; predicted from TOF mass spectra). For each low mass-resolution pixel, these models are fit to the TOF mass spectral data to determine the

intensities of each underlying component. These components and their respective intensities make up the "super-resolution' TOF mass spectra.

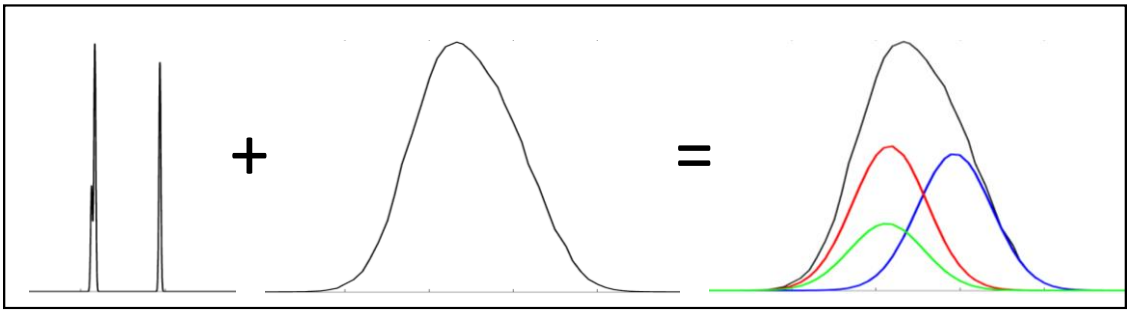

Figure 5.4. (Left) High-resolution (*i.e.*, 300,000 mass resolving power) mass spectrum showing three isobaric components. (Center) Low-resolution (*i.e.*, 10,000 mass resolving power) mass spectrum showing the same three isobaric components which are convoluted. (Right) 'Super-resolution' mass spectrum of the three deconvoluted isobaric components.

For each pixel, a goodness of fit parameter is recorded (between the solved predictive model and the TOF mass spectral data). In cases where the high mass-resolution interpolation maps fail to successfully provide a good fit model for TOF deconvolution, an additional data-dependent analysis step can be performed. This optional step involves identifying high-error (i.e., poor fit) regions in the 'super-resolution' image and performing additional high mass-resolution measurements in those regions (Figure 5.5). This newly-gained information is then used to regenerate high mass-resolution interpolation maps and subsequently incorporated into the 'super-resolution' image (via modifying relevant fitting models). The extent of this data-dependent 'spot checking' can be limited by either error thresholds or simple time constraints (Scheme 5.1).

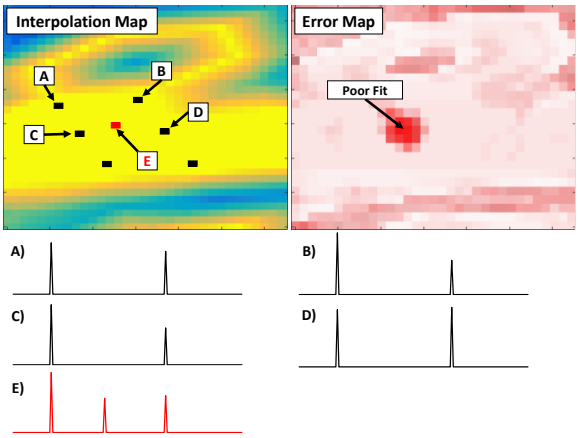

Figure 5.5. (Left) Example of a scenario where interpolation of the high-resolution data (A-D) fails to properly represent true populations. (Right) Error map indicating the location of poor fit, leading to resampling (i.e., spot checking) of sample point E. (Bottom) Representative high-resolution mass spectra for points A-E.

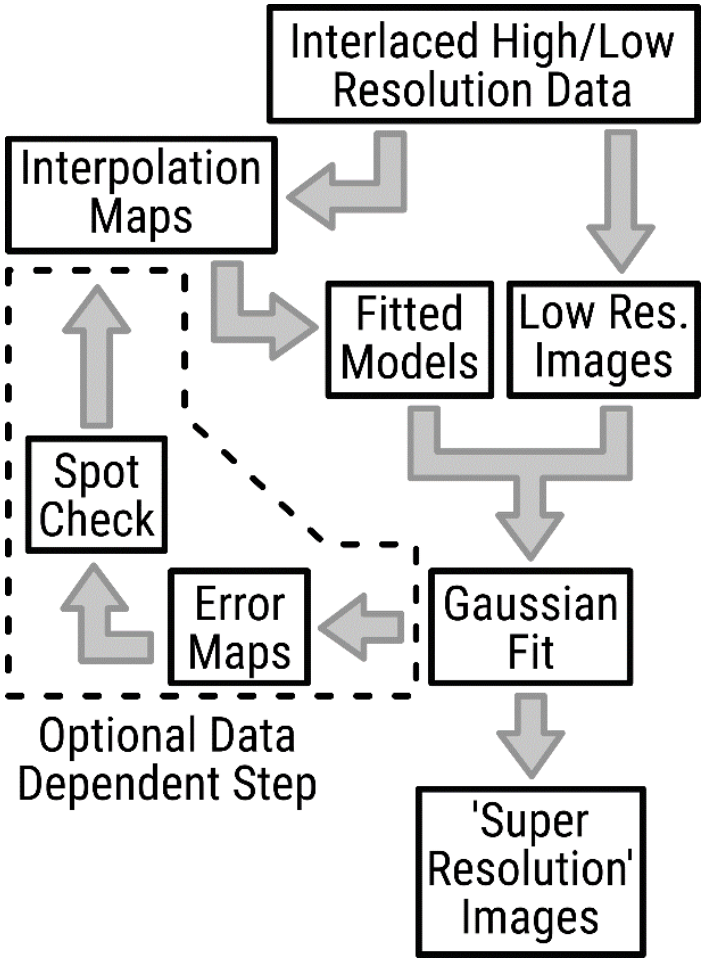

Scheme 5.1. Proposed experimental workflow beginning with the collection of interlaced high/low resolution data and ending with a final 'super-resolution' image. An optional data dependent step is also highlighted with dashed lines.

5.2.2.5 Experimental design. Currently our software is capable of resolving simulated low-resolution imaging data given additional sporadic high-resolution information (Figure 5.6). This high mass-resolution information may either be in the form of peak centroid lists or high-resolution mass spectra. However, a number of optimizations and improvements can be made to both the software design and its underlying algorithms. First, the deconvolution algorithm begins to provide increasingly erroneous information as s/n decreases (i.e. s/n > 250) (Figure 5.8). Improvements in the peak interpolation and fitting algorithms, such as weighted fitting parameters, could decrease this threshold. Second, the imaging processing algorithm takes a significant amount of time to de-convolute the data (~30 minutes for an image containing 145,000 pixels, which is slightly be-low the estimated ~48-minute collection time with MALDI-TOF). Processing time could be dramatically reduced by utilizing multi-threaded programming techniques and more computationally efficient fitting algorithms. Third, the 'sampling' locations of the FT-ICR data is simplistically derived (it samples as soon as the duty cycle is over, which leads to an even-interval sampling frequency which can produce uneven sample coverage). Fourth, the data-dependent resampling is done manually after consulting a generated 'error map' (Figure 5.5) but will be automated for future application.

Each of these areas for improvement are relatively straightforward to address, however combined they would amount to a substantial improvement in the method. Updating and improving the deconvolution and peak-fitting algorithms will serve to improve the final 'super-resolution' images, making the method more robust in terms of solving harder convolutions in terms of signal-to-noise and complexity (*i.e.*, more than 2–3 species). By refactoring and re-writing the code in a more computationally efficient

method, taking advantage of modern computer's ability of multi-threading, and by enhancing the algorithms involved, the processing time for each image will be greatly reduced. This will enhance the techniques ability to perform 'on-the-fly' spot checking as well as improving the overall workflow. By intelligently varying the sampling rate of signals sent to the FT-ICR, a more complete map of the tissue may be obtained without encountering the difficulties of accurately repositioning a rastered primary (MALDI or FIB) beam.

Our current 9.4 T custom imaging FT-ICR is designed around a modular, expandable framework. Instrumental additions are relatively facile given this modular framework. Using our highly precise positioning and rastering system, and any of our available primary beams (*i.e.*, N_2 Laser, CO_2 Laser, or liquid gallium ion beam), our system is capable of extreme spatial resolutions as low as 10 nm^2.

Our data control and acquisition hardware/software is likewise highly expandable. Most electronics (i.e., pusher frequency controls and signal acquisition components) necessary for the addition of a TOF MS detector are already available within our existing electronics. However, a few additional components would be necessary, as listed in Table 5.2.

Table 5.2. List of necessary electronics and hardware components for addition of TOF MS detector. (Total: $16,000)

Item	Role	Approx. Cost
Micro-Channel Plate (MCP)	TOF MS Detector	$8,000
MCP Amplifier Components	Power Supply & Bias	$2,000
4-foot CF Vacuum Tube	Time-of-flight Tube	$3,500
DC-DC Boost Converter	'Pusher' High-Voltage Source	$500
Misc. Parts and Electronic Components	Cables, Bolts, Gaskets, Connectors	$2,000

One consideration of the ion-source is the ability to add a large-bore instrument or window onto one side. The TOF itself would be composed of an electronic 'pusher' that would be placed in the existing accumulation cell portion of our imaging FT-ICR. This 'pusher' element would then apply an acceleration voltage orthogonally, ejecting the accumulated ions into the flight chamber where they would separate by m/z prior to impacting the microchannel plate. While a home-built TOF would likely be unable to achieve commercially available TOF mass resolutions, the mass resolution (i.e., peak width) of the low-resolution image is negligibly important to the 'super-resolution' algorithm when compared to the mass analyzer sampling rate (the data point density on a mass spectrum), the signal-to-noise ratio of the mass spectrum, and the reproducibility of said spectrum.

Aim 3 would culminate in the analysis of rat brain tissues containing neuroblastomas at various stages of development. Using the 'super-resolution' algorithm we would look to identify previously unresolved indicators of neuroblastoma formation.

These results would be shared with the greater scientific community in hopes of catalyzing new avenues of research in cancer. While Aim 3 would benefit substantially from both the completion of Aims 2 and 1, it is not necessary for either to be completed. Utilizing existing commercial FT-ICR / TOF MS imaging capabilities (where the two techniques are used independently in series, rather than in parallel) and our existing software, it would be possible to deconvolute the TOF MS data utilizing sporadic FT-ICR data. This is to say that existing instrumentation can benefit from the 'super-resolution' technique. The 'super-resolution' method could easily be extended to a single mass analysis method such interlacing high-speed (~50 ms) low-resolution FT-ICR data with very slow (~10 s) sporadic ultra-high-resolution FT- ICR data from the same instrument.

5.2.2.6 Preliminary work. As a proof of concept showing the utility of the 'super-resolution' algorithm, a semi-empirical data set was generated for selected isobaric tryptic digest peptides of Tubulin, Ubiquitin, and P73. Image maps for Tubulin and Ubiquitin derived peptides were generated from data re-ported by Stauber *et al.*[127] In their report, Stauber and coworkers successfully resolved two isobaric tryptic digest peptides from Tubulin and Ubiquitin *via* ion mobility separations prior to MS analysis. While the exact identity of these peptides was not discussed, they are presumed to correspond to the EGIPPDQQR (*m/z* 1039.5167) fragment of Ubiquitin-40S [Rattus norvegicus] and the YLTVAAVFR (*m/z* 1039.5935) fragment of Tubulin beta-4B [Rattus norvegicus].

Tumor protein 73 (i.e., P73) is an assumed tumor suppressor (due to its structural similarity to P53[271]) and has been shown to be overexpressed in some rat tumors, including neuro-blastomas[272]. P73 tryptic digests can produce several peptide fragments, one of which is the oxidized peptide ENFEILMK (m/z 1039.5129) which is isobaric to the

previously mentioned tryptic peptides from Ubiquitin and Tubulin. Due to its potential relevancy as a tumor indicator and the formation of a peptide isobaric with the previously mentioned peptides, P73 is an interesting target for 'super-resolution' imaging. However, as no P73 imaging data was available for this particular tissue sample, a synthetic population map for P73 was created.

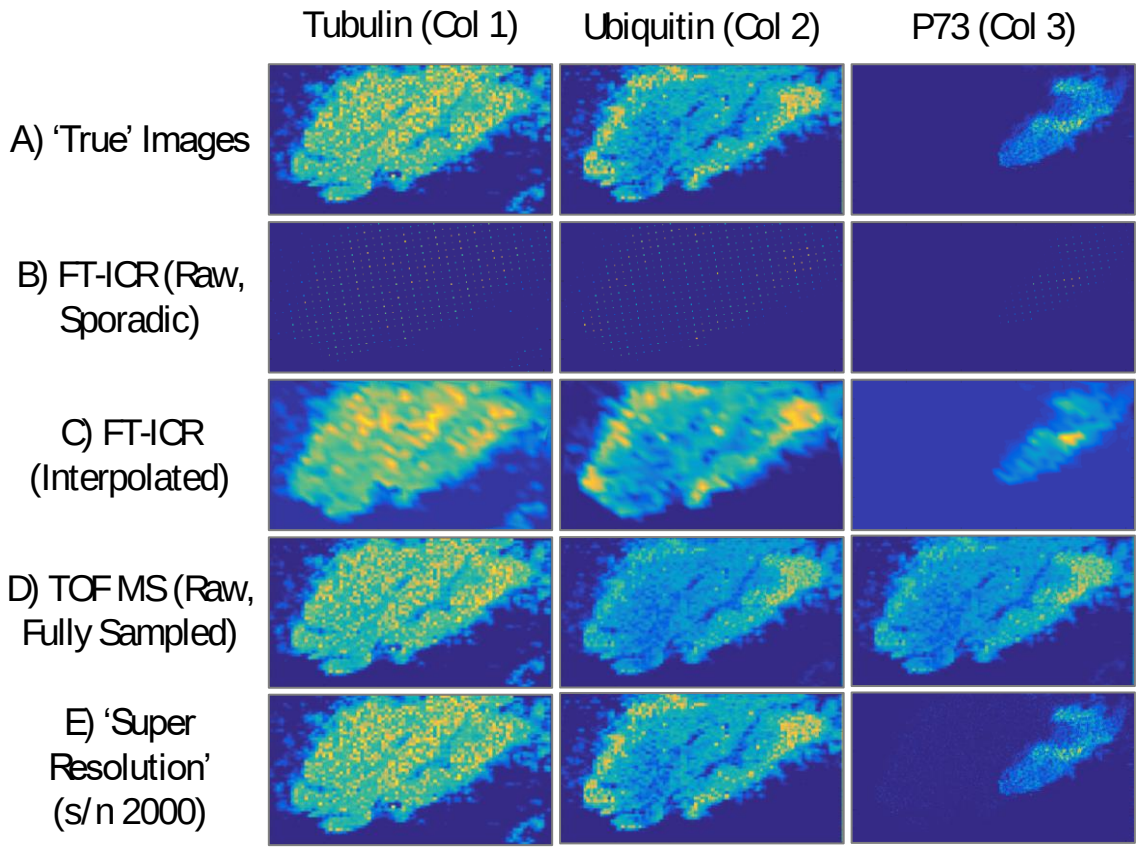

Figure 5.6. Plot of three components (*i.e.*, Tubulin, Ubiquitin, and P73) at various steps in the proposed 'super-resolution' chemometric approach. Row E 'super-resolution' results compare favorable to the 'true' populations shown in Row A.

Figure 5.6 shows at various steps of the afore-mentioned chemometric process. Row A shows images representation the 'true' (*i.e.*, perfect) population maps of the representative tryptic digest product for Tubulin (column 1), Ubiquitin (column 2), and P73 (column 3). Row B shows the simulated sporadic high-resolution FT-ICR mass spectra

(*i.e.* mass resolving power of 300,000) for each digest product. Row C contains the interpolation maps for each digest product based on the sporadic information contained in Row B. Images shown in Row D represent select ion images for each tryptic digest product using simulated low mass resolution TOF data (*i.e.* mass resolving power of 10,000). TOF data alone is still capable of resolving between the products of Tubulin and Ubiquitin (ΔM of 0.0768 Th) but unable to resolve between the products of Ubiquitin and P73 (ΔM of 0.0038 Th). These results are expected, as resolving between the two tryptic digest products of Tubulin and Ubiquitin requires a mass resolving power of ~13,500 (close to the simulated mass resolving power of 10,000). However, resolving between the products of Ubiquitin and P73 would require a mass resolving power of ~270,000 (which is currently unachievable using TOF MS alone). Row E shows the 'super-resolution' images generated using both high mass-resolution FT-ICR MS and high spatial-resolution TOF MS data. 'Super-resolution' images compared favorably to the 'true' population maps shown in Row A and demonstrate the utility of this technique.

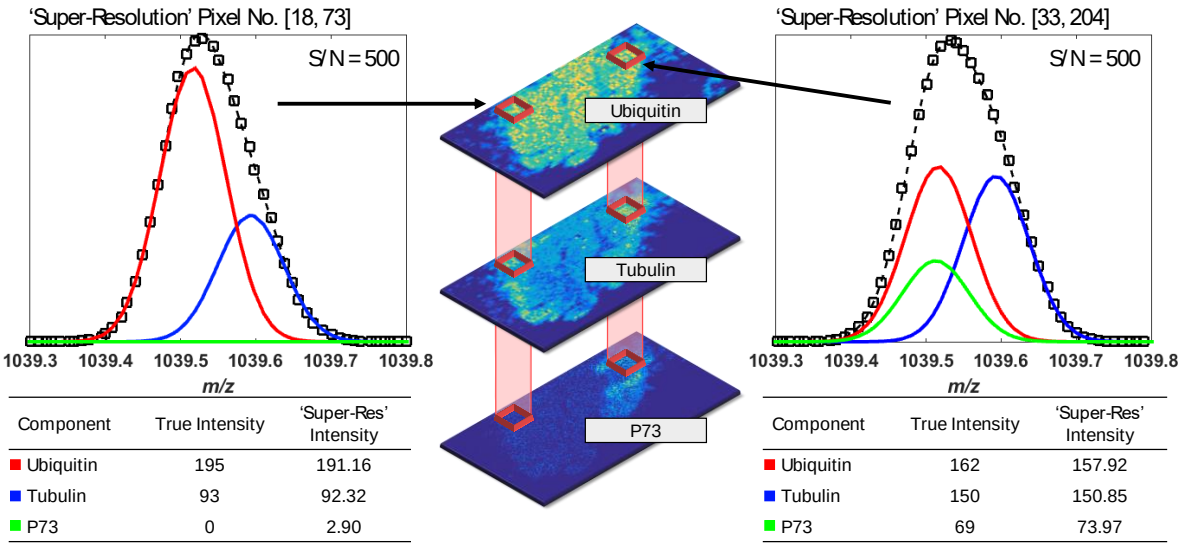

Component	True Intensity	'Super-Res' Intensity
Ubiquitin	195	191.16
Tubulin	93	92.32
P73	0	2.90

Component	True Intensity	'Super-Res' Intensity
Ubiquitin	162	157.92
Tubulin	150	150.85
P73	69	73.97

Figure 5.7. A comparison of two pixels and their respective 'Super-Resolution' mass spectra at S/N 500. The black dashed line indicates the fitting data and the black boxes represent simulated low mass-resolution peaks. The red, blue, and green lines (Ubiquitin, Tubulin, and P73 respectively) indicate the deconvoluted data.

Figure 5.7 shows examples of two successful fitting scenarios using the 'super-resolution' algorithm and s/n of 500. Low signal-to-noise (s/n) can have a significant impact in the ability of the 'super-resolution' algorithm to discern be-tween closely related isobaric compounds. Figure 5.8 shows 'super-resolution' images of the previously mentioned tryptic digest products at various simulated s/n levels. As s/n decreases, the ability of the 'super-resolution' algorithm to discern between populations of the Ubiquitin and P73 products is significantly reduced. However, Tubulin and Ubiquitin products remain resolvable even in the lowest simulated s/n 'super-resolution' image as their ΔM is approximately 20x larger than that of the Ubiquitin and P73 products. Some spatial information for the P73 product can be restored by applying an interpolation mask (Figure 5.8).

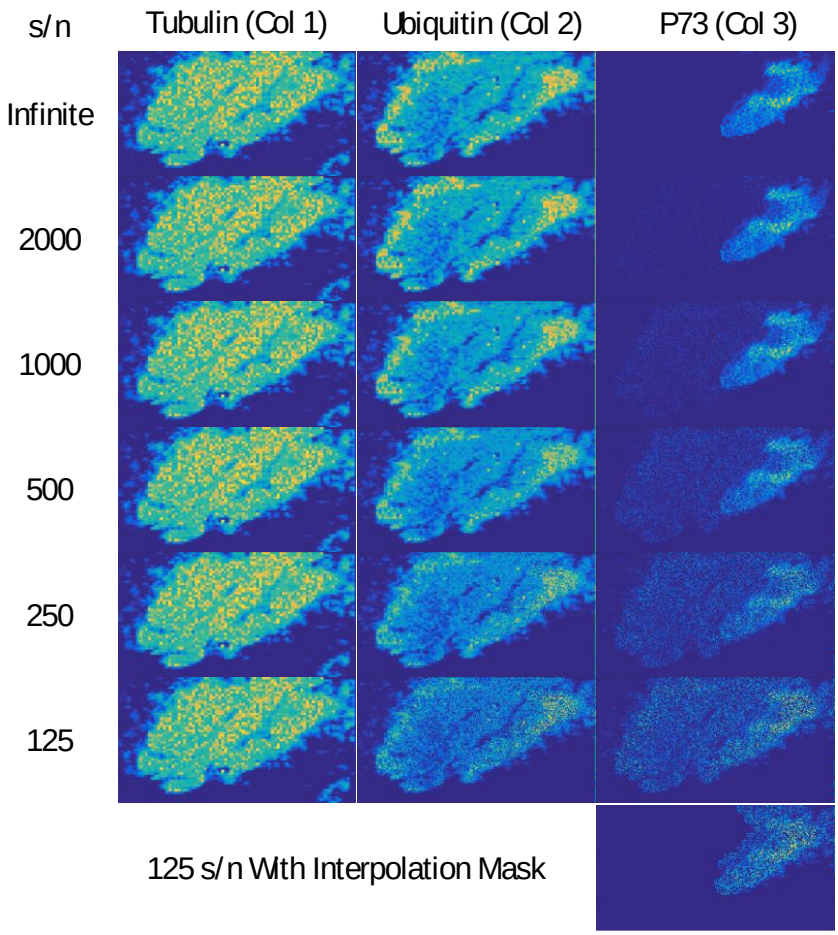

Figure 5.8. Plot of three 'super-resolution' components (*i.e.*, Tubulin, Ubiquitin, and P73) at various simulated s/n. An interpolation mask for s/n 125 is also shown at the bottom right.

The data in Figure 5.6, Figure 5.7, and Figure 5.8 show that by utilizing this 'super-resolution' imaging technique we are able to generate an image comparable to that of the 'true' population image from sporadic high mass-resolution and fully-sampled low mass-resolution data.

5.2.2.7 Significance and conclusions. With recent improvements in ablation and ionization techniques for imaging, the corresponding need for a high-speed high-resolution imaging mass spectrometer is clear (as a linear decrease in pixel size increases the number of pixels needed to cover an identical area by a power of two). Yet, with this same decrease

in pixel size comes a need for even greater sensitivity (as less material is ablated). With the scientific community's collective increase in understanding of biochemical processes comes the necessity for greater mass discrimination. However, at this time improving mass resolution comes at a significant cost to instrument duty-cycle and/or pixel size.

Our proposed 'super-resolution' imaging technique mitigates the negative tradeoffs be-tween mass resolution, spatial resolution, and duty cycle in mass spectrometry imaging. The proposed research would provide advances in the fields of instrumentation, analytical chemistry, image processing, and biochemistry.

5.2.2.8 Difficulties. Currently, the 'super-resolution' algorithm does not account for many known instrumentation variables. For instance, mass shifts between different mass analyzers could potentially lead to poor fitting results. Additionally, mass drifts[273] (i.e., change in mass calibration during image collection) could also negatively impact the ability to generate accurate 'super-resolution' images. Limitations in mass windows (such as the low-mass cutoff of an FT-ICR[161, 211]) could limit the utility of this technique to certain mass ranges. Although currently unaccounted for in the 'super-resolution' algorithm, many of the aforementioned difficulties can be negated by integrating continuous calibration verifications and additional quality control metrics.

Incorporation of the TOF mass analyzer to our existing imaging FT-ICR could pose several potential difficulties. For example, efficiently directing ions to the appropriate mass analyzer is expected to pose a number of instrumentation challenges, such as sensitivity loss and low TOF mass resolving power. Our group's experience with SIMION (Scientific Instrument Services, New York, USA) allows us to rapidly prototype, simulate, and optimize various instrument geometries prior to physical construction. Additionally,

the Baylor Science Building is equipped with a full machine shop for minimum turnaround of most custom instrument components.

APPENDICES

APPENDIX A

Ion Mobility-Mass Spectrometry Deconvolution

Early in graduate school, I was able to contribute to research focused around the deconvolution of ion mobility-mass spectrometry data. This research was outside the scope of this dissertation; however, the research was productive and impactful enough to necessitate inclusion in this document. The dissertations of Dr. Michael Pettit,[274] Dr. Mahsan Miladi,[275] and Dr. Brett Harper[276] include discussion on this particular research topic.

Ion mobility (IM) is technique for separation gas-phase ions by their collision cross-sections (CCSs)[277] and has been coupled with mass spectrometry.[190] IM is performed in many different ways,[278] such as temporally dispersive,[279] spatially dispersive,[280] and confinement/release.[281] Furthermore, ion mobility has been used for analysis of a wide variety of analytes, such as proteins,[191], metabolites,[282] and others.[190] However, while a highly useful technique, IM remains limited in its peak capacity[283] when compared to more established chromatographic techniques.[284]

One method of increasing peak capacity in IM is through instrumental modifications. A specific example of this was published by Giles *et al*. wherein they demonstrated, through improvements in their instrumentation, that they were able to separate doubly-charged ions of the isomeric peptides SDGRG and GRGDS.[285] These two peptides were previously unresolvable. However, work published by Zekavat *et al*., demonstrated that chemometric deconvolution was an alternative to expensive instrumental modifications for improving the effective peak capacity in IM.[269] Building on these principals, Brantley *et*

al. improved upon the IM deconvolution process and released the Automated Ion Mobility Deconvolution (AIMD) software.[264] The AIMD software was used to demonstrate the effective separation of the same SDGRG and GRGDS peptides (doubly-charged) without instrumental modifications.[264]

Research into the applications of ion mobility deconvolution continued. Pettit *et al*. studied the effects of collision energy on ion fragment formation and subsequent deconvolution success.[266] In this work, successful deconvolution of a trinary mixture of saccharides, in addition to a quaternary mixture of isomeric peptides, was demonstrated through fine optimization of collision energies.[266] Work by Harper *et al.*, demonstrated the successful calculation of collision cross sections for unresolved isomers using ion mobility deconvolution.[286]

With successful deconvolution of ion mobility becoming easier, an onus was placed on automated analysis. However, at this point ion mobility deconvolution remained a highly targeted approach, requiring the selection of individual ion mobility elution profiles.[264] One solution to this was presented by Brantley *et al.* where, building on previous works of Miladi *et al.*,[275] ion mobility peak widths were measured to indicated the presence of multiple isomers/isobars.[287] The presented software, IM_FIT, automatically fit experimental data and measured peak widths. By plotting the peak width as a function of drift time for a given charge state, baseline trends were observed and presumed to be single-conformation species. Peaks with abnormally wide distributions would deviate from this baseline trend and could be selected for targeted analysis.[287]

An additional solution was presented by Pettit *et al*., wherein the mass isolation requirement of IM deconvolution was removed.[288] This broadband approach increased

sensitivity and allowed for deconvolution of multiple, separate drift populations within a single instrument run. Additionally, the first demonstration of successful deconvolution of unknown isobars in LC-IM-MS was performed using a rat brain digest sample.[288]

APPENDIX B

Supplementary Information for Chapter Three: A Segmented Monte Carlo Approach for Unsupervised Optimization of Ion Optics in Mass Spectrometers

Table B.1. Ion optic geometries for the “resolving quadrupole” and “digital quadrupole” experiments

Component	Parameter	Value(s)		
Entrance Lens	Position	0 mm_x	0 mm_y	40 mm_z
	Rotation	0 °x	0 °y	0 °z
	Thickness	2 mm		
	Inside Radius	2 mm		
	Outside Radius	30 mm		
Quad	Position	0 mm_x	0 mm_y	170 mm_z
	Rotation	0 °x	0 °y	0 °z
	Length	2 mm		
	Rod Radius	3.175 mm		
	Inscribed Radius	2.764 mm		
Entrance Lens	Position	0 mm_x	0 mm_y	300 mm_z
	Rotation	0 °x	0 °y	0 °z
	Thickness	2 mm		
	Inside Radius	2 mm		
	Outside Radius	30 mm		

Table B.2. SMC Parameters used in the “resolving quadrupole” and “digital quadrupole” experiments

SMC Parameter	Value	
mz_start	50	*m/z*
mz_end	2000	*m/z*
mz_interval	50	*m/z*
mz_interval_ion_count	10	
max_failures_for_step	50	
max_failures_for_reset	50	
max_ion_flight_time	1000	µs
trajectory_quality	-1	

Table B.3. Monte Carlo bound for SMC components in the “resolving quadrupole” experiment

Component	Parameter	Min		Max	
Entrance Lens	DC	-50	V	50	V
Quad	Resolve DC	0	V	200	V
	Offset DC	0	V	0	V
	RF Amp	50	$V_{b\text{-}p}$	3000	$V_{b\text{-}p}$
	Freq	1.0	MHz	1.0	MHz
Exit Lens	DC	-50	V	50	V

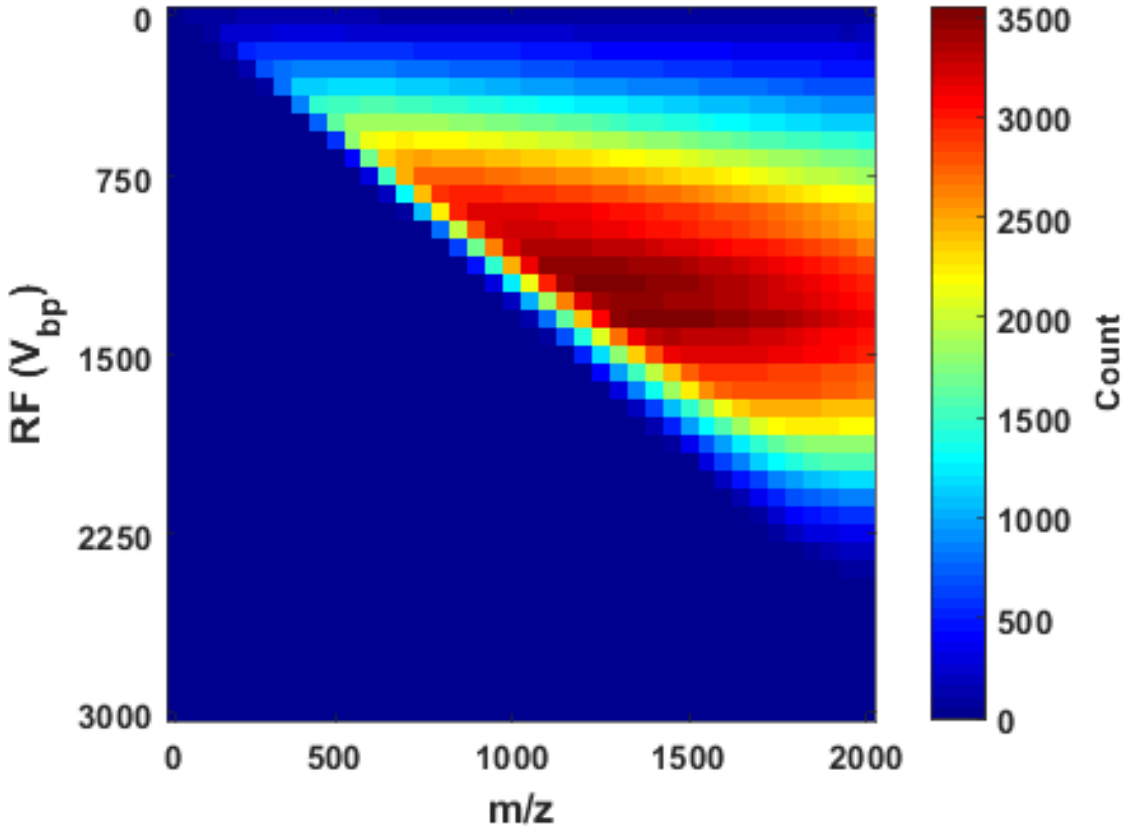

Figure B.1. Image of total solutions found at various *m/z* and RF amplitudes.

Table B.4. Monte Carlo bounds for SMC Components in the “digital quadrupole” experiments

Component	Parameter	Min	Max
Entrance Lens	DC	-50 V	50 V
Digital Quad	Resolve DC	0 V	0 V
	Offset DC	0 V	0 V
	RF Amp	50 V_{b-p}	2000 V_{b-p}
	Duty Cycle	0 %	100 %
	Freq	400 kHz	400 kHz
Exit Lens	DC	-50 V	50 V

Table B.5. Ion optic geometries for the “arbitrary geometry” experiment

Component	Parameter	Value(s)		
Entrance Lens	Position	40 mm_x	40 mm_y	40 mm_z
	Rotation	0 °x	0 °y	0 °z
	Thickness	2.67 mm		
	Inside Radius	7 mm		
	Outside Radius	20 mm		
Stacked Ring Guide	Position	40 mm_x	40 mm_y	64 mm_z
	Rotation	0 °x	0 °y	0 °z
	Ring Inner Radius	10 mm		
	Rod Outer Radius	20 mm		
	Ring Thickness	3 mm		
	Ring Spacing	2 mm		
	Number of Ring Sets	12		
Deflection Plate 1	Position	20 mm_x	40 mm_y	200 mm_z
	Rotation	0 °x	0 °y	0 °z
	Length	2 mm		
	Width	34 mm		
	Depth	30 mm		
Deflection Plate 2	Position	60 mm_x	40 mm_y	200 mm_z
	Rotation	0 °x	0 °y	0 °z
	Length	2 mm		
	Width	34 mm		
	Depth	30 mm		

Component	Parameter	Value(s)					
Deflection Plate 3	Position	40	mm_x	20	mm_y	200	mm_z
	Rotation	0	°x	0	°y	0	°z
	Length	34	mm				
	Width	2	mm				
	Depth	30	mm				
Deflection Plate 4	Position	40	mm_x	60	mm_y	200	mm_z
	Rotation	0	°x	0	°y	0	°z
	Length	34	mm				
	Width	2	mm				
	Depth	30	mm				
Target Lens	Position	100	mm_x	40	mm_y	300	mm_z
	Rotation	45	°x	0	°y	0	°z
	Thickness	2.67	mm				
	Inside Radius	7	mm				
	Outside Radius	20	mm				

Table B.6. SMC Parameters used in the “arbitrary geometry” experiments

SMC Parameter	Value
mz_start	100 *m/z*
mz_end	2000 *m/z*
mz_interval	100 *m/z*
mz_interval_ion_count	10
max_failures_for_step	20
max_failures_for_reset	200
max_ion_flight_time	500 µs
trajectory_quality	-1

Table B.7. Monte Carlo bounds for SMC Components in the “arbitrary geometry” experiments

Component	Parameter	Min	Max
Entrance Lens	DC	-500 V	500 V
Stacked Ring Guide	DC (1)	-300 V	300 V
	DC (2)	-300 V	300 V
Deflection Plate 1	DC	-300 V	300 V
Deflection Plate 2	DC	-300 V	300 V
Deflection Plate 3	DC	-300 V	300 V
Deflection Plate 4	DC	-300 V	300 V
Target Lens	DC	-500 V	500 V

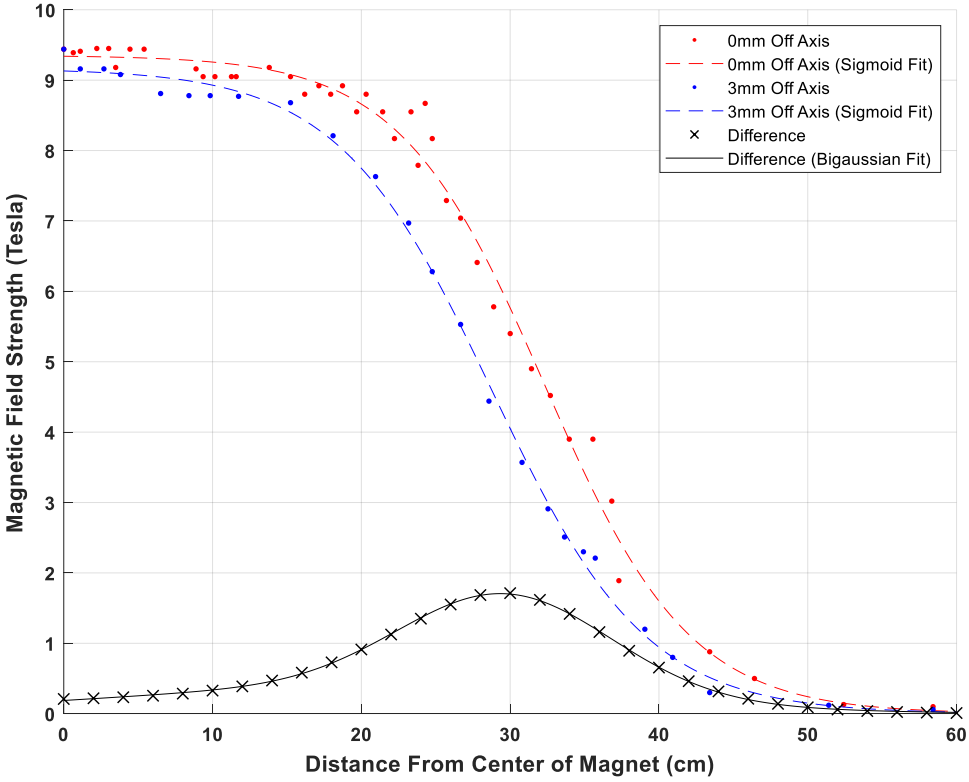

Figure B.2. Fitted experimentally collected magnetic field strength measurements for 0 (red) and 3 (blue) mm off axis of the magnetic field center.

Table B.8. Ion optic geometries for the “imaging system” experiments

Component	Parameter	Value(s)		
Stage	Position	40 mm_x	40 mm_y	10 mm_z
	Rotation	0 °x	0 °y	-45 °z
	Thickness	1 mm		
	Inside Radius	.01 mm		
	Outside Radius	16 mm		
Lens 1	Position	40 mm_x	40 mm_y	58.84 mm_z
	Rotation	0 °x	0 °y	0 °z
	Thickness	1.6 mm		
	Inside Radius	10 mm		
	Outside Radius	30 mm		
Lens 2	Position	40 mm_x	40 mm_y	64.51 mm_z
	Rotation	0 °x	0 °y	0 °z
	Thickness	1.6 mm		
	Inside Radius	10 mm		
	Outside Radius	30 mm		
Lens 3	Position	40 mm_x	40 mm_y	70.18 mm_z
	Rotation	0 °x	0 °y	0 °z
	Thickness	1.6 mm		
	Inside Radius	10 mm		
	Outside Radius	30 mm		
Quad 1	Position	40 mm_x	40 mm_y	98.01 mm_z
	Rotation	0 °x	0 °y	0 °z
	Length	43 mm		
	Rod Radius	3.175 mm		
	Inscribed Radius	2.764 mm		

Component	Parameter	Value(s)		
Trap Entrance Lens	Position	40 mm_x	40 mm_y	123.31 mm_z
	Rotation	0 °x	0 °y	0 °z
	Thickness	1.6 mm		
	Inside Radius	2 mm		
	Outside Radius	30 mm		
Quad 2	Position	40 mm_x	40 mm_y	192.61 mm_z
	Rotation	0 °x	0 °y	0 °z
	Length	131 mm		
	Rod Radius	3.175 mm		
	Inscribed Radius	2.764 mm		
Trap Exit Lens	Position	40 mm_x	40 mm_y	262.04 mm_z
	Rotation	0 °x	0 °y	0 °z
	Thickness	1.6 mm		
	Inside Radius	2 mm		
	Outside Radius	30 mm		
Quad 3	Position	40 mm_x	40 mm_y	287.34 mm_z
	Rotation	0 °x	0 °y	0 °z
	Length	43 mm		
	Rod Radius	3.175 mm		
	Inscribed Radius	2.764 mm		
Quad 4 Entrance Lens	Position	40 mm_x	40 mm_y	314.64 mm_z
	Rotation	0 °x	0 °y	0 °z
	Thickness	1.6 mm		
	Inside Radius	2 mm		
	Outside Radius	23.85 mm		

Component	Parameter	Value(s)					
Quad 4	Position	40	mm_x	40	mm_y	917.34	mm_z
	Rotation	0	°x	0	°y	0	°z
	Length	1193.8	mm				
	Rod Radius	3.175	mm				
	Inscribed Radius	2.764	mm				
ICR Quad Trap Plate	Position	40	mm_x	40	mm_y	1515.74	mm_z
	Rotation	0	°x	0	°y	0	°z
	Thickness	1	mm				
	Inside Radius	2.3	mm				
	Outside Radius	23.85	mm				

Table B.9. SMC Parameters used in the “imaging system” experiments

SMC Parameter	Value
mz_start	50 *m/z*
mz_end	2000 *m/z*
mz_interval	50 *m/z*
mz_interval_ion_count	10
max_failures_for_step	10
max_failures_for_reset	1000
max_ion_flight_time	1000 µs
trajectory_quality	-1

Table B.10. Monte Carlo bounds for SMC Components in the "imaging system" experiments

Component	Parameter	Min	Max
Stage	DC	-200 V	200 V
Lens 1	DC	-300 V	300 V
Lens 2	DC	-300 V	300 V
Lens 3	DC	-300 V	300 V
Trap Entrance Lens	DC	-300 V	300 V
Trap Exit Lens	DC	-300 V	300 V
Q4 Entrance Lens	DC	-300 V	300 V
ICR Quad Trap	DC	-50 V	50 V
Quad 1	RF Amp	50 $V_{b\text{-}p}$	1000 $V_{b\text{-}p}$
	Freq	1.0 MHz	2.0 MHz
	DC Offset	-200 V	200 V
	DC Resolving	0 V	0 V
Quad 2	RF Amp	50 $V_{b\text{-}p}$	1000 $V_{b\text{-}p}$
	Freq	1.0 MHz	2.0 MHz
	DC Offset	-200 V	200 V
	DC Resolving	0 V	0 V
Quad 3	RF Amp	50 $V_{b\text{-}p}$	1000 $V_{b\text{-}p}$
	Freq	1.0 MHz	2.0 MHz
	DC Offset	-200 V	200 V
	DC Resolving	0 V	0 V
Quad 4	RF Amp	50 $V_{b\text{-}p}$	1000 $V_{b\text{-}p}$
	Freq	1.0 MHz	2.0 MHz
	DC Offset	-200 V	200 V
	DC Resolving	0 V	0 V

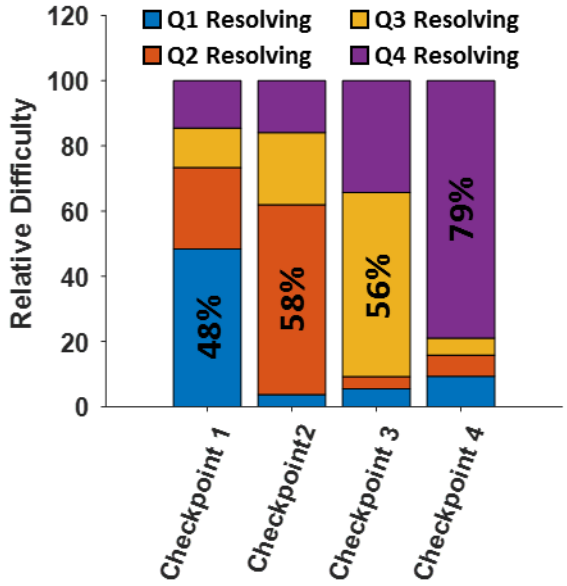

Figure B.3. Stacked bar plots of relative difficulty values for modified SMC settings in which all resolving DC parameters were set to ±0 V except for either Q1 (blue), Q2 (orange), Q3 (yellow), or Q4 (purple) which was set to ±500 V.

APPENDIX C

Supplementary Information for Chapter Four: *Data Station One: An Open Source, Modular Control Platform for Custom Imaging Mass Spectrometers*

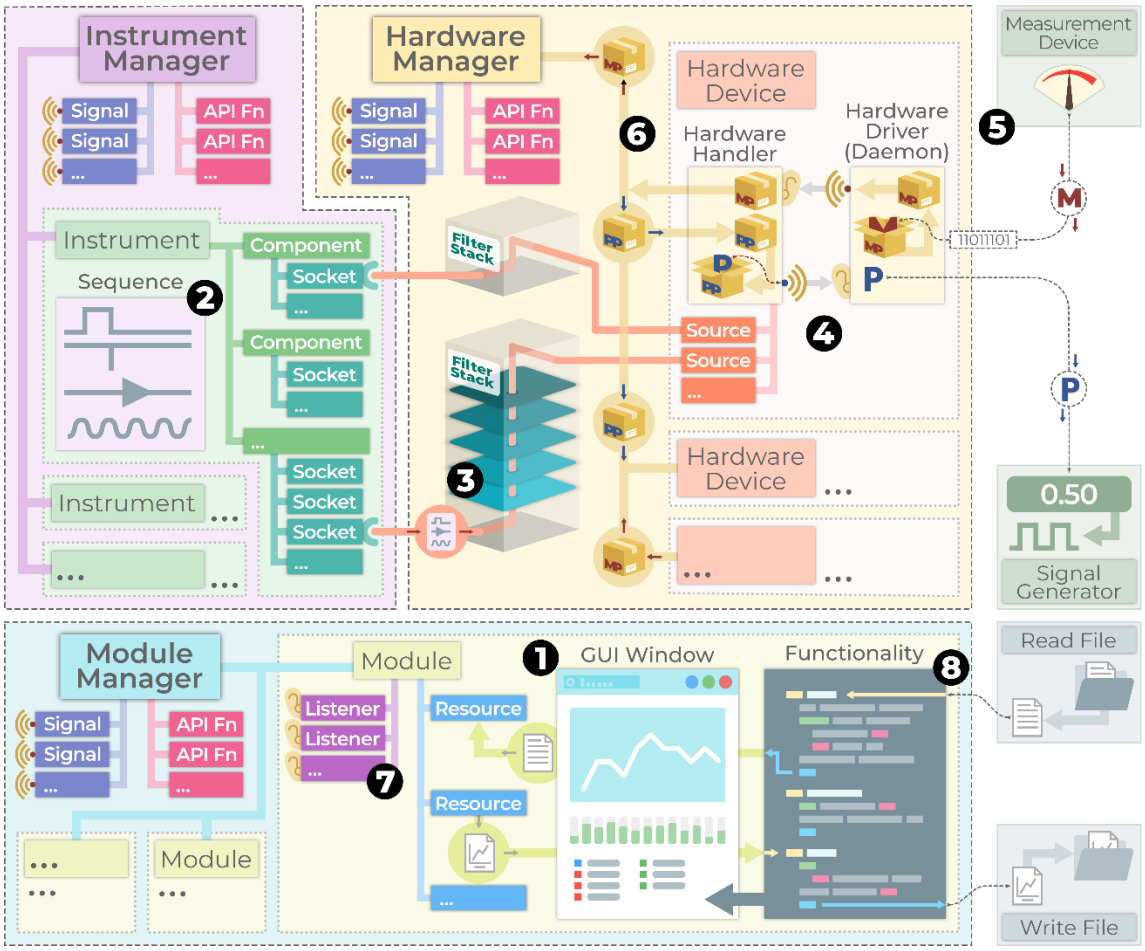

Appendix Scheme C.1. displays the "core" of DSO in much the same manner as Scheme 1 in the main text. However, eight black dots with numbers 1–8 have been added to the scheme to demonstrate how information flows through DSO.

The black-circled numbers (1–8) indicate the path that information might flow through DSO from user input to a Measurement Device to a Write File and a GUI Window. For the example experiment outlined below, a user clicks a button in a GUI Window, a

pulse valve allows injection of a gas into an FT-ICR vacuum chamber, the gas is ionized, the ions are trapped, a delay occurs to allow the pressure to return to a lower state, the FT-ICR cell excites the ions using a "chirp" excitation, the complex waveform of the ions is recorded, the data is Fourier transformed, the transformed data is stored in a Write File, and the transformed data is plotted in the original GUI Window.

In Step 1, a user clicks a button in a Module's GUI Window that has been linked to a portion of the Module's Functionality. The Functionality calls the Instrument Manager through an API Function and requests a list of the available Instruments. As directed through the API Function, the Instrument Manager queries the various Instruments and, as the FT-ICR Instrument is not currently occupied with running a Sequence and is not experiencing any errors, the Instrument Manager emits a Signal of all the available Instruments (and their Components) including the FT-ICR Instrument. The Module has a connected Listener to the Signal that the Instrument Manager emits, and the Module uses the Signal-emitted list of available Instruments and Components to then send a Sequence to the FT-ICR Instrument.

In Step 2, the Sequence contains a set of temporal events (e.g., an excitation waveform, an excitation trigger time, a detection trigger time, a DC voltage and time to apply the voltage to the trapping plates, a set of pulse valve timings (high and low), etc.) that apply to each of the FT-ICR Instrument's Components (in this case, a pulse valve, a set of electrically-connected trapping rings, a set of electrically-connected trapping plates, an electron ionization source, a set of excitation plates, a set of detection plates, and two independent triggers (one for excitation initiation and one for detection initiation)). The Sequence information is relayed to the relevant Components and executed by the respective

Components (the Instrument also alerts the Instrument Manager to emit a Signal that the Sequence has begun — and the FT-ICR Instrument will send a subsequent Signal when the Sequence completes).

In Step 3, the Components that have knowledge of how to execute the appropriate events in the Sequence, translate and send the events through their Sockets. In the example case of the pulse valve, the pulse valve Component sends a DC voltage "high" event through the Socket-Source connection and then subsequently sends a DC voltage "low" event (thus requesting the voltage needed to open and then close the pulse valve). Any applicable Filters will modify the event for suitability of the respective Sources (for instance, increasing the voltage to a needed level). In the example case of the FT-ICR excitation, there are two Components that are required. The first is a trigger Component that will arm a hardware (i.e., physical not software) trigger to execute at a certain time. The second is an excitation plate Component that contains a desired waveform for a waveform generator to apply to the physical excitation plate. When the hardware trigger's execution time occurs, the hardware trigger will initiate the application of the waveform on the physical excitation plate.

In Step 4, the Sources of the various Hardware Devices (e.g., waveform generators, DC voltage sources, differential amplification detectors, etc.) that can supply the necessary effects requested by the connected Components in turn request the effects using the corresponding Hardware Handlers. The Hardware Handlers processes these requested effects and emit them as Programming Information Signals. The Hardware Driver's Listener receives these emitted Signals and (after encoding or translating them as needed) programs the appropriate physical hardware Signal Generators using the specific digital

instructions. For example, the Hardware Driver is what performs the programming (mentioned in Step 3) of the waveform to the physical waveform Signal Generator and the timing trigger to the hardware trigger Signal Generator.

In Step 5, any Measurement Devices that were programmed (for the FT-ICR example, a differential amplifier is programmed to begin data collection at the end of the, previously mentioned, excitation waveform) receive measurement signals (usually voltages) and translate these measurement signals into digital (the binary nature of the digital signal is indicated by the 1's and 0's in the dotted-line bubble in Scheme 1) Measurements that are sent to their respective Hardware Drivers. The Measurements are received by the corresponding Hardware Drivers and any decoding or simple signal processing (e.g., waiting for 20 Measurements to be received before averaging them, performing a truncation of trailing bits, "chunking" the data, etc.) is performed. The Hardware Driver packages the Measurement into a Measurement Package and emits the Measurement Package through the Hardware Driver's Signal emitter.

In Step 6, the Hardware Handlers receives the Measurement Packet Signals using the paired, private Listeners. The Hardware Handlers forward the Measurement Packets to the Hardware Manager that then emits Signals indicating that new Measurement Packets have been received and processed by the Hardware Devices.

In Step 7, a Listener of a Module receives a new Hardware Manager Signal that contains a Measurement Packet from a differential amplifier Hardware Device. The Lister instructs the Module that such a Signal has been received and the Module uses the API Function of the Hardware Manager to retrieve a reference to the Measurement Packet. The

Module creates a Resource containing the Measurement data from the Measurement Packet.

In Step 8, the Functionality of the Module observes that a Resource has been created or changed, and the Functionality extracts the Measurement data from the Resource. The Functionality then applies any data processing that is wanted (in the case of the FT-ICR Instrument, a Fourier transform is applied to the Measurement data as well as the ICR equation to convert from frequency to mass-to-charge information). The data that is processed is then supplied to the GUI Window for plotting and is encoded and written to a Write File.

Code C.1. Example user script for a DC Electrode Component

```
from src.Managers.InstrumentManager.Component import *
from src.Managers.InstrumentManager.EventTypes import *
from src.Managers.InstrumentManager.Sockets import *
from src.Managers.HardwareManager.PacketCommands import *
from PyQt5.Qt import *
from PyQt5.QtGui import *
import os, random, numpy as np
from decimal import Decimal
from scipy import signal

class DC_Electrode(Component):
    componentType = 'DC Electrode'
    componentIdentifier = 'DCElec_MRB'
    componentVersion = '1.0'
    componentCreator = 'Matthew R. Brantley'
    componentVersionDate = '7/13/2018'
    iconGraphicSrc = 'default.png' #Not adjustable like layoutGraphicSrc
    valid = False

    def onCreation(self):
        self.compSettings['layoutGraphicSrc'] = self.iconGraphicSrc
        self.compSettings['vMin'] = 0.0
        self.compSettings['vMax'] = 10.0
        self.compSettings['granularity'] = 0.0001
        self.containerWidget = self.configWidgetContent()
        self.socket = self.addAOSocket(self.compSettings['name'])
        self.addEventType(stepEvent)
        self.addEventType(pulseEvent)
        self.addEventType(pulseTrainEvent)
        self.addEventType(linearRampEvent)
        self.addEventType(sawWave)

    def onProgram(self):
        self.packet = commandPacket()
        v0 = 0
        for event in self.eventList:
            command = event.toCommand(v0)
            self.packet.Add_Command(command)
            v0 = command.pairs[-1,1]
        self.socket.Set_Programming_Packet(self.packet)

    def updateConfigContent(self):
        self.showSequenceBox.setChecked(self.compSettings['showSequencer'])
        self.nameBox.setText(self.compSettings['name'])
        self.minVBox.setValue(self.compSettings['vMin'])
        self.maxVBox.setValue(self.compSettings['vMax'])

    def configWidgetContent(self):
        self.container = QWidget()
        self.fbox = QFormLayout()
```

```
        self.showSequenceBox = QCheckBox()
        self.showSequenceBox.setChecked(True)
        self.showSequenceBox.stateChanged.connect(self.saveWidgetValues)
        self.fbox.addRow("Draw Sequence:", self.showSequenceBox)

        self.nameBox = QLineEdit(self.compSettings['name'])
        self.nameBox.textChanged.connect(self.saveWidgetValues)
        self.fbox.addRow("Name:", self.nameBox)

        self.minVBox = QDoubleSpinBox()
        self.minVBox.setRange(-5000, 5000)
        self.minVBox.setValue(self.compSettings['vMin'])
        self.minVBox.valueChanged.connect(self.saveWidgetValues)
        self.fbox.addRow("Min (V):", self.minVBox)

        self.maxVBox = QDoubleSpinBox()
        self.maxVBox.setRange(-5000, 5000)
        self.maxVBox.setValue(self.compSettings['vMax'])
        self.maxVBox.valueChanged.connect(self.saveWidgetValues)
        self.fbox.addRow("Max (V):", self.maxVBox)

        self.container.setLayout(self.fbox)
        return self.container

    def saveWidgetValues(self):
        self.compSettings['showSequencer'] = self.showSequenceBox.isChecked()
        self.compSettings['name'] = self.nameBox.text()
        self.compSettings['vMin'] = self.minVBox.value()
        self.compSettings['vMax'] = self.maxVBox.value()
        self.socket.name = self.compSettings['name']
        self.checkValidity()
        self.Component_Modified.emit(self)


class stepEvent(eventType):
    name = 'Step'

    def __init__(self):
        super().__init__()
        self.Add_Parameter(eventParameterDouble('Voltage'))

    def getLength(self):
        return 0

    def toCommand(self, v0):
        pairs = np.array([[self.time, v0], [self.time,
self.eventParams['Voltage'].v()]])
        command = AnalogSparseCommand(pairs)
        return command


class pulseEvent(eventType):
    name = 'Pulse'
    def __init__(self):
        super().__init__()
```

```
        self.Add_Parameter(eventParameterDouble('Voltage'))
        self.Add_Parameter(eventParameterDouble(
        'Duration', allowZero=False, allowNegative=False)
        )

    def getLength(self):
        return self.eventParams['Duration'].v()

    def toCommand(self, v0):
        pairs = np.array([[self.time, v0],
        [self.time, self.eventParams['Voltage'].v()],
        [self.time + self.eventParams['Duration'].v(),
        self.eventParams['Voltage'].v()],
        [self.time + self.eventParams['Duration'].v(), v0]])
        command = AnalogSparseCommand(pairs)
        return command


class linearRampEvent(eventType):
    name = 'Linear Ramp'

    def __init__(self):
        super().__init__()
        self.Add_Parameter(eventParameterDouble('Voltage'))
        self.Add_Parameter(eventParameterDouble('Duration', allowZero=False))

    def getLength(self):
        return self.eventParams['Duration'].v()

    def toCommand(self, v0):
        pairs = np.array([[self.time, v0],
        [self.time + self.eventParams['Duration'].v(),
self.eventParams['Voltage'].v()]])
        command = AnalogSparseCommand(pairs)
        return command


class pulseTrainEvent(eventType):
    name = 'Pulse Train'

    def __init__(self):
        super().__init__()
        self.Add_Parameter(eventParameterDouble('Voltage'))
        self.Add_Parameter(eventParameterInt('Count',
            allowZero=False, allowNegative=False))
        self.Add_Parameter(eventParameterDouble('onDuration',
            allowZero=False, allowNegative=False))
        self.Add_Parameter(eventParameterDouble('offDuration',
            allowZero=False, allowNegative=False))

    def getLength(self):
        return (self.eventParams['onDuration'] * self.eventParams['Count'])
            + (self.eventParams['offDuration'] *(self.eventParams['Count']-1))

    def toCommand(self, v0):
```

```
        pairs = None
        for n in range(0, self.eventParams['Count'].v()):
            offset = n * (self.eventParams['offDuration'].v() +
                self.eventParams['onDuration'].v())
            newEventStep = np.array([[self.time + offset,
                self.eventParams['Voltage'].v()],
            [self.time + offset + self.eventParams['onDuration'].v(), v0]])
            if(pairs is None):
                pairs = newEventStep
            else:
                pairs = np.vstack((pairs, newEventStep))

        print(pairs.shape)
        command = AnalogSparseCommand(pairs)
        return command


class sawWave(eventType):
    name = 'Sawtooth Wave'

    def __init__(self):
        super().__init__()
        self.Add_Parameter(eventParameterInt('Count',
            allowZero=False, allowNegative=False))
        self.Add_Parameter(eventParameterDouble('Amplitude (V)',
            allowZero=False, allowNegative=False))
        self.Add_Parameter(eventParameterDouble('Cycle Length (ms)',
            allowZero=False, allowNegative=False))
        self.Add_Parameter(eventParameterInt('Sample Rate',
            allowZero=False, allowNegative=False))

    def getLength(self):
        return (self.eventParams['Count'].v() *
            self.eventParams['Cycle Length (ms)'].v() / 1000)

    def toCommand(self, v0):
        f = 1/(self.eventParams['Cycle Length (ms)'].v() / 1000)
        length = self.getLength()
        rate = self.eventParams['Sample Rate'].v()

        t = np.linspace(self.time, self.time + length, rate)
        s = signal.sawtooth(2 * np.pi * f * t) *
            self.eventParams['Amplitude (V)'].v()

        pairs = np.transpose(np.vstack((t, s)))
        command = AnalogSparseCommand(pairs)
        return command
```

Code C.2. Example user script for a PXIe 5451 Waveform Generator Hardware Device

```
from src.Managers.HardwareManager.HardwareDevice import HardwareDevice
import nifgen, time, numpy as np
from src.Managers.HardwareManager.PacketCommands import *

ms = lambda: int(round(time.time() * 1000))


class PXIe_5451(HardwareDevice):
    hardwareType = 'NI PXIe-5451'
    hardwareIdentifier = 'MRB_PXIe5451'
    hardwareVersion = '1.0'
    hardwareCreator = 'Matthew R. Brantley'
    hardwareVersionDate = '8/20/2018'

##################################################################
##################MANDATORY FUNCS ################################

    def scan(self):
        for device in self.systemDeviceInfo['NI-FGEN']:
            if(device['Device Model'] == 'NI PXIe-5451'):
                self.Add_Device(device['Device Name'])
        self.scanned.emit()

    def initialize(self, deviceName, triggerMode):
        try:
            if(deviceName != ''):
                self.session = None
                self.wfm_handles = list()
                self.reportTime = ms()
                with nifgen.Session(deviceName) as session:
                    self.maxRate = session.arb_sample_rate
                    self.source0 = self.Add_AOSource('0', -1, 1, 0.1)
                    self.source1 = self.Add_AOSource('1', -1, 1, 0.1)

                self.session = nifgen.Session(deviceName)
        except:
            pass
        self.initialized.emit()

    def configure(self):
        self.session.terminal_configuration =
            nifgen.TerminalConfiguration.SINGLE_ENDED
        self.session.analog_path = nifgen.AnalogPath.DIRECT
        self.configured.emit()

    def program(self, programmingPackets):
        self.Set_Ready_Status(False)
        if(programmingPackets):
            self.session.abort()
            self.session.clear_arb_memory()
            self.wfm_handles = list()
```

```
            t0, f, wave = self.parsePacket(programmingPackets)
            if t0 is not None:
                self.session.output_mode = nifgen.OutputMode.ARB
                self.session.arb_sample_rate = f
                self.session.channels[0].wait_value = 0
                self.session.wait_behavior = nifgen.WaitBehavior.JUMP_TO

                self.wfm = self.session.channels[0].create_waveform(wave)
                self.session.trigger_mode = nifgen.TriggerMode.SINGLE
                self.session.start_trigger_type =
                    nifgen.StartTriggerType.DIGITAL_EDGE
                self.session.digital_edge_start_trigger_source = 'PFI0'
                self.session.channels[0].configure_arb_waveform(
                    self.wfm, 1, 0.0
                )

        self.Set_Ready_Status(True)
        self.programmed.emit()

    def softTrigger(self):
        self.Set_Ready_Status(False)
        if self.session.is_done():
            self.session.abort()
            self.session.initiate()
            self.softTriggered.emit()

    def shutdown(self):
        if(self.session is not None):
            self.session.close()

    def idle(self):
        if(hasattr(self, 'session')):
            if(self.session is not None):
                try:
                    if(self.session.is_done() is False):
                        if(ms() - self.reportTime >= 500):
                            self.Send_Status_Message(
                                'Armed! Waiting for trigger...'
                            )
                            self.reportTime = ms()
                    else:
                        if(self.Ready_Status() is False):
                            self.Send_Status_Message('Triggered!')
                            self.Set_Ready_Status(True)
                except:
                    pass

    def stop(self):
        self.Send_Status_Message('Sending Stop Command...')
        if(hasattr(self, 'session')):
            if(self.session is not None):
                try:
                    self.session.abort()
                except:
                    pass
```

```
#########################################################
################## INTERNAL HELPER FUNCS #############

    def parsePacket(self, packet):
        fst = packet[0]
        cmd = fst['programmingPacket']
                  .Get_Commands(commandType=AnalogWaveformCommand)
        if cmd:
            cmd = cmd[0]
            if(cmd.wave.shape[0] % 2 == 0):
                return cmd.t0, cmd.f, cmd.wave
            else:
                return cmd.t0, cmd.f, cmd.wave[:-1]
        else:
            return None, None, None
```

Code C.3. Example user script of a log-linear Filter used for a 275i vacuum gauge

```
from src.Managers.HardwareManager.Filter import *
from src.Managers.InstrumentManager.Sockets import *
from PyQt5.Qt import *
from PyQt5.QtGui import *
import numpy as np


class User_Filter(AnalogFilter):
    filterType = '275i Log-Linear Output'
    filterIdentifier = '275iLL_MRB'
    filterVersion = '1.0'
    filterCreator = 'Matthew R. Brantley'
    filterVersionDate = '6/26/2019'
    iconGraphicSrc = 'default.png'
    numPaths = 1
    valid = False

    def onCreation(self):
        self.filterSettings['name'] = 'Unnamed ' + self.filterType
        self.checkValidity()

    def checkValidity(self):
        self.valid = True

    def procForward(self, programmingPacket):
        return programmingPacket

    def procReverse(self, measurementPacket):
        measurementPacket.getMeasurements()[0].wave = np.power(
            10, measurementPacket.getMeasurements()[0].wave - 5
        )
        return measurementPacket
```

Code C.4. Example user script of a Python Console module

```
from PyQt5.Qt import *
import os, time
from pyqode.core import api, modes, panels
from src.Managers.ModuleManager.DSModule import DSModule
from src.Constants import moduleFlags as mfs
from code import InteractiveConsole
from imp import new_module
from qtconsole.rich_ipython_widget import RichIPythonWidget
from qtconsole.inprocess import QtInProcessKernelManager


class Console(DSModule):
    Module_Name = 'Interactive Console'
    Module_Flags = [mfs.CAN_DELETE]
    ITEM_GUID = Qt.UserRole

    def __init__(self, ds, handler):
        super().__init__(ds, handler)
        self.ds = ds

    def configureWidget(self, window):
        self.window = window
        self.interactiveConsole = DSConsole(self.ds)
        self.consoleWidget = ConsoleContainer(self.ds)
        self.setWidget(self.consoleWidget)


class ConsoleContainer(QWidget):
    def __init__(self, ds):
        super().__init__()
        self.ds = ds
        self.layout = QVBoxLayout()
        self.layout.setSpacing(0)
        self.layout.setContentsMargins(0,0,0,0)
        self.setLayout(self.layout)
        self.consoleMainWidget = QWidget()
        self.put_ipy(self.consoleMainWidget)
        self.layout.addWidget(self.consoleMainWidget)

    def put_ipy(self, parent):
        kernel_manager = QtInProcessKernelManager()
        kernel_manager.start_kernel()
        self.kernel = kernel_manager.kernel
        self.kernel.gui = 'qt4'
        kernel_client = kernel_manager.client()
        kernel_client.start_channels()
        kernel_client.namespace  = parent

        def stop():
            kernel_client.stop_channels()
            kernel_manager.shutdown_kernel()
```

```
        layout = QVBoxLayout(parent)
        layout.setSpacing(0)
        layout.setContentsMargins(0,0,0,0)
        widget = RichIPythonWidget(parent=parent)
        layout.addWidget(widget)
        widget.kernel_manager = kernel_manager
        widget.kernel_client = kernel_client
        widget.exit_requested.connect(stop)
        ipython_widget = widget
        ipython_widget.show()
        ns = dict()
        ns['DataStation'] = self.ds
        ns['ds'] = self.ds
        ns['Hardware_Manager'] = self.ds.hM
        ns['hM'] = self.ds.hM
        ns['Instrument_Manager'] = self.ds.iM
        ns['iM'] = self.ds.iM
        ns['Module_Manager'] = self.ds.mM
        ns['mM'] = self.ds.mM
        ns['Workspace_Manager'] = self.ds.wM
        ns['wM'] = self.ds.wM
        self.kernel.shell.push(ns)
        return


class DSConsole(InteractiveConsole):
    def __init__(self, ds, names=None):
        names = names or 89
        names['console'] = self
        names['DataStation'] = ds
        names['datastation'] = ds
        names['ds'] = ds
        super().__init__(names)
        self.superspace = new_module('superspace')

    def runCodeSegment(self, code):
        code = self.preprocess(code)
        self.runcode(code)
        print()

    @staticmethod
    def preprocess(code):
        return code
```

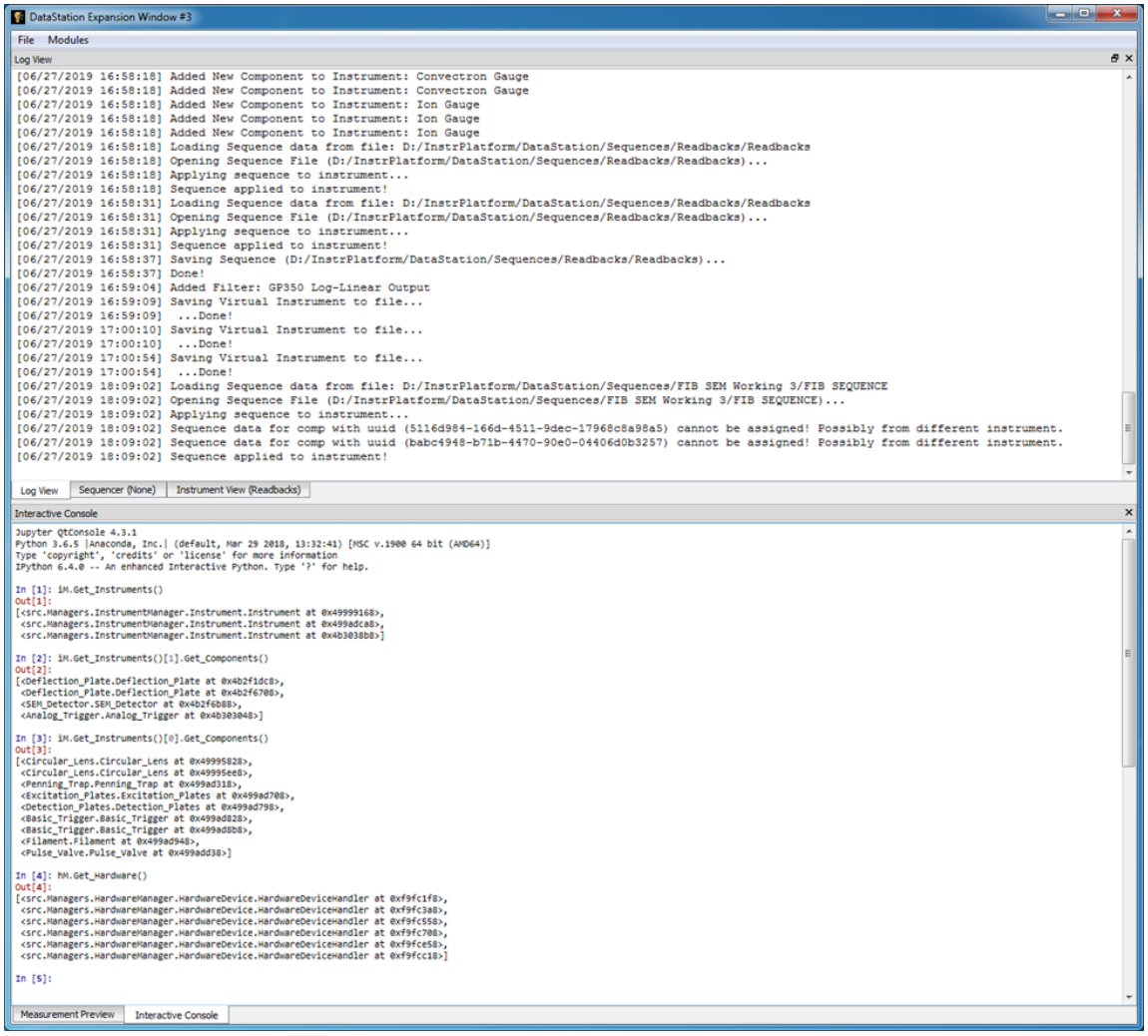

Appendix Figure C.1. displays a data log (top half) and an interactive Python console (bottom half) Module. The interactive Python console Module is generated from the same code as is shown in Appendix B.5 and depicts inspection of the internal state of various components and instruments of DSO during runtime.

BIBLIOGRAPHY

1. Watson, J. T.; Sparkman, O. D., Introduction to mass spectrometry: instrumentation, applications, and strategies for data interpretation. **2007**.

2. De Hoffmann, E., Mass spectrometry. *Kirk-Othmer Encyclopedia of Chemical Technology* **2000**.

3. Richardson, S. D., Environmental mass spectrometry: emerging contaminants and current issues. *Analytical Chemistry* **2011,** *84* (2), 747-778.

4. Richardson, S. D.; Kimura, S. Y., Emerging environmental contaminants: Challenges facing our next generation and potential engineering solutions. *Environmental Technology & Innovation* **2017,** *8*, 40-56.

5. Petrović, M.; Hernando, M. D.; Díaz-Cruz, M. S.; Barceló, D., Liquid chromatography–tandem mass spectrometry for the analysis of pharmaceutical residues in environmental samples: a review. *Journal of Chromatography A* **2005,** *1067* (1-2), 1-14.

6. Lindinger, W.; Hansel, A.; Jordan, A., On-line monitoring of volatile organic compounds at pptv levels by means of proton-transfer-reaction mass spectrometry (PTR-MS) medical applications, food control and environmental research. *International Journal of Mass Spectrometry and Ion Processes* **1998,** *173* (3), 191-241.

7. Chai, M.; Pawliszyn, J., Analysis of environmental air samples by solid-phase microextraction and gas chromatography/ion trap mass spectrometry. *Environmental science & technology* **1995,** *29* (3), 693-701.

8. Picó, Y.; Blasco, C.; Font, G., Environmental and food applications of LC–tandem mass spectrometry in pesticide-residue analysis: An overview. *Mass spectrometry reviews* **2004,** *23* (1), 45-85.

9. Rosén, J.; Hellenäs, K.-E., Analysis of acrylamide in cooked foods by liquid chromatography tandem mass spectrometry. *Analyst* **2002,** *127* (7), 880-882.

10. Zöllner, P.; Mayer-Helm, B., Trace mycotoxin analysis in complex biological and food matrices by liquid chromatography–atmospheric pressure ionisation mass spectrometry. *Journal of Chromatography A* **2006,** *1136* (2), 123-169.

11. Lacorte, S.; Fernandez-Alba, A. R., Time of flight mass spectrometry applied to the liquid chromatographic analysis of pesticides in water and food. *Mass spectrometry reviews* **2006,** *25* (6), 866-880.

12. Careri, M.; Bianchi, F.; Corradini, C., Recent advances in the application of mass spectrometry in food-related analysis. *Journal of Chromatography A* **2002,** *970* (1-2), 3-64.

13. Ejsing, C. S.; Sampaio, J. L.; Surendranath, V.; Duchoslav, E.; Ekroos, K.; Klemm, R. W.; Simons, K.; Shevchenko, A., Global analysis of the yeast lipidome by quantitative shotgun mass spectrometry. *Proceedings of the National Academy of Sciences* **2009,** *106* (7), 2136-2141.

14. Soga, T.; Ohashi, Y.; Ueno, Y.; Naraoka, H.; Tomita, M.; Nishioka, T., Quantitative metabolome analysis using capillary electrophoresis mass spectrometry. *Journal of proteome research* **2003,** *2* (5), 488-494.

15. Hirayama, A.; Kami, K.; Sugimoto, M.; Sugawara, M.; Toki, N.; Onozuka, H.; Kinoshita, T.; Saito, N.; Ochiai, A.; Tomita, M., Quantitative metabolome profiling of colon and stomach cancer microenvironment by capillary electrophoresis time-of-flight mass spectrometry. *Cancer research* **2009,** *69* (11), 4918-4925.

16. Ehrich, M.; Nelson, M. R.; Stanssens, P.; Zabeau, M.; Liloglou, T.; Xinarianos, G.; Cantor, C. R.; Field, J. K.; van den Boom, D., Quantitative high-throughput analysis of DNA methylation patterns by base-specific cleavage and mass spectrometry. *Proceedings of the National Academy of Sciences* **2005,** *102* (44), 15785-15790.

17. Park, S. K.; Venable, J. D.; Xu, T.; Yates III, J. R., A quantitative analysis software tool for mass spectrometry–based proteomics. *Nature methods* **2008,** *5* (4), 319.

18. Bantscheff, M.; Schirle, M.; Sweetman, G.; Rick, J.; Kuster, B., Quantitative mass spectrometry in proteomics: a critical review. *Analytical and bioanalytical chemistry* **2007,** *389* (4), 1017-1031.

19. Dong, M.-Q.; Venable, J. D.; Au, N.; Xu, T.; Park, S. K.; Cociorva, D.; Johnson, J. R.; Dillin, A.; Yates, J. R., Quantitative mass spectrometry identifies insulin signaling targets in C. elegans. *Science* **2007,** *317* (5838), 660-663.

20. Perkins, D. N.; Pappin, D. J.; Creasy, D. M.; Cottrell, J. S., Probability-based protein identification by searching sequence databases using mass spectrometry data. *ELECTROPHORESIS: An International Journal* **1999,** *20* (18), 3551-3567.

21. Shevchenko, A.; Wilm, M.; Vorm, O.; Mann, M., Mass spectrometric sequencing of proteins from silver-stained polyacrylamide gels. *Analytical chemistry* **1996,** *68* (5), 850-858.

22. Zaia, J., Mass spectrometry of oligosaccharides. *Mass spectrometry reviews* **2004,** *23* (3), 161-227.

23. Mechref, Y.; Novotny, M. V.; Krishnan, C., Structural characterization of oligosaccharides using MALDI-TOF/TOF tandem mass spectrometry. *Analytical chemistry* **2003,** *75* (18), 4895-4903.

24. Murray, K. K., DNA sequencing by mass spectrometry. *Journal of Mass Spectrometry* **1996,** *31* (11), 1203-1215.

25. Köster, H.; Tang, K.; Fu, D.-J.; Braun, A.; Van Den Boom, D.; Smith, C. L.; Cotter, R. J.; Cantor, C. R., A strategy for rapid and efficient DNA sequencing by mass spectrometry. *Nature biotechnology* **1996,** *14* (9), 1123.

26. Benninghoven, A.; Okano, J.; Shimizu, R.; Werner, H. In *Secondary Ion Mass Spectrometry SIMS IV*, Proc. 3rd Int. Conf., Budapest, Springer: 1981; pp 438-42.

27. Takats, Z.; Wiseman, J. M.; Gologan, B.; Cooks, R. G., Mass spectrometry sampling under ambient conditions with desorption electrospray ionization. *Science* **2004,** *306* (5695), 471-473.

28. Benninghoven, A., Chemical analysis of inorganic and organic surfaces and thin films by static time-of-flight secondary ion mass spectrometry (TOF-SIMS). *Angewandte Chemie International Edition in English* **1994,** *33* (10), 1023-1043.

29. Stoeckli, M.; Chaurand, P.; Hallahan, D. E.; Caprioli, R. M., Imaging mass spectrometry: a new technology for the analysis of protein expression in mammalian tissues. *Nature medicine* **2001,** *7* (4), 493.

30. Chughtai, K.; Heeren, R. M., Mass spectrometric imaging for biomedical tissue analysis. *Chemical reviews* **2010,** *110* (5), 3237-3277.

31. Hutchens, T. W.; Yip, T. T., New desorption strategies for the mass spectrometric analysis of macromolecules. *Rapid Communications in Mass Spectrometry* **1993,** *7* (7), 576-580.

32. Benesch, J. L.; Robinson, C. V., Mass spectrometry of macromolecular assemblies: preservation and dissociation. *Current opinion in structural biology* **2006,** *16* (2), 245-251.

33. Yost, R.; Enke, C., Triple quadrupole mass spectrometry for direct mixture analysis and structure elucidation. *Analytical chemistry* **1979,** *51* (12), 1251-1264.

34. Amster, I. J., Fourier transform mass spectrometry. *Journal of mass spectrometry* **1996,** *31* (12), 1325-1337.

35. Makarov, A.; Denisov, E.; Kholomeev, A.; Balschun, W.; Lange, O.; Strupat, K.; Horning, S., Performance evaluation of a hybrid linear ion trap/orbitrap mass spectrometer. *Analytical chemistry* **2006,** *78* (7), 2113-2120.

36. Märk, T. D.; Dunn, G. H., *Electron impact ionization*. Springer Science & Business Media: 2013.

37. Fenn, J. B.; Mann, M.; Meng, C. K.; Wong, S. F.; Whitehouse, C. M., Electrospray ionization–principles and practice. *Mass Spectrometry Reviews* **1990,** *9* (1), 37-70.

38. Zenobi, R.; Knochenmuss, R., Ion formation in MALDI mass spectrometry. *Mass spectrometry reviews* **1998,** *17* (5), 337-366.

39. Constantopoulos, T. L.; Jackson, G. S.; Enke, C. G., Effects of salt concentration on analyte response using electrospray ionization mass spectrometry. *Journal of the American Society for Mass Spectrometry* **1999,** *10* (7), 625-634.

40. Yamashita, M.; Fenn, J. B., Negative ion production with the electrospray ion source. *The Journal of Physical Chemistry* **1984,** *88* (20), 4671-4675.

41. Hunt, D. F.; Stafford, G. C.; Crow, F. W.; Russell, J. W., Pulsed positive negative ion chemical ionization mass spectrometry. *Analytical Chemistry* **1976,** *48* (14), 2098-2104.

42. McLafferty, F. W.; Tureček, F.; Turecek, F., *Interpretation of mass spectra*. University science books: 1993.

43. Falconer, I., JJ Thomson and the discovery of the electron. *Physics Education* **1997,** *32* (4), 226.

44. Thomson, J. J., XXVI. Rays of positive electricity. *The London, Edinburgh, and Dublin Philosophical Magazine and Journal of Science* **1911,** *21* (122), 225-249.

45. Thomson, J. J., LVIII. On the masses of the ions in gases at low pressures. *The London, Edinburgh, and Dublin philosophical magazine and journal of science* **1899,** *48* (295), 547-567.

46. Herring, C.; Nichols, M., Thermionic emission. *Reviews of modern physics* **1949,** *21* (2), 185.

47. Fowler, R. H.; Nordheim, L., Electron emission in intense electric fields. *Proceedings of the Royal Society of London. Series A, Containing Papers of a Mathematical and Physical Character* **1928,** *119* (781), 173-181.

48. Spindt, C., Microfabricated field-emission and field-ionization sources. *Surface Science* **1992,** *266* (1-3), 145-154.

49. Zekavat, B.; Solouki, T., Radio-frequency ionization of organic compounds for mass spectrometry analysis. *Angewandte Chemie International Edition* **2013,** *52* (9), 2426-2429.

50. Olaitan, A. D.; Zekavat, B.; Dhungana, B.; Hockaday, W. C.; Chambliss, C. K.; Solouki, T., Analysis of volatile organic compound mixtures using radio-frequency ionization/mass spectrometry. *Analytical Methods* **2014,** *6* (14), 4982-4987.

51. Olaitan, A. D.; Zekavat, B.; Solouki, T., Evidence for electron-based ion generation in radio-frequency ionization. *Journal of Mass Spectrometry* **2016,** *51* (1), 12-19.

52. Harrison, A. G., *Chemical ionization mass spectrometry*. Routledge: 2018.

53. Zaikin, V. G.; Halket, J. M., Derivatization in mass spectrometry—8. Soft ionization mass spectrometry of small molecules. *European Journal of Mass Spectrometry* **2006,** *12* (2), 79-115.

54. Dedieu, M.; Juin, C.; Arpino, P.; Guiochon, G., Soft negative ionization of nonvolatile molecules by introduction of liquid solutions into a chemical ionization mass spectrometer. *Analytical Chemistry* **1982,** *54* (13), 2372-2375.

55. Robb, D. B.; Covey, T. R.; Bruins, A. P., Atmospheric pressure photoionization: an ionization method for liquid chromatography− mass spectrometry. *Analytical Chemistry* **2000,** *72* (15), 3653-3659.

56. Raffaelli, A.; Saba, A., Atmospheric pressure photoionization mass spectrometry. *Mass Spectrometry Reviews* **2003,** *22* (5), 318-331.

57. Schuhle, U.; Pallix, J.; Becker, C., Sensitive mass spectrometry of molecular adsorbates by stimulated desorption and single-photon ionization. *Journal of the American Chemical Society* **1988,** *110* (7), 2323-2324.

58. Boesl, U.; Neusser, H.; Schlag, E., Multi-photon ionization in the mass spectrometry of polyatomic molecules: Cross sections. *Chemical Physics* **1981,** *55* (2), 193-204.

59. Lubman, D. M.; Kronick, M. N., Mass spectrometry of aromatic molecules with resonance-enhanced multiphoton ionization. *Analytical Chemistry* **1982,** *54* (4), 660-665.

60. Beckey, H.-D., *Principles of Field Ionization and Field Desorption Mass Spectrometry: International Series in Analytical Chemistry*. Elsevier: 2016.

61. Beckey, H.-D., *Field Ionization Mass Spectrometry: International Series of Monographs in Analytical Chemistry*. Elsevier: 2017; Vol. 42.

62. Han, X.; Aslanian, A.; Yates III, J. R., Mass spectrometry for proteomics. *Current opinion in chemical biology* **2008,** *12* (5), 483-490.

63. Gstaiger, M.; Aebersold, R., Applying mass spectrometry-based proteomics to genetics, genomics and network biology. *Nature Reviews Genetics* **2009,** *10* (9), 617.

64. Link, A. J.; Eng, J.; Schieltz, D. M.; Carmack, E.; Mize, G. J.; Morris, D. R.; Garvik, B. M.; Yates, J. R., Direct analysis of protein complexes using mass spectrometry. *Nature biotechnology* **1999,** *17* (7), 676.

65. Snyder, L. R.; Kirkland, J. J.; Dolan, J. W., *Introduction to modern liquid chromatography*. John Wiley & Sons: 2011.

66. Covey, T. R.; Lee, E. D.; Bruins, A. P.; Henion, J. D., Liquid chromatography/mass spectrometry. *Analytical chemistry* **1986,** *58* (14), 1451A-1461A.

67. Fenn, J. B.; Mann, M.; Meng, C. K.; Wong, S. F.; Whitehouse, C. M., Electrospray ionization for mass spectrometry of large biomolecules. *Science* **1989,** *246* (4926), 64-71.

68. Iribarne, J.; Thomson, B., On the evaporation of small ions from charged droplets. *The Journal of chemical physics* **1976,** *64* (6), 2287-2294.

69. Dole, M.; Mack, L. L.; Hines, R. L.; Mobley, R. C.; Ferguson, L. D.; Alice, M. B., Molecular beams of macroions. *The Journal of chemical physics* **1968,** *49* (5), 2240-2249.

70. Konermann, L.; Ahadi, E.; Rodriguez, A. D.; Vahidi, S., Unraveling the mechanism of electrospray ionization. ACS Publications: 2012.

71. Striegel, A. M.; Piotrowiak, P.; Boué, S. M.; Cole, R. B., Polarizability and inductive effect contributions to solvent–cation binding observed in electrospray ionization mass spectrometry. *Journal of the American Society for Mass Spectrometry* **1999,** *10* (3), 254-260.

72. Bruins, A. P.; Covey, T. R.; Henion, J. D., Ion spray interface for combined liquid chromatography/atmospheric pressure ionization mass spectrometry. *Analytical Chemistry* **1987,** *59* (22), 2642-2646.

73. McDonnell, L. A.; Heeren, R. M., Imaging mass spectrometry. *Mass spectrometry reviews* **2007,** *26* (4), 606-643.

74. van Hove, E. R. A.; Smith, D. F.; Heeren, R. M., A concise review of mass spectrometry imaging. *Journal of chromatography A* **2010,** *1217* (25), 3946-3954.

75. Caprioli, R. M., Imaging mass spectrometry: Molecular microscopy for the new age of biology and medicine. *Proteomics* **2016,** *16* (11-12), 1607-1612.

76. Benninghoven, A., Surface analysis by secondary ion mass spectrometry (SIMS). *Surface Science* **1994,** *299*, 246-260.

77. Caprioli, R. M.; Farmer, T. B.; Gile, J., Molecular imaging of biological samples: localization of peptides and proteins using MALDI-TOF MS. *Analytical chemistry* **1997,** *69* (23), 4751-4760.

78. Meier, M. A.; Adams, N.; Schubert, U. S., Statistical approach to understand MALDI-TOFMS matrices: discovery and evaluation of new MALDI matrices. *Analytical chemistry* **2007,** *79* (3), 863-869.

79. Cornett, D. S.; Reyzer, M. L.; Chaurand, P.; Caprioli, R. M., MALDI imaging mass spectrometry: molecular snapshots of biochemical systems. *Nature methods* **2007,** *4* (10), 828-833.

80. Barber, M.; Bordoli, R. S.; Sedgwick, R. D.; Tyler, A. N., Fast atom bombardment of solids (FAB): A new ion source for mass spectrometry. *Journal of the Chemical Society, Chemical Communications* **1981,** (7), 325-327.

81. Barber, M.; Bordoli, R. S.; Elliott, G. J.; Sedgwick, R. D.; Tyler, A. N., Fast atom bombardment mass spectrometry. *Analytical Chemistry* **1982,** *54* (4), 645A-657A.

82. Morris, H. R.; Panico, M.; Barber, M.; Bordoli, R. S.; Sedgwick, R. D.; Tyler, A., Fast atom bombardment: a new mass spectrometric method for peptide sequence analysis. *Biochemical and biophysical research communications* **1981,** *101* (2), 623-631.

83. Tomiyasu, B.; Fukuju, I.; Komatsubara, H.; Owari, M.; Nihei, Y., High spatial resolution 3D analysis of materials using gallium focused ion beam secondary ion mass spectrometry (FIB SIMS). *Nuclear Instruments and Methods in Physics Research Section B: Beam Interactions with Materials and Atoms* **1998,** *136*, 1028-1033.

84. Weibel, D.; Wong, S.; Lockyer, N.; Blenkinsopp, P.; Hill, R.; Vickerman, J. C., A C60 primary ion beam system for time of flight secondary ion mass spectrometry: its development and secondary ion yield characteristics. *Analytical Chemistry* **2003,** *75* (7), 1754-1764.

85. McLafferty, F. W., Tandem mass spectrometry. *Science* **1981,** *214* (4518), 280-287.

86. Mattauch, J., A double-focusing mass spectrograph and the masses of N 15 and O 18. *Physical Review* **1936,** *50* (7), 617.

87. Kemper, P. R.; Bowers, M. T., A hybrid double-focusing mass spectrometer—high-pressure drift reaction cell to study thermal energy reactions of mass-selected ions. *Journal of the American Society for Mass Spectrometry* **1990,** *1* (3), 197-207.

88. Bruins, A.; Jennings, K.; Evans, S., The observation of metastable transitions in a double-focussing mass spectrometer using a linked scan of the electric sector and magnetic sector fields. *International Journal of Mass Spectrometry and Ion Physics* **1978,** *26* (4), 395-404.

89. Dawson, P. H., *Quadrupole mass spectrometry and its applications*. Elsevier: 2013.

90. Wiley, W.; McLaren, I. H., Time-of-flight mass spectrometer with improved resolution. *Review of Scientific Instruments* **1955,** *26* (12), 1150-1157.

91. March, R. E., An introduction to quadrupole ion trap mass spectrometry. *Journal of mass spectrometry* **1997,** *32* (4), 351-369.

92. Perry, R. H.; Cooks, R. G.; Noll, R. J., Orbitrap mass spectrometry: instrumentation, ion motion and applications. *Mass spectrometry reviews* **2008,** *27* (6), 661-699.

93. Marshall, A. G.; Hendrickson, C. L.; Jackson, G. S., Fourier transform ion cyclotron resonance mass spectrometry: a primer. *Mass spectrometry reviews* **1998,** *17* (1), 1-35.

94. Makarov, A.; Denisov, E.; Lange, O.; Horning, S., Dynamic range of mass accuracy in LTQ Orbitrap hybrid mass spectrometer. *Journal of the American Society for Mass Spectrometry* **2006,** *17* (7), 977-982.

95. Polfer, N. C.; Oomens, J.; Dunbar, R. C., IRMPD spectroscopy of metal-ion/tryptophan complexes. *Physical Chemistry Chemical Physics* **2006,** *8* (23), 2744-2751.

96. Daly, N., Scintillation type mass spectrometer ion detector. *Review of Scientific Instruments* **1960,** *31* (3), 264-267.

97. Gerdin, G.; Stygar, W.; Venneri, F., Faraday cup analysis of ion beams produced by a dense plasma focus. *Journal of Applied Physics* **1981,** *52* (5), 3269-3275.

98. Allen, J. S., An improved electron multiplier particle counter. *Review of Scientific Instruments* **1947,** *18* (10), 739-749.

99. Burroughs, E., Collection Efficiency of Continuous Dynode Electron Multiple Arrays. *Review of Scientific Instruments* **1969,** *40* (1), 35-37.

100. Wiza, J. L., Microchannel plate detectors. *Nucl. Instrum. Methods* **1979,** *162* (1-3), 587-601.

101. Murray, K. K.; Boyd, R. K.; Eberlin, M. N.; Langley, G. J.; Li, L.; Naito, Y., Definitions of terms relating to mass spectrometry (IUPAC Recommendations 2013). *Pure and Applied Chemistry* **2013,** *85* (7), 1515-1609.

102. Bracewell, R. N.; Bracewell, R. N., *The Fourier transform and its applications*. McGraw-Hill New York: 1986; Vol. 31999.

103. Comisarow, M. B., Cubic trapped-ion cell for ion cyclotron resonance. *International Journal of Mass Spectrometry and Ion Physics* **1981,** *37* (2), 251-257.

104. Comisarow, M. B., Signal modeling for ion cyclotron resonance. *The Journal of Chemical Physics* **1978,** *69* (9), 4097-4104.

105. Tilford, C. R., Pressure and vacuum measurements. *Physical methods of chemistry* **1992,** *6*.

106. Blakeman, K. H.; Wolfe, D. W.; Cavanaugh, C. A.; Ramsey, J. M., High pressure mass spectrometry: the generation of mass spectra at operating pressures exceeding 1 Torr in a microscale cylindrical ion trap. *Analytical chemistry* **2016,** *88* (10), 5378-5384.

107. Weise, H.; Kowalewsky, H.; Wenz, R., Behaviour of elastomeric seals at low temperature. *Vacuum* **1992,** *43* (5-7), 555-557.

108. Kurokouchi, S.; Shinoda, S.; Morita, S., Dependence of the seal property of ConFlat-type flanges on the fine dimensions of the knife edge. *Journal of Vacuum Science & Technology A: Vacuum, Surfaces, and Films* **2003,** *21* (2), 438-448.

109. Battes, K.; Day, C.; Hauer, V., Outgassing behavior of different high-temperature resistant polymers. *Journal of Vacuum Science & Technology A: Vacuum, Surfaces, and Films* **2018,** *36* (2), 021602.

110. Hablanian, M. H., *High-vacuum technology: a practical guide*. Routledge: 2017.

111. Pringle, S. D.; Giles, K.; Wildgoose, J. L.; Williams, J. P.; Slade, S. E.; Thalassinos, K.; Bateman, R. H.; Bowers, M. T.; Scrivens, J. H., An investigation of the mobility separation of some peptide and protein ions using a new hybrid quadrupole/travelling wave IMS/oa-ToF instrument. *International Journal of Mass Spectrometry* **2007,** *261* (1), 1-12.

112. Geankoplis, C. J., *Transport processes and separation process principles:(includes unit operations)*. Prentice Hall Professional Technical Reference: 2003.

113. Hoffmann, K., *Applying the Wheatstone bridge circuit*. HBM Germany: 1974.

114. Utterback, N. G.; Griffith Jr, T., Reliable submicron pressure readings with capacitance manometer. *Review of Scientific Instruments* **1966,** *37* (7), 866-870.

115. Liptak, B. G., *Instrument Engineers' Handbook, Volume Two: Process Control and Optimization*. CRC press: 2018.

116. Schmitt, R., *Electromagnetics explained: a handbook for wireless/RF, EMC, and high-speed electronics*. Elsevier: 2002.

117. Dorf, R. C., *The electrical engineering handbook*. CRC press: 1997.

118. Walden, R. H., Analog-to-digital converter survey and analysis. *IEEE Journal on selected areas in communications* **1999,** *17* (4), 539-550.

119. Hoeschele, D. F., *Analog-to-digital and digital-to-analog conversion techniques*. Wiley New York: 1994; Vol. 968.

120. Technologies, A. https://www.ardaratech.com/ (accessed 4/1/2019).

121. Engineering, G. C. http://mstar2k.com/gaace-home (accessed 4/1/2019).

122. Stahl-Electronics https://www.stahl-electronics.com/ (accessed 4/1/2019).

123. CMS, E. https://www.extrel.com/ (accessed 4/1/2019).

124. Fasmatech http://fasmatech.com/ (accessed 4/1/2019).

125. Hinshaw, J. V., New Gas Chromatography Products, 2014–2015. **2015**.

126. McLean, J. A.; Ridenour, W. B.; Caprioli, R. M., Profiling and imaging of tissues by imaging ion mobility-mass spectrometry. *Journal of mass spectrometry* **2007,** *42* (8), 1099-1105.

127. Stauber, J.; MacAleese, L.; Franck, J.; Claude, E.; Snel, M.; Kaletas, B. K.; Wiel, I. M.; Wisztorski, M.; Fournier, I.; Heeren, R. M., On-tissue protein identification and imaging by MALDI-ion mobility mass spectrometry. *Journal of the American Society for Mass Spectrometry* **2010,** *21* (3), 338-347.

128. Format, N. I.-T. F. http://www.ni.com/product-documentation/3727/en/ (accessed 5/3/2019).

129. Shafranovich, Y., Common format and MIME type for comma-separated values (CSV) files. **2005**.

130. Bray, T.; Paoli, J.; Sperberg-McQueen, C. M.; Maler, E.; Yergeau, F., Extensible markup language (XML) 1.0. W3C recommendation October: 2000.

131. Crockford, D. *The application/json media type for javascript object notation (json)*; 2070-1721; 2006.

132. Cattell, R., Scalable SQL and NoSQL data stores. *Acm Sigmod Record* **2011,** *39* (4), 12-27.

133. McKinney, W. In *Data structures for statistical computing in python*, Proceedings of the 9th Python in Science Conference, Austin, TX: 2010; pp 51-56.

134. MATLAB, T. M. https://www.mathworks.com/products/matlab.html (accessed 5/4/2019).

135. Team, R. C., R: A language and environment for statistical computing. **2013**.

136. Sodhi, R. N., Time-of-flight secondary ion mass spectrometry (TOF-SIMS):—versatility in chemical and imaging surface analysis. *Analyst* **2004,** *129* (6), 483-487.

137. Laskin, J.; Heath, B. S.; Roach, P. J.; Cazares, L.; Semmes, O. J., Tissue imaging using nanospray desorption electrospray ionization mass spectrometry. *Analytical chemistry* **2011,** *84* (1), 141-148.

138. Wu, C.; Dill, A. L.; Eberlin, L. S.; Cooks, R. G.; Ifa, D. R., Mass spectrometry imaging under ambient conditions. *Mass spectrometry reviews* **2013,** *32* (3), 218-243.

139. Swanson, L., Liquid metal ion sources: Mechanism and applications. *Nuclear Instruments and Methods in Physics Research* **1983,** *218* (1-3), 347-353.

140. Ji, L. *Plasma ion sources and ion beam technology inmicrofabrications*; Lawrence Berkeley National Lab.(LBNL), Berkeley, CA (United States): 2007.

141. Mahoney, J.; Perel, J.; Ruatta, S.; Martino, P.; Husain, S.; Cook, K.; Lee, T., Massive cluster impact mass spectrometry: A new desorption method for the analysis of large biomolecules. *Rapid communications in mass spectrometry* **1991,** *5* (10), 441-445.

142. Kirkpatrick, A., Gas cluster ion beam applications and equipment. *Nuclear Instruments and Methods in Physics Research Section B: Beam Interactions with Materials and Atoms* **2003,** *206*, 830-837.

143. Glückmann, M.; Pfenninger, A.; Krüger, R.; Thierolf, M.; Karasa, M.; Horneffer, V.; Hillenkamp, F.; Strupat, K., Mechanisms in MALDI analysis: surface interaction or incorporation of analytes? *International Journal of Mass Spectrometry* **2001,** *210*, 121-132.

144. Gimon, M.; Preston, L.; Solouki, T.; White, M.; Russell, D., Are proton transfer reactions of excited states involved in UV laser desorption ionization? *Organic mass spectrometry* **1992,** *27* (7), 827-830.

145. Croxatto, A.; Prod'hom, G.; Greub, G., Applications of MALDI-TOF mass spectrometry in clinical diagnostic microbiology. *FEMS microbiology reviews* **2012,** *36* (2), 380-407.

146. Easterling, M. L.; Mize, T. H.; Amster, I. J., Routine part-per-million mass accuracy for high-mass ions: Space-charge effects in MALDI FT-ICR. *Analytical chemistry* **1999,** *71* (3), 624-632.

147. Solouki, T.; Paša-Tolić, L.; Jackson, G. S.; Guan, S.; Marshall, A. G., High-resolution multistage MS, MS2, and MS3 matrix-assisted laser desorption/ionization FT-ICR mass spectra of peptides from a single laser shot. *Analytical chemistry* **1996,** *68* (21), 3718-3725.

148. Richards, A. L.; Lietz, C. B.; Wager-Miller, J. B.; Mackie, K.; Trimpin, S., Imaging mass spectrometry in transmission geometry. *Rapid Communications in Mass Spectrometry* **2011,** *25* (6), 815-820.

149. Park, S. G.; Murray, K. K., Infrared laser ablation sample transfer for on-line liquid chromatography electrospray ionization mass spectrometry. *Journal of Mass Spectrometry* **2012,** *47* (10), 1322-1326.

150. Park, S.-G.; Murray, K. K., Infrared laser ablation sample transfer for MALDI and electrospray. *Journal of the American Society for Mass Spectrometry* **2011,** *22* (8), 1352-1362.

151. O'Brien, J. T.; Williams, E. R.; Holman, H.-Y. N., Ambient infrared laser ablation mass spectrometry (AIRLAB-MS) of live plant tissue with plume capture by continuous flow solvent probe. *Analytical chemistry* **2015,** *87* (5), 2631-2638.

152. https://www.lsu.edu/science/soar/files/how_big_is_a_cell.pdf (accessed 6/15/2019).

153. Zavalin, A.; Yang, J.; Caprioli, R., Laser beam filtration for high spatial resolution MALDI imaging mass spectrometry. *Journal of the American Society for Mass Spectrometry* **2013,** *24* (7), 1153-1156.

154. Wiseman, J. M.; Ifa, D. R.; Song, Q.; Cooks, R. G., Tissue imaging at atmospheric pressure using desorption electrospray ionization (DESI) mass spectrometry. *Angewandte Chemie International Edition* **2006,** *45* (43), 7188-7192.

155. Nemes, P.; Barton, A. A.; Li, Y.; Vertes, A., Ambient molecular imaging and depth profiling of live tissue by infrared laser ablation electrospray ionization mass spectrometry. *Analytical chemistry* **2008,** *80* (12), 4575-4582.

156. Whitby, J. A.; Östlund, F.; Horvath, P.; Gabureac, M.; Riesterer, J. L.; Utke, I.; Hohl, M.; Sedláček, L.; Jiruše, J.; Friedli, V., High spatial resolution time-of-flight secondary ion mass spectrometry for the masses: a novel orthogonal ToF FIB-SIMS instrument with in situ AFM. *Advances in Materials Science and Engineering* **2012,** *2012*.

157. Wong, S.; Hill, R.; Blenkinsopp, P.; Lockyer, N.; Weibel, D.; Vickerman, J., Development of a C60+ ion gun for static SIMS and chemical imaging. *Applied Surface Science* **2003,** *203*, 219-222.

158. Daniel, J.; Moore, D.; Walker, J., Focused ion beams for microfabrication. *Engineering Science & Education Journal* **1998,** *7* (2), 53-56.

159. Bozzola, J. J.; Russell, L. D., *Electron microscopy: principles and techniques for biologists*. Jones & Bartlett Learning: 1999.

160. Calder, R.; Lewin, G., Reduction of stainless-steel outgassing in ultra-high vacuum. *British Journal of Applied Physics* **1967,** *18* (10), 1459.

161. Senko, M. W.; Hendrickson, C. L.; Emmett, M. R.; Shi, S. D.-H.; Marshall, A. G., External accumulation of ions for enhanced electrospray ionization Fourier transform ion cyclotron resonance mass spectrometry. *Journal of the American Society for Mass Spectrometry* **1997,** *8* (9), 970-976.

162. Jiao, C. Q.; Ranatunga, D. R. A.; Vaughn, W. E.; Freiser, B. S., A pulsed-leak valve for use with ion trapping mass spectrometers. *Journal of the American Society for Mass Spectrometry* **1996,** *7* (1), 118-122.

163. Liyanage, O. T.; Brantley, M. R.; Calixte, E. I.; Solouki, T.; Shuford, K. L.; Gallagher, E. S., Characterization of electrospray ionization (ESI) parameters on in-ESI hydrogen/deuterium exchange of carbohydrate-metal ion adducts. *Journal of the American Society for Mass Spectrometry* **2019,** *30* (2), 235-247.

164. Kaufmann, A., The current role of high-resolution mass spectrometry in food analysis. *Analytical and Bioanalytical Chemistry* **2012,** *403* (5), 1233-1249.

165. Benson, S.; Lennard, C.; Maynard, P.; Roux, C., Forensic applications of isotope ratio mass spectrometry—a review. *Forensic science international* **2006,** *157* (1), 1-22.

166. Montaser, A., *Inductively coupled plasma mass spectrometry*. John Wiley & Sons: 1998.

167. Aebersold, R.; Mann, M., Mass spectrometry-based proteomics. *Nature* **2003,** *422* (6928), 198.

168. Gillespie, T. A.; Winger, B. E., Mass spectrometry for small molecule pharmaceutical product development: a review. *Mass spectrometry reviews* **2011,** *30* (3), 479-490.

169. Shushan, B., A review of clinical diagnostic applications of liquid chromatography–tandem mass spectrometry. *Mass spectrometry reviews* **2010,** *29* (6), 930-944.

170. Snyder, D. T.; Pulliam, C. J.; Ouyang, Z.; Cooks, R. G., Miniature and fieldable mass spectrometers: recent advances. *Analytical chemistry* **2015,** *88* (1), 2-29.

171. Smith, D. F.; Podgorski, D. C.; Rodgers, R. P.; Blakney, G. T.; Hendrickson, C. L., 21 tesla FT-ICR mass spectrometer for ultrahigh-resolution analysis of complex organic mixtures. *Analytical chemistry* **2018,** *90* (3), 2041-2047.

172. Yoon, O. K.; Zuleta, I. A.; Kimmel, J. R.; Robbins, M. D.; Zare, R. N., Duty cycle and modulation efficiency of two-channel hadamard transform time-of-flight mass spectrometry. *Journal of the American society for mass spectrometry* **2005,** *16* (11), 1888-1901.

173. Tabb, D. L.; Vega-Montoto, L.; Rudnick, P. A.; Variyath, A. M.; Ham, A.-J. L.; Bunk, D. M.; Kilpatrick, L. E.; Billheimer, D. D.; Blackman, R. K.; Cardasis, H. L., Repeatability and reproducibility in proteomic identifications by liquid chromatography− tandem mass spectrometry. *Journal of proteome research* **2009,** *9* (2), 761-776.

174. Ouyang, Z.; Cooks, R. G., Miniature mass spectrometers. *Annual Review of Analytical Chemistry* **2009,** *2*, 187-214.

175. Morris, H. R.; Paxton, T.; Dell, A.; Langhorne, J.; Berg, M.; Bordoli, R. S.; Hoyes, J.; Bateman, R. H., High sensitivity collisionally-activated decomposition tandem mass spectrometry on a novel quadrupole/orthogonal-acceleration time-of-flight mass spectrometer. *Rapid Communications in Mass Spectrometry* **1996,** *10* (8), 889-896.

176. Valaskovic, G. A.; Kelleher, N. L.; Little, D. P.; Aaserud, D. J.; McLafferty, F. W., Attomole-sensitivity electrospray source for large-molecule mass spectrometry. *Analytical chemistry* **1995,** *67* (20), 3802-3805.

177. Solouki, T.; Marto, J. A.; White, F. M.; Guan, S.; Marshall, A. G., Attomole biomolecule mass analysis by matrix-assisted laser desorption/ionization Fourier transform ion cyclotron resonance. *Analytical chemistry* **1995,** *67* (22), 4139-4144.

178. Blakney, G. T.; Hendrickson, C. L.; Marshall, A. G., Predator data station: a fast data acquisition system for advanced FT-ICR MS experiments. *International Journal of Mass Spectrometry* **2011,** *306* (2-3), 246-252.

179. Kooijman, P. C.; Nagornov, K. O.; Kozhinov, A. N.; Kilgour, D. P.; Tsybin, Y. O.; Heeren, R. M.; Ellis, S. R., Increased throughput and ultra-high mass resolution in DESI FT-ICR MS imaging through new-generation external data acquisition system and advanced data processing approaches. *Scientific reports* **2019,** *9* (1), 8.

180. Röst, H. L.; Sachsenberg, T.; Aiche, S.; Bielow, C.; Weisser, H.; Aicheler, F.; Andreotti, S.; Ehrlich, H.-C.; Gutenbrunner, P.; Kenar, E., OpenMS: a flexible open-source software platform for mass spectrometry data analysis. *Nature methods* **2016,** *13* (9), 741.

181. Bilbao, A.; Varesio, E.; Luban, J.; Strambio-De-Castillia, C.; Hopfgartner, G.; Müller, M.; Lisacek, F., Processing strategies and software solutions for data-independent acquisition in mass spectrometry. *Proteomics* **2015,** *15* (5-6), 964-980.

182. Mueller, L. N.; Brusniak, M.-Y.; Mani, D.; Aebersold, R., An assessment of software solutions for the analysis of mass spectrometry based quantitative proteomics data. *Journal of proteome research* **2008,** *7* (01), 51-61.

183. Kaiser, N. K.; Quinn, J. P.; Blakney, G. T.; Hendrickson, C. L.; Marshall, A. G., A novel 9.4 Tesla FTICR mass spectrometer with improved sensitivity, mass resolution, and mass range. *Journal of the American Society for Mass Spectrometry* **2011,** *22* (8), 1343-1351.

184. Gross, J. H., Direct analysis in real time—a critical review on DART-MS. *Analytical and bioanalytical chemistry* **2014,** *406* (1), 63-80.

185. Zavalin, A.; Todd, E. M.; Rawhouser, P. D.; Yang, J.; Norris, J. L.; Caprioli, R. M., Direct imaging of single cells and tissue at sub-cellular spatial resolution using transmission geometry MALDI MS. *Journal of Mass Spectrometry* **2012,** *47* (11), 1473-1481.

186. Zubarev, R. A.; Makarov, A., Orbitrap mass spectrometry. *Analytical Chemistry* **2013,** *85* (11), 5288-5296.

187. Tolmachev, A. V.; Robinson, E. W.; Wu, S.; Kang, H.; Lourette, N. M.; Paša-Tolić, L.; Smith, R. D., Trapped-ion cell with improved DC potential harmonicity for FT-ICR MS. *Journal of the American Society for Mass Spectrometry* **2008,** *19* (4), 586-597.

188. Ibrahim, Y. M.; Hamid, A. M.; Deng, L.; Garimella, S. V.; Webb, I. K.; Baker, E. S.; Smith, R. D., New frontiers for mass spectrometry based upon structures for lossless ion manipulations. *Analyst* **2017,** *142* (7), 1010-1021.

189. Giles, K.; Pringle, S. D.; Worthington, K. R.; Little, D.; Wildgoose, J. L.; Bateman, R. H., Applications of a travelling wave-based radio-frequency-only stacked ring ion guide. *Rapid Communications in Mass Spectrometry* **2004,** *18* (20), 2401-2414.

190. Kanu, A. B.; Dwivedi, P.; Tam, M.; Matz, L.; Hill Jr, H. H., Ion mobility–mass spectrometry. *Journal of mass spectrometry* **2008,** *43* (1), 1-22.

191. Ruotolo, B. T.; Benesch, J. L.; Sandercock, A. M.; Hyung, S.-J.; Robinson, C. V., Ion mobility–mass spectrometry analysis of large protein complexes. *Nature protocols* **2008,** *3* (7), 1139.

192. Dahl, D. A., SIMION for the personal computer in reflection. *International Journal of Mass Spectrometry* **2000,** *200* (1-3), 3-25.

193. Marinach, C.; Brunot, A.; Beaugrand, C.; Bolbach, G.; Tabet, J., Simulation of ion beam and optimization of orthogonal tandem ion trap/reflector time-of-flight mass spectrometry. *International Journal of Mass Spectrometry* **2002,** *213* (1), 45-62.

194. Hendrickson, C. L.; Beu, S. C.; Blakney, G. T.; Marshall, A. G., SIMION modeling of ion image charge detection in Fourier transform ion cyclotron resonance mass spectrometry. *International Journal of Mass Spectrometry* **2009,** *283* (1-3), 100-104.

195. Appelhans, A. D.; Dahl, D. A., SIMION ion optics simulations at atmospheric pressure. *International Journal of Mass Spectrometry* **2005,** *244* (1), 1-14.

196. Hernandez, D. R.; DeBord, J. D.; Ridgeway, M. E.; Kaplan, D. A.; Park, M. A.; Fernandez-Lima, F., Ion dynamics in a trapped ion mobility spectrometer. *Analyst* **2014,** *139* (8), 1913-1921.

197. Lai, H.; McJunkin, T. R.; Miller, C. J.; Scott, J. R.; Almirall, J. R., The predictive power of SIMION/SDS simulation software for modeling ion mobility spectrometry instruments. *International Journal of Mass Spectrometry* **2008,** *276* (1), 1-8.

198. Marto, J. A.; Marshall, A. G.; May, M. A.; Limbach, P. A., Ion trajectories in an electrostatic ion guide for external ion source fourier transform ion cyclotron resonance mass spectrometry. *Journal of the American Society for Mass Spectrometry* **1995,** *6* (10), 936-946.

199. Shaffer, S. A.; Tang, K.; Anderson, G. A.; Prior, D. C.; Udseth, H. R.; Smith, R. D., A novel ion funnel for focusing ions at elevated pressure using electrospray ionization mass spectrometry. *Rapid communications in mass spectrometry* **1997,** *11* (16), 1813-1817.

200. Wilcox, B. E.; Hendrickson, C. L.; Marshall, A. G., Improved ion extraction from a linear octopole ion trap: SIMION analysis and experimental demonstration. *Journal of the American Society for Mass Spectrometry* **2002,** *13* (11), 1304-1312.

201. Ding, L.; Sudakov, M.; Kumashiro, S., A simulation study of the digital ion trap mass spectrometer. *International Journal of Mass Spectrometry* **2002,** *221* (2), 117-138.

202. Sun, W.; May, J. C.; Russell, D. H., A novel surface-induced dissociation instrument for ion mobility-time-of-flight mass spectrometry. *International Journal of Mass Spectrometry* **2007,** *259* (1-3), 79-86.

203. Dahl, D. A.; McJunkin, T. R.; Scott, J. R., Comparison of ion trajectories in vacuum and viscous environments using SIMION: Insights for instrument design. *International Journal of Mass Spectrometry* **2007,** *266* (1-3), 156-165.

204. Fletcher, R., *Practical methods of optimization*. John Wiley & Sons: 2013.

205. Metropolis, N.; Ulam, S., The monte carlo method. *Journal of the American statistical association* **1949,** *44* (247), 335-341.

206. Krutchinsky, A.; Chernushevich, I.; Spicer, V.; Ens, W.; Standing, K., Collisional damping interface for an electrospray ionization time-of-flight mass spectrometer. *Journal of the American Society for Mass Spectrometry* **1998,** *9* (6), 569-579.

207. Han, F.; Du, Y.; Cheng, S.; Zhou, Q.; Chen, C.; Wang, W.; Li, H., Computational fluid dynamics-Monte Carlo method for calculation of the ion trajectories and applications in ion mobility spectrometry. *International Journal of Mass Spectrometry* **2012,** *309*, 13-21.

208. Weile, D. S.; Michielssen, E., Genetic algorithm optimization applied to electromagnetics: A review. *IEEE Transactions on Antennas and Propagation* **1997,** *45* (3), 343-353.

209. Sivanandam, S.; Deepa, S., Genetic algorithm optimization problems. In *Introduction to Genetic Algorithms*, Springer: 2008; pp 165-209.

210. Guan, S.; Marshall, A. G., Stacked-ring electrostatic ion guide. *Journal of the American Society for Mass Spectrometry* **1996,** *7* (1), 101-106.

211. Zekavat, B.; Szulejko, J. E.; LaBrecque, D.; Olaitan, A. D.; Solouki, T., Efficient injection of low-mass ions into high magnetic field Fourier transform ion cyclotron resonance mass spectrometers. *Rapid Communications in Mass Spectrometry* **2014,** *28* (2), 230-238.

212. Beu, S. C.; Hendrickson, C. L.; Marshall, A. G., Excitation of radial ion motion in an rf-only multipole ion guide immersed in a strong magnetic field gradient. *Journal of the American Society for Mass Spectrometry* **2011,** *22* (3), 591-601.

213. Webster, J. G., *The measurement, instrumentation and sensors handbook*. CRC press: 1998.

214. Yinon, J., Field detection and monitoring of explosives. *TrAC Trends in Analytical Chemistry* **2002,** *21* (4), 292-301.

215. Cai, Y.; Cao, D.; He, X.; Wang, Q., Continuous glucose monitoring system based on smart phone. *Procedia Engineering* **2012,** *29*, 3894-3898.

216. Barisano, G.; Sepehrband, F.; Ma, S.; Jann, K.; Cabeen, R.; Wang, D. J.; Toga, A. W.; Law, M., Clinical 7 T MRI: Are we there yet? A review about magnetic resonance imaging at ultra-high field. *The British Journal of Radiology* **2019,** *92* (1094), 20180492.

217. Wang, B.; Kong, W.; Guan, H.; Xiong, N. N., Air Quality Forcasting based on Gated Recurrent Long Short Term Memory Model in Internet of Things. *IEEE Access* **2019**.

218. Duan, W.; Liu, A.; Li, Q.; Li, Z.; Wen, C.-Y.; Cai, Z.; Tang, S.; Li, X.; Zeng, J., Toward ultrasensitive and fast colorimetric detection of indoor formaldehyde across the visible region using cetyltrimethylammonium chloride-capped bone-shaped gold nanorods as “chromophores”. *Analyst* **2019**.

219. Loo, J. A., Electrospray ionization mass spectrometry: a technology for studying noncovalent macromolecular complexes. *International Journal of Mass Spectrometry* **2000,** *200* (1-3), 175-186.

220. Cheng, K.; Chui, H.; Domish, L.; Hernandez, D.; Wang, G., Recent development of mass spectrometry and proteomics applications in identification and typing of bacteria. *PROTEOMICS–Clinical Applications* **2016,** *10* (4), 346-357.

221. Hendrickson, C. L.; Quinn, J. P.; Kaiser, N. K.; Smith, D. F.; Blakney, G. T.; Chen, T.; Marshall, A. G.; Weisbrod, C. R.; Beu, S. C., 21 Tesla Fourier transform ion cyclotron resonance mass spectrometer: a national resource for ultrahigh resolution mass analysis. *Journal of the American Society for Mass Spectrometry* **2015,** *26* (9), 1626-1632.

222. Xian, F.; Hendrickson, C. L.; Marshall, A. G., High resolution mass spectrometry. *Analytical chemistry* **2012,** *84* (2), 708-719.

223. Awad, H.; Khamis, M. M.; El-Aneed, A., Mass spectrometry, review of the basics: ionization. *Applied Spectroscopy Reviews* **2015,** *50* (2), 158-175.

224. Boesl, U., Time-of-flight mass spectrometry: introduction to the basics. *Mass spectrometry reviews* **2017,** *36* (1), 86-109.

225. Pluskal, T.; Castillo, S.; Villar-Briones, A.; Orešič, M., MZmine 2: modular framework for processing, visualizing, and analyzing mass spectrometry-based molecular profile data. *BMC bioinformatics* **2010,** *11* (1), 395.

226. Bateman, N. W.; Goulding, S. P.; Shulman, N. J.; Gadok, A. K.; Szumlinski, K. K.; MacCoss, M. J.; Wu, C. C., Maximizing peptide identification events in proteomic workflows using data-dependent acquisition (DDA). *Molecular & Cellular Proteomics* **2014,** *13* (1), 329-338.

227. OuYang, C.; Chen, B.; Li, L., High throughput in situ DDA analysis of neuropeptides by coupling novel multiplex mass spectrometric imaging (MSI) with gas-phase fractionation. *Journal of The American Society for Mass Spectrometry* **2015,** *26* (12), 1992-2001.

228. Michalski, A.; Cox, J.; Mann, M., More than 100,000 detectable peptide species elute in single shotgun proteomics runs but the majority is inaccessible to data-dependent LC− MS/MS. *Journal of proteome research* **2011,** *10* (4), 1785-1793.

229. Soltwisch, J.; Kettling, H.; Vens-Cappell, S.; Wiegelmann, M.; Müthing, J.; Dreisewerd, K., Mass spectrometry imaging with laser-induced postionization. *Science* **2015,** *348* (6231), 211-215.

230. Brunelle, A.; Touboul, D.; Laprévote, O., Biological tissue imaging with time-of-flight secondary ion mass spectrometry and cluster ion sources. *Journal of Mass Spectrometry* **2005,** *40* (8), 985-999.

231. Alexandrov, T., MALDI imaging mass spectrometry: statistical data analysis and current computational challenges. *BMC bioinformatics* **2012,** *13* (16), S11.

232. McDonnell, L. A.; van Remoortere, A.; van Zeijl, R. J.; Dalebout, H.; Bladergroen, M. R.; Deelder, A. M., Automated imaging MS: toward high throughput imaging mass spectrometry. *Journal of proteomics* **2010,** *73* (6), 1279-1282.

233. Bottomley, P. A., A versatile magnetic field gradient control system for NMR imaging. *Journal of Physics E: Scientific Instruments* **1981,** *14* (9), 1081.

234. Edelen, A.; Biedron, S.; Chase, B.; Edstrom, D.; Milton, S.; Stabile, P., Neural networks for modeling and control of particle accelerators. *IEEE Transactions on Nuclear Science* **2016,** *63* (2), 878-897.

235. Schorb, M.; Haberbosch, I.; Hagen, W. J.; Schwab, Y.; Mastronarde, D. N., Software tools for automated transmission electron microscopy. *Nature methods* **2019**, 1.

236. Haas, J. K., A history of the Unity game engine. **2014**.

237. Busby, J.; Parrish, Z.; Wilson, J., *Mastering Unreal Technology, Volume II: Advanced Level Design Concepts with Unreal Engine 3*. Sams Publishing: 2009.

238. Lewis, M.; Jacobson, J., Game engines. *Communications of the ACM* **2002,** *45* (1), 27.

239. Xie, J. In *Research on key technologies base Unity3D game engine*, 2012 7th international conference on computer science & education (ICCSE), IEEE: 2012; pp 695-699.

240. Sabin-Wilson, L., *WordPress for dummies*. John Wiley & Sons: 2011.

241. Patel, S. K.; Rathod, V.; Prajapati, J. B., Performance analysis of content management systems-joomla, drupal and wordpress. *International Journal of Computer Applications* **2011,** *21* (4), 39-43.

242. Patel, S. K.; Rathod, V. R.; Parikh, S. In *Joomla, Drupal and WordPress-a statistical comparison of open source CMS*, 3rd International Conference on Trendz in Information Sciences & Computing (TISC2011), IEEE: 2011; pp 182-187.

243. Elliott, C.; Vijayakumar, V.; Zink, W.; Hansen, R., National instruments LabVIEW: a programming environment for laboratory automation and measurement. *JALA: Journal of the Association for Laboratory Automation* **2007,** *12* (1), 17-24.

244. Van Der Walt, S.; Colbert, S. C.; Varoquaux, G., The NumPy array: a structure for efficient numerical computation. *Computing in Science & Engineering* **2011,** *13* (2), 22.

245. Taban, I. M.; Altelaar, A. F.; van der Burgt, Y. E.; McDonnell, L. A.; Heeren, R. M.; Fuchser, J.; Baykut, G., Imaging of peptides in the rat brain using MALDI-FTICR mass spectrometry. *Journal of the American Society for Mass Spectrometry* **2007,** *18* (1), 145-51.

246. Hillenkamp, F.; Karas, M.; Beavis, R. C.; Chait, B. T., Matrix-assisted laser desorption/ionization mass spectrometry of biopolymers. *Analytical chemistry* **1991,** *63* (24), 1193A-1203A.

247. Kaufmann, R., Matrix-assisted laser desorption ionization (MALDI) mass spectrometry: a novel analytical tool in molecular biology and biotechnology. *Journal of biotechnology* **1995,** *41* (2), 155-175.

248. Touboul, D.; Halgand, F.; Brunelle, A.; Kersting, R.; Tallarek, E.; Hagenhoff, B.; Laprévote, O., Tissue molecular ion imaging by gold cluster ion bombardment. *Analytical chemistry* **2004,** *76* (6), 1550-1559.

249. Todd, P. J.; Schaaff, T. G.; Chaurand, P.; Caprioli, R. M., Organic ion imaging of biological tissue with secondary ion mass spectrometry and matrix-assisted laser desorption/ionization. *Journal of Mass Spectrometry* **2001,** *36* (4), 355-369.

250. Weston, D. J.; Bateman, R.; Wilson, I. D.; Wood, T. R.; Creaser, C. S., Direct analysis of pharmaceutical drug formulations using ion mobility spectrometry/quadrupole-time-of-flight mass spectrometry combined with desorption electrospray ionization. *Analytical chemistry* **2005,** *77* (23), 7572-7580.

251. Takats, Z.; Wiseman, J. M.; Cooks, R. G., Ambient mass spectrometry using desorption electrospray ionization (DESI): instrumentation, mechanisms and applications in forensics, chemistry, and biology. *Journal of Mass Spectrometry* **2005,** *40* (10), 1261-1275.

252. Wiseman, J. M.; Ifa, D. R.; Zhu, Y.; Kissinger, C. B.; Manicke, N. E.; Kissinger, P. T.; Cooks, R. G., Desorption electrospray ionization mass spectrometry: Imaging drugs and metabolites in tissues. *Proceedings of the National Academy of Sciences* **2008,** *105* (47), 18120-18125.

253. Spraggins, J. M.; Rizzo, D. G.; Moore, J. L.; Noto, M. J.; Skaar, E. P.; Caprioli, R. M., Next-generation technologies for spatial proteomics: Integrating ultra-high speed MALDI-TOF and high mass resolution MALDI FTICR imaging mass spectrometry for protein analysis. *PROTEOMICS* **2016**

254. Buck, A.; Balluff, B.; Voss, A.; Langer, R.; Zitzelsberger, H.; Aichler, M.; Walch, A., How Suitable is Matrix-Assisted Laser Desorption/Ionization-Time-of-Flight for Metabolite Imaging from Clinical Formalin-Fixed and Paraffin-Embedded Tissue Samples in Comparison to Matrix-Assisted Laser Desorption/Ionization-Fourier Transform Ion Cyclotron Resonance Mass Spectrometry? *Anal Chem* **2016**.

255. Buck, A.; Ly, A.; Balluff, B.; Sun, N.; Gorzolka, K.; Feuchtinger, A.; Janssen, K. P.; Kuppen, P. J.; van de Velde, C. J.; Weirich, G., High-resolution MALDI-FT-ICR MS imaging for the analysis of metabolites from formalin-fixed, paraffin-embedded clinical tissue samples. *The Journal of pathology* **2015,** *237* (1), 123-132.

256. Smith, D. F.; Kiss, A.; Leach, F. E., 3rd; Robinson, E. W.; Pasa-Tolic, L.; Heeren, R. M., High mass accuracy and high mass resolving power FT-ICR secondary ion mass spectrometry for biological tissue imaging. *Analytical and bioanalytical chemistry* **2013,** *405* (18), 6069-76.

257. Pól, J.; Vidová, V.; Kruppa, G.; Kobliha, V. c.; Novák, P.; Lemr, K.; Kotiaho, T.; Kostiainen, R.; Havlíček, V. r.; Volný, M., Automated ambient desorption− ionization platform for surface imaging integrated with a commercial Fourier transform ion cyclotron resonance mass spectrometer. *Analytical chemistry* **2009,** *81* (20), 8479-8487.

258. Cornett, D. S.; Frappier, S. L.; Caprioli, R. M., MALDI-FTICR imaging mass spectrometry of drugs and metabolites in tissue. *Analytical chemistry* **2008,** *80* (14), 5648-5653.

259. Stemmler, E. A.; Cashman, C. R.; Messinger, D. I.; Gardner, N. P.; Dickinson, P. S.; Christie, A. E., High-mass-resolution direct-tissue MALDI-FTMS reveals broad conservation of three neuropeptides (APSGFLGMRamide, GYRKPPFNGSIFamide and pQDLDHVFLRFamide) across members of seven decapod crustaean infraorders. *Peptides* **2007,** *28* (11), 2104-15.

260. Chandra, S.; Parker, D. J.; Barth, R. F.; Pannullo, S. C., Quantitative imaging of magnesium distribution at single-cell resolution in brain tumors and infiltrating tumor cells with secondary ion mass spectrometry (SIMS). *Journal of neuro-oncology* **2016,** *127* (1), 33-41.

261. Holzlechner, G.; Kubicek, M.; Hutter, H.; Fleig, J., A novel ToF-SIMS operation mode for improved accuracy and lateral resolution of oxygen isotope measurements on oxides. *Journal of Analytical Atomic Spectrometry* **2013,** *28* (7), 1080-1089.

262. Boggio, K. J.; Obasuyi, E.; Sugino, K.; Nelson, S. B.; Agar, N. Y.; Agar, J. N., Recent advances in single-cell MALDI mass spectrometry imaging and potential clinical impact. *Expert review of proteomics* **2011,** *8* (5), 591-604.

263. Smith, D. F.; Kharchenko, A.; Konijnenburg, M.; Klinkert, I.; Pasa-Tolic, L.; Heeren, R. M., Advanced mass calibration and visualization for FT-ICR mass spectrometry imaging. *Journal of the American Society for Mass Spectrometry* **2012,** *23* (11), 1865-72.

264. Brantley, M.; Zekavat, B.; Harper, B.; Mason, R.; Solouki, T., Automated deconvolution of overlapped ion mobility profiles. *Journal of the American Society for Mass Spectrometry* **2014,** *25* (10), 1810-1819.

265. Harper, B.; Miladi, M.; Solouki, T., Loss of internal backbone carbonyls: additional evidence for sequence-scrambling in collision-induced dissociation of y-type ions. *Journal of the American Society for Mass Spectrometry* **2014,** *25* (10), 1716-1729.

266. Pettit, M. E.; Harper, B.; Brantley, M. R.; Solouki, T., Collision-energy resolved ion mobility characterization of isomeric mixtures. *Analyst* **2015,** *140* (20), 6886-6896.

267. Zekavat, B.; Miladi, M.; Al-Fdeilat, A. H.; Somogyi, A.; Solouki, T., Evidence for sequence scrambling and divergent H/D exchange reactions of doubly-charged isobaric b-type fragment ions. *Journal of the American Society for Mass Spectrometry* **2014,** *25* (2), 226-236.

268. Zekavat, B.; Miladi, M.; Becker, C.; Munisamy, S. M.; Solouki, T., Combined use of post-ion mobility/collision-induced dissociation and chemometrics for b fragment ion analysis. *Journal of the American Society for Mass Spectrometry* **2013,** *24* (9), 1355-1365.

269. Zekavat, B.; Solouki, T., Chemometric data analysis for deconvolution of overlapped ion mobility profiles. *Journal of the American Society for Mass Spectrometry* **2012,** *23* (11), 1873-1884.

270. Lu, W.; Olaitan, A. D.; Brantley, M. R.; Zekavat, B.; Erdogan, D. A.; Ozensoy, E.; Solouki, T., Photocatalytic Conversion of Nitric Oxide on Titanium Dioxide: Cryotrapping of Reaction Products for Online Monitoring by Mass Spectrometry. *The Journal of Physical Chemistry C* **2016**.

271. Zawacka-Pankau, J.; Kostecka, A.; Sznarkowska, A.; Hedström, E.; Kawiak, A., p73 tumor suppressor protein: a close relative of p53 not only in structure but also in anti-cancer approach? *Cell Cycle* **2010,** *9* (4), 720-728.

272. Kovalev, S.; Marchenko, N.; Swendeman, S.; LaQuaglia, M.; Moll, U. M., Expression level, allelic origin, and mutation analysis of the p73 gene in neuroblastoma tumors and cell lines. *Cell Growth and Differentiation-Publication American Association for Cancer Research* **1998,** *9* (11), 897-904.

273. Ledford Jr, E. B.; Rempel, D. L.; Gross, M., Space charge effects in Fourier transform mass spectrometry. II. Mass calibration. *Analytical chemistry* **1984,** *56* (14), 2744-2748.

274. Pettit, M. E. Development of ion mobility mass spectrometry deconvolution strategies for use in data-independent acquisition proteomics. 2018.

275. Miladi, M. Structural characterization of peptides and peptide fragment ions using high resolution mass spectrometry and ion mobility spectrometry. 2014.

276. Harper, B. D. Structural analysis of biomolecules using ion mobility and mass spectrometry: exploration of ion rearrangements and conformations. 2016.

277. Eiceman, G. A.; Karpas, Z.; Hill Jr, H. H., *Ion mobility spectrometry*. CRC press: 2013.

278. May, J. C.; McLean, J. A., Ion mobility-mass spectrometry: time-dispersive instrumentation. *Analytical chemistry* **2015,** *87* (3), 1422-1436.

279. Hill Jr, H. H.; Siems, W. F.; Louis, R. H. S.; McMinn, D. G., Ion mobility spectrometry. *Analytical Chemistry* **1990,** *62* (23), 1201A-1209A.

280. Shvartsburg, A. A., *Differential ion mobility spectrometry: nonlinear ion transport and fundamentals of FAIMS*. CRC Press: 2008.

281. Fernandez-Lima, F.; Kaplan, D.; Park, M., Note: Integration of trapped ion mobility spectrometry with mass spectrometry. *Review of Scientific Instruments* **2011,** *82* (12), 126106.

282. Dwivedi, P.; Wu, P.; Klopsch, S. J.; Puzon, G. J.; Xun, L.; Hill, H. H., Metabolic profiling by ion mobility mass spectrometry (IMMS). *Metabolomics* **2008,** *4* (1), 63-80.

283. Ruotolo, B. T.; Gillig, K. J.; Stone, E. G.; Russell, D. H., Peak capacity of ion mobility mass spectrometry:: Separation of peptides in helium buffer gas. *Journal of Chromatography B* **2002,** *782* (1-2), 385-392.

284. Horvath, C. G.; Lipsky, S. R., Peak capacity in chromatography. *Analytical chemistry* **1967,** *39* (14), 1893-1893.

285. Giles, K.; Williams, J. P.; Campuzano, I., Enhancements in travelling wave ion mobility resolution. *Rapid Communications in Mass Spectrometry* **2011,** *25* (11), 1559-1566.

286. Harper, B.; Neumann, E. K.; Stow, S. M.; May, J. C.; McLean, J. A.; Solouki, T., Determination of ion mobility collision cross sections for unresolved isomeric mixtures using tandem mass spectrometry and chemometric deconvolution. *Analytica chimica acta* **2016,** *939*, 64-72.

287. Brantley, M. R.; Pettit, M. E.; Harper, B.; Brown, B.; Solouki, T., Automated peak width measurements for targeted analysis of ion mobility unresolved species. *Analytica chimica acta* **2016,** *941*, 49-60.

288. Pettit, M. E.; Brantley, M. R.; Donnarumma, F.; Murray, K. K.; Solouki, T., Broadband ion mobility deconvolution for rapid analysis of complex mixtures. *Analyst* **2018,** *143* (11), 2574-2586.